



## X-ray Phase Contrast Nano-Tomography of Third Generation Solar Cells

**Fevola, Giovanni**

*Publication date:*  
2020

*Document Version*  
Publisher's PDF, also known as Version of record

[Link back to DTU Orbit](#)

*Citation (APA):*  
Fevola, G. (2020). *X-ray Phase Contrast Nano-Tomography of Third Generation Solar Cells*. Technical University of Denmark.

---

### General rights

Copyright and moral rights for the publications made accessible in the public portal are retained by the authors and/or other copyright owners and it is a condition of accessing publications that users recognise and abide by the legal requirements associated with these rights.

- Users may download and print one copy of any publication from the public portal for the purpose of private study or research.
- You may not further distribute the material or use it for any profit-making activity or commercial gain
- You may freely distribute the URL identifying the publication in the public portal

If you believe that this document breaches copyright please contact us providing details, and we will remove access to the work immediately and investigate your claim.

# **X-ray Phase Contrast Nano-Tomography of Third Generation Solar Cells**

PhD Thesis

Technical University of Denmark

Department of Energy Conversion and Storage

**Author:**

Giovanni Fevola

**Supervisors:**

Jens W. Andreasen

Dina Carbone

Yiqiu Dong

June, 2020

**X-ray Phase Contrast Nano-Tomography of Third Generation Solar Cells**

Report  
2020

By  
Giovanni Fevola

Copyright:   Reproduction of this publication in whole or in part must include the customary bibliographic citation, including author attribution, report title, etc.

Cover photo: [/]

Published    DTU, Department of Energy Conversion and Storage, Fysikvej  
Building 310, DK-2800 Kgs. Lyngby, Denmark

by:            [www.dtu.dk](http://www.dtu.dk)

ISSN:         [0000-0000] (electronic version)

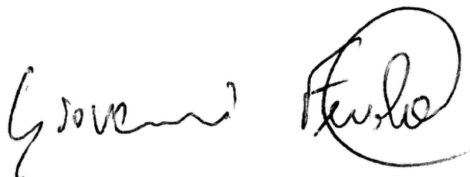
# Preface

This thesis is submitted in candidacy for the Ph.D. degree from the Technical University of Denmark (DTU). The work was carried out at the Department of Energy Conversion and Storage in the period from September 2016 to September 2019. The project was supervised by Professor Jens Wenzel Andreasen, and co-supervised by Beamline Scientist Dina Carbone and Associate Professor Yiqiu Dong. A period of 6 weeks was spent on external stay at the German Electron Synchrotron (DESY), under Dr. Falkenberg's supervision.

This work was funded by the European Research Council (ERC) under the European Union's Horizon 2020 research and innovation programme (SEEWHI Consolidator grant, ERC-2015-CoG-681881) and by the Ministry of Higher Education and Science (DANSCATT grant, 7055-00007B).

Hamburg, June 2020

Giovanni Fevola

A handwritten signature in black ink, appearing to read 'Giovanni Fevola'. The signature is written in a cursive style with a large, circular flourish at the end.



# Table Of Contents

<b>1. INTRODUCTION .....</b>	<b>10</b>
1.1 THESIS STRUCTURE.....	11
<b>2. X-RAY IMAGING .....</b>	<b>13</b>
2.1.1 Synchrotron Radiation .....	13
2.1.2 Interaction with matter .....	15
2.1.3 Propagation.....	17
2.2 SYNCHROTRON TECHNIQUES .....	18
2.2.1 Scanning Transmission X-ray Microscopy and Coherent Diffractive Imaging .....	18
2.2.2 Ptychography.....	20
2.2.3 Resonant X-ray Imaging .....	25
2.2.4 Tomography.....	27
2.2.5 X-ray Beam Induced Current/Voltage (XBIC/XBIV).....	28
2.2.6 Laminography .....	29
2.2.7 Note on optics.....	31
2.3 RECONSTRUCTION QUALITY IN X-RAY IMAGING .....	33
2.3.1 Resolution Assessment .....	33
2.3.2 Quantitativeness of Ptychographic Nanotomography .....	34
<b>3. ULTRAMICROSCOOPY OF SOLAR CELLS.....</b>	<b>36</b>
3.1 ORGANIC SOLAR CELLS .....	37
3.1.1 Studies on organic blends .....	41
3.1.2 Our experiment proposal .....	45
3.2 KESTERITE SOLAR CELLS.....	48
3.2.1 X-ray fluorescence of CZTS .....	51
3.2.2 Ptychographic Tomography of Kesterite from Oxides.....	53
<b>4. MONTE CARLO RAY TRACING SIMULATIONS OF COHERENT DIFFRACTIVE IMAGING .....</b>	<b>57</b>
4.1 JOURNAL ARTICLE 1 .....	58
4.2 SUPPORTING INFORMATION .....	71
4.2.1 Effect of subvoxel size .....	71
4.2.2 Resolution assessment.....	71
<b>5. RESONANT X-RAY PTYCHOGRAPHIC NANO-TOMOGRAPHY OF KESTERITE SOLAR CELLS .....</b>	<b>75</b>

5.1	JOURNAL ARTICLE 2 .....	76
5.2	SUPPLEMENTAL MATERIAL .....	89
5.2.1	Additional figures and Tables .....	89
5.2.2	Note on radiation damage .....	95
<b>6.</b>	<b>CONCLUSIONS AND OUTLOOK .....</b>	<b>98</b>
6.1	OUTLOOK.....	100
<b>7.</b>	<b>REFERENCES .....</b>	<b>103</b>

## Summary

Solar cells are likely to play an increasing role in the future energy scenario and a new generation of solar cells is being developed for this purpose, with a strong focus on sustainability. The solar cells we focus on have organic or kesterite absorber layers. The organic solar cells suffer from degradation and instability, for which their nanomorphology plays a key role whereas the efficiency of kesterite cells is still hampered by presence of secondary phases, which is below detection limits for standard techniques. Unlike silicon, both technologies are thin-film, with absorber layers that can be as thin as a few microns.

Such size makes them suitable for a nanoscale study with synchrotron X-ray imaging techniques, which is the goal of this project. The techniques we dealt with are three-dimensional, non-destructive, quantitative, allow for sample sizes of tens of microns, and achieve resolutions in the 10-20 nm range.

Importantly, these techniques are based on coherent diffractive imaging methods, which we have demonstrated in an alternative simulation framework solely based on ray tracing. This approach operates in real space and enables in principle to explore configurations for which an analytical solution is not available.

This framework was developed to simulate an experiment with organic solar cells. The criticality of this sample with respect to resolution, contrast, and radiation damage, is outlined in this work.

Experimentally, we demonstrated resonant ptychographic tomography of kesterite solar cells. The measurements achieve an unprecedented combination of high resolution, quantitiveness, and elemental sensitivity to three different elements. These remarkable imaging capabilities enable quantification and localization of defective features that were overlooked by standard characterization techniques.

## Dansk Resumé

Solceller vil med stor sandsynlighed spille en vigtig rolle i fremtidens energiscenarier, og en ny generation af solceller er ved at blive udviklet til disse med et stort fokus på bæredygtighed. De typer solceller, som vi her vil fokusere på, er kaldet organiske solceller og kesteritsolceller. Organiske solceller er ofte ustabile og bliver nedbrudt, når de udsættes for varme og UV-stråling, hvilket er stærkt relateret til ændringer i deres nanomorfologi, mens kesteritsolcellers effektivitet til stadighed er hæmmet af sekundære faser, som er under detektionsgrænserne for standardteknikker. Ulig siliciumsolceller er begge disse typer af solceller tyndfilmsteknologier og består dermed af aktive lag, der kan være så tynde som få mikrometer. Disse størrelser gør dem egnede til studier af deres nanomorfologi ved brug af billeddannelsesteknikker baseret på synkrotronrøntgenstråling, hvilket er målet med dette projekt.

Teknikkerne, som vi beskæftiger os med, er tredimensionelle, ikke-ødelæggende og kvantitative, de tillader undersøgelse af prøver med størrelser på op til 100  $\mu\text{m}$ , og de opnår opløsninger på 10-20 nm. Mest bemærkelsesværdigt er, at disse teknikker er baseret på koherente, diffraktive billeddannelsesteknikker, hvilket vi har demonstreret i en alternativ simuleringsramme, der udelukkende er baseret på strålesporing. Denne tilgang opererer i det reelle rum og gør det i princippet muligt at udforske konfigurationer, for hvilke analytiske løsninger ikke er tilgængelige.

Denne simuleringsramme blev udviklet til at simulere et eksperiment med organiske solceller. Vigtigheden af at opnå høj opløsning og kontrast samt at minimere stråleskade for organiske prøver som denne er skitseret i denne afhandling.

Eksperimentelt har vi demonstreret resonant, ptychografisk tomografi af kesteritsolceller. Målingerne opnåede en kombination af høj opløsning, kvantitativ præcision og følsomhed for tre forskellige grundstoffer, hvilket er uden fortilfælde. Disse bemærkelsesværdige muligheder indenfor billeddannelse gør det muligt at kvantificere og lokalisere defekter, der blev overset med standardkarakteriseringsteknikker.

## List of Acronyms

(2,3,4)D	(Two-, Three-, Four-) Dimensional
AFM	Atomic Force Microscopy
BW	Bandwidth
CBD	Chemical Bath Deposition
CDI	Coherent Diffractive Imaging
CIGS	Cu-In-Ga-Se
CZT(S,Se)	Copper Zinc Tin (Sulfide, Selenide) - $\text{Cu}_2\text{ZnSn}(\text{S,Se})_4$
EDS	Energy Dispersive X-ray Spectroscopy
EFTEM	Energy Filtered Transmission Electron Microscopy
FFT	Fast Fourier Transform
FIB	Focused Ion Beam
F(R,S)C	Fourier (Ring, Shell) Correlation
FWHM	Full Width Half Maximum
ITO	Indium Tin Oxide
MLL	Multilayer Laue Lenses
OSC	Organic Solar Cells
PLD	Pulsed Laser Deposition
PXCT	Ptychographic X-ray Computer Tomography
RXPT	Resonant X-ray Ptychographic Tomography
SAXS	Small Angle X-ray Scattering
SEM	Scanning Electron Microscope
SLG	Soda Lime Glass
SNR	Signal to Noise Ratio
STEM	Scanning Transmission Electron Microscopy
STXM	Scanning Transmission X-ray Microscopy
TEM	Transmission Electron Microscopy
XBI(C,V)	X-ray Beam Induced (Current, Voltage)
XRD	X-ray diffraction

## **Acknowledgements**

I thank Jens W. Andreasen and Luise T. Kuhn for giving me the opportunity to pursue a PhD at DTU Energy. Prof. Andreasen is also thanked for his stern guidance.

Dina Carbone, for hosting me on beamtimes at NanoMax and for her support on the ray tracing work. Yiqiu Dong, for her lessons on inverse problems.

Erik B. Knudsen for endless support and for his attitude on the McWork. Peter S. Jorgensen for guidance and support on the analysis of tomographic data.

Tiago, for introducing me to the field of phasing algorithms and to the analysis of experimental data, for starting operando investigations, fostering the collaboration with Dr. Stuckelberger, through a series of lucky coincidences.

Besides Peter, Tiago and Jens, the other members of our phycho-club, more or less occasional: Azat, Mariana, Michael, hoping they will remember the first rule. Raha, for sharing the office and a lot of PhD experience.

Ebtisam and Karl for first- and last-minute help on sample preparation. Anders, for his help with choice of polymer and small molecule to be used for EFTEM study; Søren Bredmose for carrying out EFTEM and electron tomography with Sofie Colding-Jørgensen; Marcial for preparing samples for the EFTEM; Christian, Moises, Shagai for fruitful discussion of CZTS data and information about fabrication processes of CZTS and CIGS cells. Megha for her proofreading; Salvatore, for helpful discussions on sample preparation, data presentation, and for inviting me to a beamtime which was an invaluablely precious experience; Simone for his informal mentoring.

# 1. Introduction

With the increasing energy demand, renewable sources and solar in particular are likely to play an increasingly decisive role in the future energy production [1]. In fact, a new generation of solar cells is being developed to address a growing energy demand, with a strong focus on sustainability. Low-energy-input, environment-friendly technologies alternative or complementary to silicon are under investigation as absorber materials that would be competitive in terms of efficiency, energy payback time, and scalability. The topic of this project is the investigation of such devices with ultra-high resolution X-ray imaging techniques. In simple terms, the idea behind this project is to use the most powerful<sup>1</sup> 3D X-ray microscopes available today to characterize and study solar cells. Characterization on the nanoscale can provide insight on things like grain morphology, grain boundaries, interfaces, and secondary phases. That can be done in a non-destructive way, on significant volumes, allowing for in situ and operando studies. Many very good PhD theses have been written about these microscopes and even the youngest techniques have started to appear on books, therefore many works will be cited throughout this text and only the essentials summarized. The microscopes we refer to are not laboratory tools but are complex instruments that take several months to build in large facilities and are continuously upgraded, prompted by research cases built within an astoundingly wide range of disciplines. Access to these microscopes is not easily granted. A sound scientific case needs to be described in a beamtime proposal, i.e. an application requesting access to this microscope. The proposal is evaluated by a panel of experts which rates the proposal based on their expected scientific impact, their feasibility, and chance of success. Only proposals with the highest scores are granted beamtime. Therefore, using this microscope is not something that can be done routinely (so far), but is more of a one-shot experiment. Because of that, it can hardly be

---

<sup>1</sup> The figures of merit for this statement will be clarified.

integrated in the fabrication process and provide useful feedback for trial and error tuning of the process.

The devices we choose to focus on are the kesterite and organic devices, which are both non-toxic and earth-abundant, which are appealing features in terms of sustainability. The other common characteristic is that they are thin-film devices. By employing a direct semiconductor, they require less material to absorb most of the solar spectrum. That is advantageous in perspective, thinking of large scale production, and interesting from an X-ray imaging point of view, as it makes it possible to study them with the ultra-high resolution techniques we will discuss. A classical silicon device has been studied with laboratory computer tomography scan, but that line of enquiry has not seen any continuation so far [2].

The two main contributions of this project consist of an addition to the simulation techniques and to the application, with relatively novel variations, of such techniques to kesterite solar cells. The possibility to exploit this ultra-high resolution microscopy techniques requires the synchrotron to build a solid, convincing scientific case to make an experiment and it was not granted in our case for the organic solar cells, but it was for the kesterite solar cells.

## **1.1 Thesis Structure**

The aim of this text is to illustrate how this project was carried out and the rationale behind our efforts, for evaluation of a committee of experts. Hopefully, it can come in handy for a PhD student being introduced to the field. The work is organized in such a way that theories and concepts useful or necessary to understand our novel contributions are illustrated in chapter 2 and 3. These chapters illustrate respectively the context for X-ray synchrotron imaging and for the investigated solar cells. Not all the techniques mentioned in chapter 2 have been used during the project, but if they haven't they are complementary to the ones used. We did not use CDI or STXM for any experiment, but we feel it necessary to introduce them to talk about ptychography. Likewise, laminography was not used during the project, but it is mentioned in outlook of our tomography work, and we considered to devote a separate paragraph to it.



In chapter 3, the reader will find, in addition to references to existing literature, some results of ours which are not in publishable form, but are worth reporting in the text. Our novel contributions in the form of published articles are presented in chapters 4 and 5. Conclusions and perspective about this project are drawn in chapter 6.

## 2. X-ray Imaging

In this chapter we describe the microscope, mentioning some of its basic working principles, illustrating some most recent developments, and pointing to certain lines of inquiry. This sort of survey should by no means be intended as exhaustive, but includes our view of ideas and context that were potentially relevant for our two main endeavors with respect to simulations and experiments, presented in the later chapters.

X-ray science can probe matter on the whole spectrum from scales of interatomic crystal planes with spacing on the Å scale to time resolved laboratory computed tomography.

The parameters of interest of these techniques include spatial resolution, maximum sample size, acquisition time, dose efficiency, just to mention a few. Often there exists a trade-off between them. The techniques we discuss here cover roughly the range of single/double-digit nm resolution.

### 2.1.1 Synchrotron Radiation

Synchrotrons are the large facilities where X-ray beams with unique properties are produced. The main component of a synchrotron is the storage ring, which is a long pipe where electrons circulate in vacuum at speeds close to that of light. The circular trajectory is imposed by a system of bending magnets and there are radio-frequency cavities that accelerate electrons that have lost energy.

The X-ray beams are derived from the ring at many tangent points, called beamlines. The layout of the beamline NanoMax at MAX IV is illustrated in **Figure 2-1**.

The essential components of a beamline are:

- An undulator or a wiggler, i.e. a periodic array of magnets that wiggle electrons. The acceleration they induce produces an intense X-ray beam, with very low angular divergence. In the undulators, where the electrons are wiggled more gently than in wigglers, the angular divergence is smaller by a factor  $\sqrt{N}$  and the bandwidth is narrower. The emitted frequency is determined by the array period and can be changed by changing the distance between the poles in the magnet array.

- A monochromator, which is typically a double Si (111) crystal that exploits Bragg's law to select the photons that have a certain wavelength.
- Pre-focusing optics, such as mirrors and slits/apertures that help to steer the beam towards the target;
- An experimental hutch, where the beam is focused onto the sample, lodged on a sample stage, and is measured by detectors.

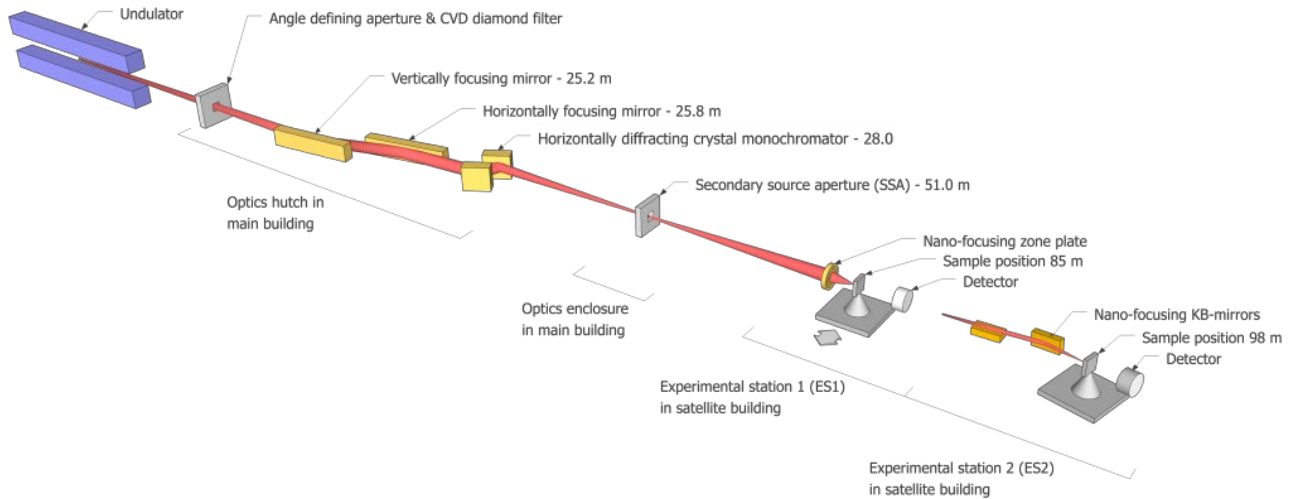


**Figure 2-1. Layout of the NanoMax beamline at MAX IV. From Nanomax website.**

## Properties of Synchrotrons X-rays Beams

The main way sources are characterized, is by their brilliance, defined as:

$$\text{Brilliance} = \frac{\text{Photons/second}}{\text{source}[\text{mm}^2] \text{divergence}[\text{rad}^2] 0.1\% \text{BW}}, \quad 2.1$$

stating that a brilliant source is not only intense (many photons per second) but is also well-confined and collimated and that most of its photons are in a narrow bandwidth range.

A high flux is obviously useful to reduce acquisition time, but is also beneficial for resolution. In fact, even the most stable setup typically suffers oscillations in the 1-10 nm order of magnitude. A quick acquisition of the illumination prevents the blur that this oscillation would cause.

The imaging techniques that we discuss also largely rely on coherence. Coherence is the property that allows waves to produce observable interference and diffraction phenomena [3] and is a measurement of the degree of correlation between two points of a wavefield in time and space. Coherence is lost when diffraction fringes are poorly visible or when there is poor correlation between two points of a wavefield in space or time. Coherence can be lost because of the beam not being perfectly monochromatic or collimated. In the two cases we refer to the temporal/longitudinal and the spatial/transverse coherence. As only the idealization of a point-like source or a plane wave are actually coherent, the coherence lengths are used to define the distances on which the beam can be still considered on a good approximation coherent. They can be defined as the distances it takes to catch up in phase, both in the longitudinal and the transverse case. The expressions are taken from [4]. For the longitudinal coherence, in case of a  $\Delta\lambda$  offset, the longitudinal coherence length amounts to:

$$L_L = \frac{1}{2} \frac{\lambda^2}{\Delta\lambda}. \quad 2.2$$

In the case of two waves with same wavelength but originating from opposite ends of an object with size  $D$ , if the observation point is at a distance  $R$ , then the transverse coherence length can be estimated as:

$$L_T = \frac{\lambda R}{2D}. \quad 2.3$$

### 2.1.2 Interaction with matter

Interaction with matter of X-rays with wavelength  $\lambda$  can be modeled by the complex refractive index

$$n(\lambda) = 1 - \delta(\lambda) + j\beta(\lambda), \quad 2.4$$

$\delta$  is responsible for the phase shift of the radiation through the object:

$$\Phi = 2\pi \int_0^L \delta(\lambda) dz \quad 2.5$$

$\beta$  is responsible for the absorption, also modeled by the absorption coefficient  $\mu = 4\pi/\lambda$ , which is used in the Lambert-Beer law, relating the incoming and outgoing intensity through an object:

$$I_{\text{out}} = I_{\text{in}} \exp(-\mu L) \quad 2.6$$

The dependence on the wavelength stems from the complex atomic scattering factor  $f(\lambda) = Z + f_1(\lambda) + jf_2(\lambda)$ , with its real and imaginary part related to  $\delta$  and  $\beta$  as follows:

$$\delta(\lambda) = \frac{r_0}{2\pi} \lambda^2 n_{\text{at}} [Z + f_1(\lambda)] \quad 2.7$$

$$\beta(\lambda) = \frac{r_0}{2\pi} \lambda^2 n_{\text{at}} f_2(\lambda),$$

With  $r_0$  being the classical electron radius and  $Z$  being the atomic number.

Kramer-Kronig relations allow calculation of the real part of the atomic scattering factor from its imaginary part or from absorption data. A useful example of the dependence on energy of  $f_1$  in different compounds is represented in **Figure 2-2**.

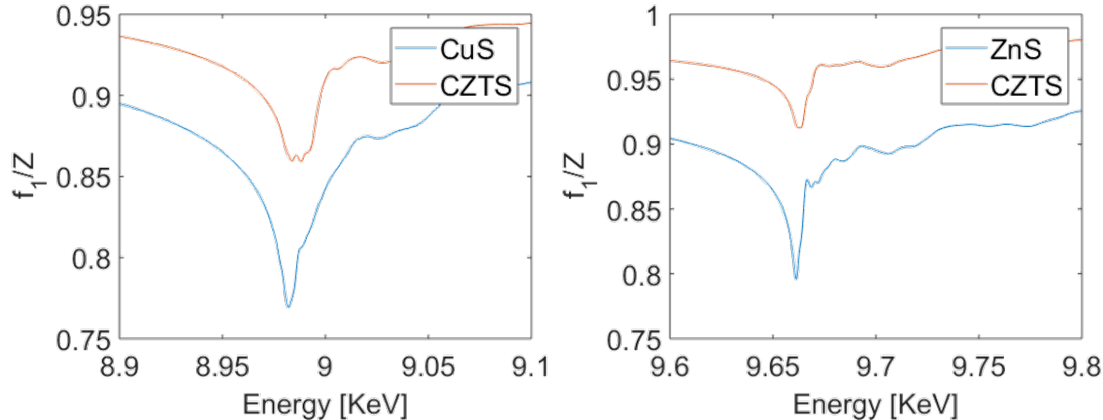


**Figure 2-2. Empirical relative variation of the real part of scattering factor. The scattering factor is plotted as a fraction of CuS and CZTS around Cu K-edge (left); ZnS and CZTS around Zn K-edge (right). This fine-structure variation is computed from experimental data provided by Rein et al. (article in preparation), using the software KKcalc [5].**

## Fluorescence

When enough energy is absorbed to promote electrons in the illuminated material into an upper shell, they eventually decay and emit a radiation with energy equal to the

difference in energy levels. This radiation is typically in the X-ray regime and is called fluorescence.

### 2.1.3 Propagation

In this section we sum up the most widely used formulas for propagation. For a full derivation refer to [6], from which they are taken, with an adapted notation.

Given a source of electromagnetic radiation three regions are defined for its propagation: the contact, the near-field (Fresnel), and the far-field (Fraunhofer) regions. They are precisely identified by these three conditions that relate the Fresnel number  $F_N$ , defined as follows:

$$F_N = \frac{a^2}{z\lambda}, \quad 2.8$$

where  $a$  is the largest size of the object or the radiator,  $z$  is the distance between the radiator and the detector,  $\lambda$  is the source wavelength.

Let the propagation axis be  $z$  and let  $(x, y)$  and  $(X, Y)$  be two planar coordinate systems at  $z = 0$  and  $z = z$ . The momentum transfer is defined as

$$\mathbf{q} = \frac{\mathbf{s}}{\lambda z}, \quad 2.9$$

with  $\mathbf{s} = (X, Y)$  being an observation point in a plane orthogonal to the optical axis at distance  $z$ . In that case,  $2\pi\mathbf{q}$  can be seen as the transverse component of the propagation vector  $\mathbf{k}$  a wave scattered from the origin towards  $(X, Y, z)$  in space.

The angular spectrum solution is an exact solution of the Helmholtz equation<sup>2</sup>:

$$\Psi(x, y) = \mathfrak{F}^{-1} \left[ \mathfrak{F}(\psi(x, y, z = 0)) \exp\left(\frac{2\pi j z}{\lambda} \sqrt{1 - \mathbf{q}^2 \lambda^2}\right) \right], \quad 2.10$$

$\psi$  being the wavefield in the plane  $z = 0$ , and  $\Psi$  being the one propagated at distance  $z$ . Under the small angle approximation, in the near-field region ( $F_N \gg 1$ ), it can be approximated to:

---

<sup>2</sup> Its only assumption is:  $z \gg \lambda$ .

$$\Psi(x, y) = \exp(jkz) \mathfrak{F}^{-1}[\mathfrak{F}(\psi(x, y, z = 0)) \exp(-j\pi z \lambda \mathbf{q}^2)]. \quad 2.11$$

in the far-field region ( $F_N \ll 1$ ) the wavefield can be propagated as

$$\Psi(X, Y) = -\frac{jk \exp(jkz)}{z} \exp\left(jk \frac{X^2 + Y^2}{2z}\right) \mathfrak{F}[\psi(x, y)]. \quad 2.12$$

Giewekemeyer provides a useful and detailed MATLAB implementation of these formulas [7]. It can be shown that the same formulas can be derived from the more general Fresnel-Kirchhoff diffraction formula, which in the case of a source  $\psi_0$  on a surface  $S_0$  in the  $z = 0$  plane, can be written as:

$$\Psi(X, Y, z) = \frac{k}{2j\pi} \int_{S_0} \psi_0(x, y) \frac{\exp(jkr)}{r} \cos \alpha \, dx dy \quad 2.13$$

$r$  being the position vector pointing at  $(X, Y)$ , and  $\alpha$  the angle between  $r$  and the propagation axis. Such formula recalls the Huygens-Fresnel principle, by summing the spherical waves  $\frac{\exp(jkr)}{r}$  coming from  $S_0$ , weighted by their complex illumination function  $\psi_0$ .

## 2.2 Synchrotron Techniques

### 2.2.1 Scanning Transmission X-ray Microscopy and Coherent Diffractive Imaging

In scanning transmission X-ray microscopy (STXM) [8] the sample is raster-scanned with a focused beam and the number of transmitted photons is measured by a non-pixelated detector such as a photodiode. A map is obtained in which counts from each position are ascribed to each pixel. Fluorescence maps are collected in the same scheme, with the difference that, rather than photon counts, whole spectra are collected at each pixel position. The two setups are compatible as fluorescence is collected on the side, whereas the photon-counting detector is in line with the transmitted beam. The pixel size of these maps is obviously limited by the spot size on the sample and that size is limited by the optics. The smallest spot sizes obtained for this setup are around 10 nm [8], however the image quality suffers from the imperfections of the X-ray optics.

Coherent diffractive imaging (CDI) techniques were developed to overcome the limits of X-ray optics. They rely on a coherent beam and use no lens between sample and detector. In the full-field version<sup>3</sup>, the beam fully illuminates an object and diffraction patterns are collected in the far field. To recover the sample transmission function, a phase retrieval algorithm is necessary. This algorithm applies constraints in real and reciprocal space to return the transmission function and the probe.

A simulated example, references, and more information is given in our ray tracing simulation work [9]. For now we conclude by noting that measuring the diffraction pattern, or indirectly the object transmission function, entails sampling a physical (continuous) signal into discrete ones. The sampling step of the object is the reconstructed pixel size  $\Delta x$  and is determined by the highest spatial frequency considered on the diffraction pattern, i.e. the detector size if the measurements are not cropped. The reconstructed pixel size is determined by:

$$\Delta x = \frac{\lambda z}{N_p \Delta X} \quad \mathbf{2.14}$$

where  $\Delta X$  is the detector's pixel size, and  $N_p$  the number of pixels along the  $x$  direction. In the diffraction plane, in order to avoid aliasing, the intensity signal must be sampled according to the Shannon sampling theorem, i.e. at least at its Nyquist frequency. In a CDI setup, the bandwidth of the diffraction pattern is in fact the object lateral size  $W$ , and this requirement reads:

$$\Delta X < \frac{\lambda z}{2W} \quad \mathbf{2.15}$$

A signal sampled according to the Shannon theorem, is said to be oversampled.

---

<sup>3</sup> Normally simply referred to as CDI



### 2.2.2 Ptychography

The invention of ptychography is credited to Hoppe, who coined the name and described the principle in 1970 [10], however the first ptychographical phase retrieval was only published by Faulkner and Rodenburg in 2004 [11], [12] and the first experimental demonstration with X-rays came in [13]. Today, ptychography is well-established enough to be included in the most recent X-ray microscopy textbooks [14], [15].

It has been applied also to electron microscopy producing the highest resolution ever achieved for microscopy in general [16], [17], and to visible light [18]. The technique is the child of CDI and STXM, as it merges the phase retrieval approach of CDI with the STXM scan setup. By doing so, it inherits their best features, i.e. it extends the field of view of CDI and achieves higher resolution and sensitivity than STXM.

Ptychography allows to fully characterize the beam [19] without any prior knowledge of the test sample to use and with high precision, which has fostered its application for characterization of optics [20], [21].

Ptychography has also been demonstrated in near-field in two [22] and three [23] dimensions. There are no fundamental differences w.r.t. the far-field setup aside from the use of a cone-beam geometry for the beam and a different propagation model (equation 2.10). The advantage in this case consists of the possibility to image extremely optically-thick objects, as demonstrated with a 46  $\mu\text{m}$ -diameter uranium sphere [24].

Another approach aiming to allow thicker samples is provided by Tsai et al. [25], who takes up from the earlier demonstration of the multislice approach of Maiden et al. [26], which has recently been demonstrated in tomography [27].

In this approach the exit wave  $\psi$  is retrieved as usual, but the object is regarded as a series of slices  $O_1, \dots, O_N$  along the optical axis, and the relation between the incoming wavefield (the probe  $P = \psi_0$ ) and the exit wave accounts for the free propagation between each couple of adjacent slices:

$$\psi_i = P_F(\psi_{i-1} O_i) \quad i = 1, \dots, N \quad \mathbf{2.16}$$

in which  $P_F$  is a free-space (Fresnel) propagator and  $\psi_{i-1}$  is the incoming wave (the probe) for the slice  $O_i$ .

This approach overcomes the thin-sample approximation (supplemental material of [13]), which has been refined by numerical simulations [25] as

$$T \leq \frac{5.2 d^2}{\lambda} \quad 2.17$$

in which  $d$  is the resolution,  $T$  the maximum allowable thickness of the object, and  $\lambda$  is the incident wavelength. In tomography, the multislice approach for projections relaxes the Crowther criterion [27] [28].

Some of the popular algorithms for ptychography include: ePIE [29], difference map [30], RAAR [31], pHebie [32]. They aim to minimize the distance between the diffraction patterns of guesses of a common probe and the object and measurements. The problem can be seen as two separate tasks of finding: 1) the exit waves that minimize such distance for every scan position; 2) a common probe that yields these exit waves when scanned across the object.

ePIE has perhaps the most intuitive structure and we report it here as an example.

Starting from initial guesses for the object and probe, it recalculates the exit wave at each iteration, by imposing the modulus constraint, which amounts to substituting the square root of the measured intensities with the amplitudes of the current guess of the measured wavefield for each of the  $s$ -th displacement :

$$\begin{aligned} \Psi_i(\mathbf{u}) &= \sqrt{I_{i(s)}} \frac{\mathfrak{F}[\psi_i(\mathbf{r})]}{|\mathfrak{F}[\psi_i(\mathbf{r})]|} \\ \psi'_i(\mathbf{r}) &= \mathfrak{F}^{-1}[\Psi_i(\mathbf{u})] \end{aligned} \quad 2.18$$

Then, uses the new guess of the exit-wave to update functions for the probe and the object at the  $i$ -th iteration:

$$\begin{aligned} O_{i+1}(\mathbf{r}) &= O_i(\mathbf{r}) + \alpha \frac{P_i^*(\mathbf{r} - R_i)}{|P_i(\mathbf{r} - R_i)|_{\max}^2} (\psi'_i(\mathbf{r}) - \psi_i(\mathbf{r})) \\ P_{i+1}(\mathbf{r}) &= P_i(\mathbf{r}) + \beta \frac{O_i^*(\mathbf{r} - R_i)}{|O_i(\mathbf{r} - R_i)|_{\max}^2} (\psi'_i(\mathbf{r}) - \psi_i(\mathbf{r})) \end{aligned} \quad 2.19$$

$\alpha$  and  $\beta$  being tunable convergence speed parameters. These update functions implicitly enforce the overlap constraint.

Although these methods require a coherent beam, there is indeed an interest in relaxing this requirement. A wider portion of the beam entails higher flux, which in turn allows for shorter exposure time, relaxing the requirements on stability. The first milestone in that sense was to decompose the wavefield into a weighted sum of independent modes [33]. The article demonstrates that ptychography works by retrieving the weights of these modes besides probe and object, avoiding reconstruction artefacts due to partial coherence.

The intensities are modelled according to a sum of  $n$  independent modes according to:

$$I_j(q) = \sum_n \left| \int P_n(\mathbf{r}) O(\mathbf{r} + \mathbf{r}_j) \exp(-j\mathbf{q}\mathbf{r}) d\mathbf{r} \right|^2, \quad 2.20$$

where  $P_n$  are the independent probes,  $\mathbf{r}$  the position vector in the sample plane,  $\mathbf{r}_j$  the scanning positions, and  $\mathbf{q}$  the transverse component of the scattering vector. As the strict coherence requirements for ptychography could be relaxed, specifically, Enders et al. addressed temporal coherence [34]. They point out that such an expression cannot be extended to a pink beam because the propagation is wavelength-dependent; however, the effect of a broad bandwidth is limited to a blurring of the diffraction patterns, which does not affect the pattern as long as the probe size is small enough (the spectral blurring has to be smaller than the speckle size). They show that under such conditions the modal decomposition is still effective even without accounting for the different wavelengths in the propagation. Therefore, loss of temporal coherence only limits the portion of the diffraction patterns that can be used, whereas loss of spatial coherence can invalidate the whole dataset. In [35] Burdet et al. addressed spatial coherence by introducing a correction to the model of illumination. They highlight that the intensities that are recorded with a partially coherent beam can be expressed as a convolution of the ‘fully coherent’ intensities with a 2D Gaussian which is the Fourier transform of the mutual coherence function. The systematic effect of this Gaussian is to blur the diffraction patterns and it can be incorporated in the model of CDI phase retrieval, leading to better reconstructions and faster convergence.

Other parameters affect the outcome of the reconstruction, like the amount of overlap between adjacent illumination positions, and Bunk et al. has been determined 60% as a minimum value for successful reconstructions [36]. Although generally fulfilled, the constraints of CDI about oversampling do not strictly apply to ptychography. It has been shown that as long as there is sufficient overlap between illuminations, a phase retrieval is possible even with grossly undersampled patterns [37], [38].

Some scanning patterns are more effective than others at preventing artefacts, covering the area uniformly, which is particularly critical for low amount of overlap and noisy diffraction patterns [39].

Moreover, it has been demonstrated that the illumination can be optimized to reduce artifacts and lead to increased resolution of phase retrieval [40], [41].

Batey et al. demonstrated the interesting concept of ptychographical information multiplexing [42]. Using red, green, and blue laser beams to illuminate simultaneously a sample composed of three superimposed projector slides images of the same colors. They show that a modified version of the ePIE, in which the update functions account for simultaneous illumination by three incoherent modes, is able to retrieve the three single images, along with the probe function and the spectral weights of each wavelength. This, despite the superimposed slides not being fully transparent at other colors, and the diffraction patterns having different relative pixel size.

A more recent proof of principle validates an interesting concept for in situ studies. Whereas ptychography exploits a spatial overlap of the illuminations, in situ coherent diffractive imaging [43] can successfully exploit a *temporal* overlap of diffraction patterns. In this setup a set of diffraction patterns is recorded at different time steps and the phase retrieval is performed on this dataset assuming that there is a partial overlap, i.e. the sample is seen as a composition of a static and a dynamic portion. Importantly, the authors also compare CDI to ptychography, showing that for the same resolution and dose CDI allows for a higher temporal resolution.

A strategy for reducing scan time comes from having the sample moving continuously rather than in steps [44]. These scans were also implemented in an arbitrary-path version [45], admitting though that the highest resolution is still achieved with step

scans. However, an ultra-fast fly-scan implementation at the Argonne national laboratory [46] claims a 9 nm resolution, which is the same order of magnitude as record resolution, but reducing scanning times by a factor 450 compared to a step scan with the same dwell time.

A parallel, popular line of inquiry for ptychographic methods involves non-iterative approaches [47]–[50]. In fact, the approach of Wigner-distribution deconvolution, which is non-iterative, was a precursor of the ptychography studies, but revealed itself too demanding in terms of scan time [51], [52]. Although these have demonstrated their robustness to noise or promise faster reconstruction speed, they have yet to show results on experimental data.

### **Study of Noise in Ptychography**

Noise is the undesired signal overlapping with the measurement of a signal of interest. The measurement of a wavefield by an area detector can be modelled as a Poisson process, as the detector integrates over a certain sampling time the number of photons reaching the pixel area. This number has to be an integer (i.e. the wavefield is quantized), unlike the simulated wavefield. This discrepancy is referred to as a photon-counting noise. This noise can be added in Python to the pattern  $I$  with the function `'numpy.random.poisson(I)'` or in MATLAB with `'imnoise(I, 'poisson')'`. For each element of a 2D array, these functions sample a random integer value from a Poisson distribution having mean and variance equal to that element. For high values of means Poisson distribution approximates a Gaussian distribution with the same mean. The visual properties are: 1) noise is signal-dependent, i.e. the noise mask resembles the original image, implying that absolute noise is higher for higher intensities; 2) relative values of noise are lower for the low intensities. On the contrary, Gaussian white noise (independent of frequency) bears no signal dependence in its structure and the mean is not defined by the signal. A Gaussian process is typically used to model the electronic noise of the detector.

All deviations from the experiment's model can be considered sources of noise.

A classification of these experimental sources is reported in [53]. They can be grouped into: structured (parasitic scattering, dark noise), random (photon counting noise, detector noise), and outliers (bad pixels, bad frames, cosmic rays).

Dark noise and bad pixels pose no problem as they can be subtracted from the measurements. Random sources of noise have been the first to be considered and the concept of maximum likelihood was used to deal with photon counting noise [54], [55]. This random process can be modelled as a Poisson process. In this case the probability of measuring  $n_p$  photons on a pixel located in reciprocal space at position  $q$  given the incident wave with intensity  $I_q$  equals:

$$p(n_{pq}|I_q) = \frac{(I_q)^{n_{pq}}}{n_{pq}!} e^{-I_q}. \quad 2.21$$

Based on such probability, the maximum-likelihood defines a cost function for the whole set of measurements (pixels and frames) and aims to find the probe and object minimizing such a cost function. This algorithm is rightly labelled as a refinement as it cannot achieve convergence from a distant object only based on counting statistics properties, but must take over from a ptychographic reconstruction.

Other sources of noise can be the variation in the illumination for ptychography (which relies on the probe being a constant), and in sample shifts due to instability. Odstrcil et al. show that they are able to take these into account without significant increase in computational cost with their iterative least-squares solver [56], whereas the main merit of the advanced denoising reported in [53] is to deal with noise from parasitic scattering, bad frames, and cosmic rays.

### 2.2.3 Resonant X-ray Imaging

The sort of imaging discussed so far relates to off-resonance conditions. In that case, a single value for the energy of the monochromatic radiation impinging on the sample is chosen. Besides, this value is chosen far from the characteristic electron binding energies of the elements included in the sample.

In a resonant experiment, a value of energy in proximity of such energy is selected. The interaction with matter in this case requires a different discussion and has a

comprehensive mathematical description of scattering factors as a function of energy [57]. The practical feature is that the element shows a decreased scattering power around a resonant edge, as if fewer electrons contribute to scattering. The intuitive explanation relates to the fact that, provided with an energy exactly equal to the levels' difference, electrons are in an unstable position, having enough energy to leave the lower shell, but not enough to oscillate freely without decaying.

If several energy values are used, a new dimension is added to the collected imaging dataset. There are different options as to which energies should be selected and which imaging technique is used, and there exists a trade-off between sample size and scan duration.

If several scans are acquired at different energies around the edge with a resolution on the order of 1 eV or less, the fine structure is probed and the technique is a combination of spectroscopy (known as XANES, X-ray absorption near edge structure, or NEXAFS, near-edge X-ray absorption fine structure) and imaging methods. In the case of ptychography, that is also referred to in literature as spectro-ptychography. This strategy provides chemical sensitivity, as different species of the same elements behave differently in terms of absorption and scattering, provided that such effects are within detection limits. From a beamline-operation point of view, a near-edge scan can be automatized in a script, whereas a resonant scan at edges that are separated more than a few hundred eV requires a realignment of optics, which in most cases requires assistance of a beamline scientist.

There has been a number of imaging experiments exploiting resonance. Although STXM imaging experiments can very well be resonant, we focus here on the 2D and the more recent 3D CDI imaging. For the 2D case, the experimental demonstration of resonant full-field CDI is credited to Song et al. [58], then resonant ptychography demonstrations were provided with soft X-rays by Shapiro et al. on a  $\text{LiFePO}_4$  nanoplate [59] and by Beckers et al. on biological samples [60], and with hard X-rays by Hoppe et al. on gold nano-spheres [61] and Pt bubbles [62]. From an algorithmic point on view, Hirose et al. suggested an interesting paradigm in phase retrieval of resonant data [63]. They incorporated the Kramers-Kronig relations in phase retrieval (ePIE), as an additional constraint besides the overlap and the modulus constraint. They show in

numerical simulations and experimental data that this constraint helps to get faster convergence and better quality in the retrieved image. In 3D, as an intermediate step towards demonstration of magnetic tomography [64], [65], Donnelly et al. [66] were the first to demonstrate elemental sensitivity with resonant X-ray ptychographic tomography (RXPT) on a Co-coated polymer scaffold. In this demonstration they perform a tomographic scan at the Co K-edge (on-resonance) and one at 6.2 keV (off-resonance) and quantify the Co 3D distribution by a subtraction of the phase tomograms, normalized to the wavelengths. Following the same scheme, Ihli et al. went beyond the proof of concept by locating Fe accumulation within a catalyst. The near-edge 3D version, going by the name of spectro-ptycho-tomography, has been demonstrated relatively recently and it is obviously demanding in terms of scan duration and size of datasets to analyse. Wu et al., who performed spectro-ptycho-tomography on an organic sample [67], also point out, based on outcome of their experiment, that it is also demanding in terms of radiation damage. They only looked at the amplitude signal and only two energies, before and after an absorption edge of F to derive a F-map on a C support. They also provide a direct comparison with spectro-STXM performed with high-resolution zone plates, highlighting the advantage of spectro-ptychography. Hirose et al. used the above mentioned Kramers-Konig constraint in ptychographic phase retrieval on experimental 3D data [68], to track the oxidation state of cerium-zirconium oxide. Ref. [69] is the first example of spectro-tomography across two edges of two different elements.

#### **2.2.4 Tomography**

Tomography is the scanning modality that enables 3D imaging from reconstruction of a set of 2D projections of an object acquired from different angles. Although iterative algorithms exist for this operation, the most commonly used method for computed tomography reconstruction is the filtered back projection [70]. The method relies on the Fourier slice theorem, which states that a slice of the Fourier transform of the object taken along a certain angle can be obtained as the projection (mathematically defined as the Radon transform) in real space of the object along the same angle. Hence,



projections can be measured with a pixelated detector, Fourier transformed and summed up together to obtain the object. The filtering operation is necessary, however, because measured projections are sampled with a constant stepsize in real space, which yields a denser sampling around the lower frequencies in Fourier space. The effect of that is a smearing of the reconstructed object. This undesired effect is prevented by applying a low-pass filter to the backprojection.

The number of projections  $N_p$  that are necessary for reconstruction is provided by the Crowther criterion [71], which defines a relation between the achievable resolution  $d$  and the number of projections and the object's diameter  $D$ :

$$N_p = \pi D/d \quad \mathbf{2.22}$$

The standard acquisition scheme for ptychographic X-ray computer tomography (PXCT) is a two-step process in which 1) projections of overlapping illuminations are reconstructed from diffraction patterns via ptychography and 2) three dimensional reconstructions are obtained from such projections via tomographic methods. However, one can think of a 3D reconstruction performed in a single step. This approach has been demonstrated for full-field CDI [72], and is recently being applied to ptychography [73]–[76].

### **2.2.5 X-ray Beam Induced Current/Voltage (XBIC/XBIV)**

Besides structural and chemical properties of solar cells, it is obviously of interest to measure other parameters, directly related to their performance. A collimated beam of photons induces locally a current in a solar device, provided that the photon energy is higher than the bandgap of the element/compound active layer. This current is due to the charge carriers that are generated by photoabsorption and those that make it to the electrodes without recombining provide a measurement of the charge collection efficiency. This concept is behind the LBIC, EBIC, XBIC techniques where the beam-induced current is produced by an optical light, an electron, or an X-ray beam, respectively. Scanning a device area as in a STXM setup, a map of the charge collection efficiency can be obtained.

LBIC is a standard laboratory characterization technique, whereas the other two are more niche-like. More collimated beams can be produced with electrons and synchrotron X-rays, allowing for a higher resolution mapping of the device, but electrons do not have the penetration power of X-rays and the simulation of electron pathways is performed with Monte Carlo methods [77]. XBIC is part of a correlative approach to characterization of solar cells, which entails synchrotron in situ and operando studies [78]. After a first study demonstrating with statistical significance a correlation between performance at grain boundaries and Ga concentration in CIGS  $\text{Cu}(\text{In,Ga})\text{Se}_2$  solar cells [79], other materials have followed [80]. The full procedure of collecting fluorescence images to correlate to XBIC maps is thoroughly described in [81]. The induced currents are typically on the order of pA and it can be beneficial to use a lock-in amplifier to filter out noise. Despite the low magnitude of such currents, XBIC has been reported with some success in a laboratory setup [82], [83]. In that case, to enhance sensitivity, because of the exponential I-V characteristic, it can be helpful to measure the induced voltage rather than the current. However, whilst XBIC is proportional to photon intensity, there is a non-linear relationship between XBIV and photon intensity, which does not directly permit to discriminate well performing cells [84].

### **2.2.6 Laminography**

Laminography is an imaging modality in which projections of a planar device (a flat specimen) are acquired for different angles and (differently from tomography) the rotation axis of the sample is not perpendicular to the beam. This geometry has been investigated with synchrotron radiation by Helfen et al. [85], [86] and is depicted in Figure 2-3 where it is compared to tomography.

For planar devices laminography has the clear advantage of not requiring as complex a sample preparation as for tomography. Tomography of flat samples has the disadvantage of missing the angles for which the sample plane is close to the beam direction, when the beam is highly attenuated. In fact, in tomography the ideal geometry is a cylinder, which permits uniform transmission and counts for all angles. Therefore a pillar is usually extracted from a planar device. That is not necessary in laminography as in that geometry the sample thickness remains constant for all angles. In reciprocal

space, rotation of a flat sample produces a missing wedge for a tomographic dataset and a missing cone for a laminographic dataset.

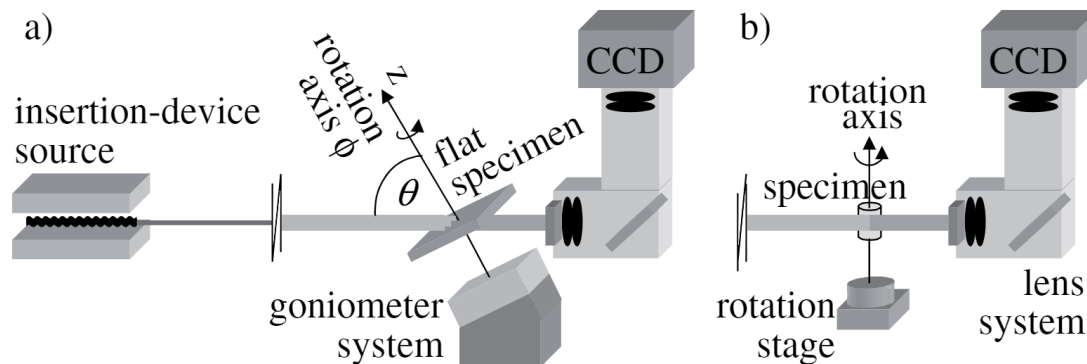


**Figure 2-3.** Comparison between a laminographic (a) and a tomographic (b) scan setup as implemented at beamline ID15, ESRF as in [85]. The rotation axis of the sample is not perpendicular to the beam in the laminographic setup, whereas it is in the tomographic setup. Reprinted with permission from [85]. Copyright (2007) Wiley-VGH.

A direct comparison between tomographic and laminographic reconstruction data is provided by Xu et al. [87]. Their paper quantifies the advantage of the laminographic setup for a flat sample both in terms of artefacts (more or less distinguishable) and overall signal-to-noise ratio (SNR). In particular, they estimate in simulations the SNR as a function of the rotation angle in a tomographic setup, comparing it to the tilt angle of laminography. They find that in laminography the SNR of all projections is similar, whereas in tomography it is only equal to that of laminography when the tilt angle of laminography is reached, but is generally higher for all other angles, thus making the average SNR of projections higher for tomography and producing more visible artefacts. Furthermore they hint to the advantage of laminography also for fluorescence measurements.

Interestingly, laminography has recently been demonstrated even on a conventional industrial laboratory micro-CT scanner, without resorting to any specialist equipment [88]. Projections are acquired with a cone-beam illuminating a LEGO sample and the conjugate gradient least square method was used for the reconstruction. Moreover, the authors account for uncertainty of center of rotation, sample-detector distance, and tilt angle and describe the artefacts that these produce, which are not very well known for this particular setup.

Besides, projections can be acquired in all propagation regimes with the same techniques used for tomography. It has therefore been demonstrated simultaneously with absorption, phase-contrast and fluorescence [89], and most recently the group at cSAXS published their ptycho-laminography setup [90]. In both papers it is emphasized the concept of hierarchical imaging, which represents another advantage of laminography. Having an extended sample it is possible to image a wider area (on the order of  $\sim 100 \mu\text{m}$ ) on a coarse scale ( $\sim 1 \mu\text{m}$ ), and then zoom on the most interesting features with the same scale and record resolution that can be achieved in PXCT. In [90] it is also addressed the challenge of the missing cone in reciprocal space. The use of priors related to the known sample composition and shape, the consistence with retrieval at coarser scales help convergence and compensate for the missing cone.

### **2.2.7 Note on optics**

We have mentioned in relation to STXM that small spot sizes for the beam are crucial. In this section we discuss one kind of optics that achieves best performance in this regard. A description of other optics that are typically used in an imaging experiment is beyond our scope.

#### **Multilayer Laue lenses**

While lensless coherent diffractive was developed to overcome the limits imposed by optics for image formation, the recent developments w.r.t multilayer Laue lenses (MLL) challenge this paradigm as they promise focus sizes comparable to the current resolution records.

Like KB-mirrors [91], [92] they are used in pairs, with one focusing horizontally and the other vertically. Like Fresnel zone plates [92], they are diffractive optics, although they exploit a more precise method for fabrication. Instead of photolithography, they rely on deposition by sputtering of thin stacked alternating layers of an opaque and a transparent material (**Figure 2-4a**). The size of these layers is designed to fulfil the zone-plate law that allows all reflected rays to interfere constructively in the focus, and in the wedge geometry (**Figure 2-4b**) the angle of each bilayer is designed to fulfil Bragg's law locally.

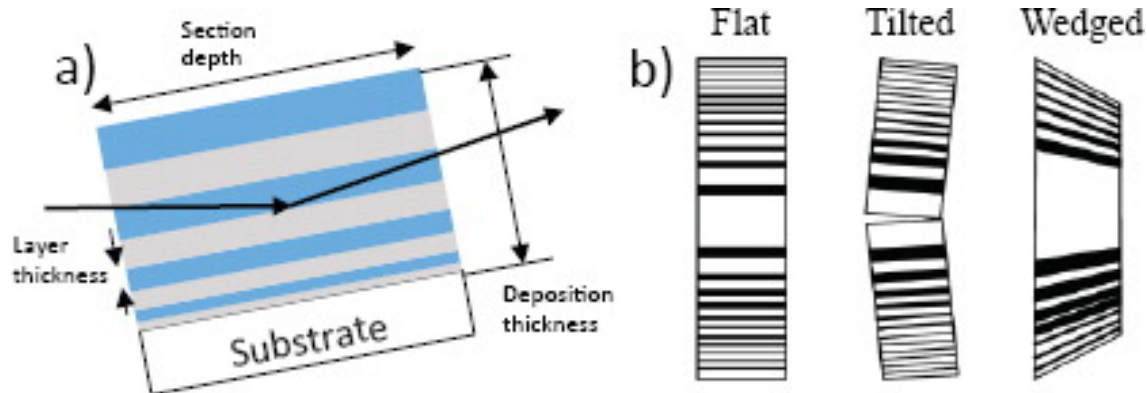


**Figure 2-4. Multilayer Laue Lenses. a) the structure of a MLL is composed of alternating transparent and opaque layers deposited on a substrate and following a precise scaling law. b) three different geometries of MLL: flat, tilted and wedged. Reprinted with permission from [93].**

Record focus size have been reported in recent years. Bajt et al. achieved a two dimensional focus of  $8.4 \times 6.8 \text{ nm}^2$ , and suggest that 1 nm focusing can be reached [94]. They have also been demonstrated with hard X-rays up to 34 keV where they are claimed to become more efficient compared to other X-ray optics [95]. Kubec et al. have experimentally demonstrated the higher efficiency of lenses with the wedge over the flat geometry (44% vs. 28 %) for these lenses [96]. Like in the other cases reported, they have noticed significant lobes in the beam profile. However, as they are still in a development phase, they present several limitations which make them still not available for general users. The focused beam is highly divergent, implying a restrictive operational distance. Other downsides are a high sensitivity of alignment with respect to beam energy.

Their application is particularly relevant for XBIC and fluorescence studies as they rely on an STXM setup, whose resolution is limited by the focus size of the beam. For that case, the observed side lobes represent a downside, which can perhaps be mitigated by probe deconvolution. However, like in [94], they can also provide sufficient overlap for a valid ptychographic reconstruction.

## 2.3 Reconstruction quality in X-ray imaging

In this section, we discuss the concept of resolution and quantitiveness, in relation to the way we have evaluated them in our simulation and experimental work.

### 2.3.1 Resolution Assessment

As well explained in [97], the idea behind the estimation of resolution with a full-width-half-maximum method (FWHM) is to consider a line profile across a sub-resolution object, ideally a point-like source. When such an object is fitted by a Gaussian profile, the FWHM resolution is defined by identifying the maximum and measuring the width of the profile at half maximum of the gaussian.

An alternative to this measurement is evaluating the profile across an edge, and is referred to as edge response. A sharp edge is also a sub-resolution object and its image can show a transition that is less sharp than the physical edge. In that case one can refer to the 90-10% criterion to estimate resolution.

That requires evaluating the end values of the transition and measuring the distance between 10% and 90% of the gap between them. Another possibility in the case of an edge is to evaluate the FWHM of the gradient.

Fourier ring and shell correlation (FRC and FSC) are the other popular tool to evaluate resolution of images and volumes. These methods compares two images or volumes in Fourier space, and evaluate the correlation between features in the same range (rings or shells) of spatial frequencies  $R$ . In formula:

$$\text{FSC}(R) = \frac{\sum_{R \in R_i} [F_1(R)F_2^*(R)]}{\sqrt{\sum_{R \in R_i} |F_1(R)|^2 \sum_{R \in R_i} |F_2(R)|^2}}, \quad 2.23$$

where  $F_1$  and  $F_2$  are the Fourier transform of the two volumes,  $R$  is the reciprocal coordinate,  $R_i$  is the  $i$ -th shell, and  $*$  denotes complex conjugate.

When this correlation is plotted as a function of spatial frequencies, the intersection with a threshold yields the assessment of resolution. If the image under test is compared to the ground truth, then the (lower) 1-bit threshold should be considered. If, like in the

case of tomography experiment, a ground truth is not available, two sub-tomograms obtained from two subsets of measurements are correlated, and the intersection with the  $\frac{1}{2}$ -bit threshold must be considered.

It is important to point out is that these criteria to estimate resolution obviously do not necessarily provide the same value. The same method and criterion should be used to compare different images or different portions of an image.

### **2.3.2 Quantitativeness of Ptychographic Nanotomography**

The quantitativeness of ptychographic nanotomography is evaluated as a function of resolution by Diaz et al. in [98]. Using a sample of known composition and density, they showed that indirect measurements of the mass density relying on measurements of the real part of the refractive index, were accurate up to a 2% error. Besides this final claim, other important points are made with respect to the refractive index measurements. Namely, it is shown that once the deviations of the real part of the refractive index in a volume of the sample of uniform composition are plotted in a histogram, they fit well a Gaussian distribution and that the standard deviation of this distribution is very similar to that of any region of air of the same volume. This standard deviation depends on the voxel size, and increases (slower than expected, because of the correlated noise introduced by the reconstruction method) for decreasing voxel size. These points highlight that the variation on  $\delta$ , and likewise on the indirectly measured electron density, can easily be around a tenth of the measured value, and a good way to estimate the variation can be to evaluate measurements of uniform regions, air or sample. It is not strictly clear whether this variation is independent of the measured density, i.e. whether low  $\delta$  values are more or less affected than high ones. It should also be pointed out that values reported in [98] refer to an earlier stage of the beamline and to our knowledge, there are not any more recent papers specifically assessing quantitativeness of nanotomography at higher resolution. The above mentioned study evaluates tomography based on projections with a 43.6 nm pixel size, whereas tomography is now routinely performed at higher resolutions. Rule of thumb suggested by beamline scientists (cf. personal communication, A. Diaz, Aug 2018) is not to expect to distinguish phases with a contrast below 5% in terms of refractive index.





### 3. Ultramicroscopy of Solar Cells

The solar cells we have investigated present different features and hence different lines of inquiry, which we highlight in this chapter. As solar cells, electrically, albeit with different parameters, they behave at the same way, i.e. as a photodiode, illustrated by the current-voltage (I-V) plot illustrated in Figure 3-1. In the dark, they present the I-V characteristic of a p-n junction, with current rising exponentially with an applied voltage and switching on at a characteristic value which depends on the combination of materials used. Plus, they are photosensitive, in that an amount of charge carriers becomes available when illuminated. Electrically, this makes these devices active, i.e. the I-V characteristic shifts into the 4<sup>th</sup> quadrant and they produce power. Their performance is fully characterized with a few essential parameters (see Figure 3-1), whose names are almost all self-explanatory: open-circuit voltage,  $V_{OC}$ ; short-circuit current density,  $J_{SC}$ ; the maximum power point where the cell yields power per area equal to  $P_{MPP} = J_{MPP} \times V_{MPP}$ ; fill factor  $FF = \frac{J_{MPP} \times V_{MPP}}{J_{SC} \times V_{OC}}$ ; and the power conversion efficiency  $PCE = \frac{P_{MPP}}{P_{IN}} = FF \frac{J_{SC} \times V_{OC}}{P_{IN}}$  with  $P_{IN} \approx 0.1 \text{ W/cm}^2$  being the solar irradiance.

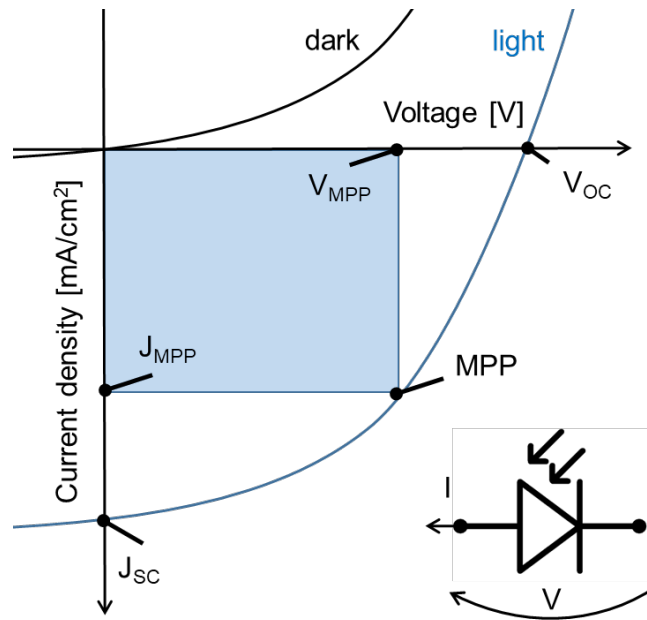


**Figure 3-1.** I-V characteristic of a solar cell. The active sign convention is often used for solar cells in order to quote a positive number for  $J_{SC}$ .

### 3.1 Organic Solar Cells

The figure of merit that is most often quoted about organic solar cells (OSC) is their energy-payback time, which is the amount of time an energy technology takes to recover the energy spent to produce it in the first place. This time is much shorter for OSC compared to Si solar cells (roughly 30 vs. 100 days), or even to thin-film technologies such as amorphous Si or CdTe [99].

It is an easily scalable technology because of roll-to-roll fabrication process and its practical installation [100]. Given these strengths, the issues that such technology needs to address are mainly efficiency and stability. The 10:10 goal (10% efficiency and 10 years stability) [101] was achieved almost 10 years ago. Lately a 17% record efficiency has been achieved [102], however there is still the gap to fill between champion lab devices obtained with low throughput deposition techniques that are not fully scalable and those obtained with a roll-to-roll ready deposition technique.

The basic working principle of an organic solar cell can be summed up as follows [103]:  
 1) charge generation. An exciton, i.e. a bound excited electron-hole pair, is generated by a photon with energy higher than the difference in energy levels between HOMO and

LUMO; 2) Exciton diffusion. An exciton can diffuse up to its diffusion length  $L_D$  (on average), which is on the order of 1-10 nm [103], before recombining; 3) Exciton dissociation. If the exciton runs into a donor-acceptor interface, separation into free carriers (also called polarons) occurs 4) Charge transport. Free carriers are swept towards the electrodes by the internal electric field induced by difference in work functions.

These steps highlight the main difference w.r.t. to classic semiconductors, where the photo-absorption of a photon produces a couple of charge carriers that are only weakly bound.

### **The importance of morphology control**

A fundamental breakthrough for OSC came when it was understood that mixing in a blend the donor and the acceptor, rather than having the acceptor layer on top of the donor layer, would boost the efficiency by an order of magnitude [104], [105]. It was soon understood that the morphology formed by this blend plays a role in the efficiency of the solar cells. The acceptor-donor domains that are formed need to find a certain balance for an optimal performance of the cell. The success of the blend was ascribed to the presence of smaller domains, as the excitons needing an interface to separate had an increased chance, but there is a trade-off between charge generation and charge transport. The bilayer structure achieves poor charge generation, but provides efficient charge transport. All carriers generated at a distance bigger than the exciton diffusion length ( $L_D \sim 10$  nm) would recombine before separating [106][107]. Therefore carriers contributing to charge transport are actually created on a thin layer of  $L_D$  at the interface.

The nano-interdigitated structure of Figure 3-2c has been suggested as ideal for charge transport *and* charge generation [108]. Implementing precisely such a structure is unrealistic, but the idea of having long tracks responsible for charge transport keeping a transverse size that allowed for excitons' charge separation was supported by the TEM investigation showing nanorods or fibrils with such thickness [109], [110].

Zhao et al. analyse and discuss morphology control and characterization in a recent review [111], making several points. First, that the nanomorphology is affected by many

parameters of the donor acceptor-blend, e.g. solubility, crystallinity, miscibility, and by the film processing that turns it into a solar cell.

Then, that no single characterization technique is able to provide full information about a morphology, at different scales. They refer to the morphology of nanorods or fibrils that were highlighted by others as a “3D charge highway” for the cell. Most of the examples come from TEM and some are shown later. Finally they report the need for novel characterization techniques for the multilength scale morphology that help understand further the relation between morphology and device performance.

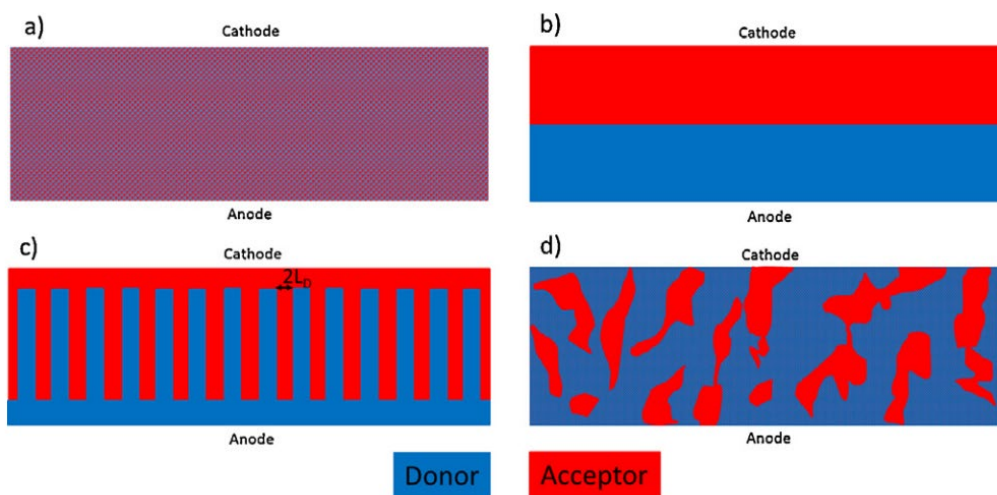


**Figure 3-2. Schematic of nano-morphology for the bulk heterojunction. a) fine mixture, b) bilayer, c) ideal morphology d) typical morphology after annealing of the organic blend. Reprinted with permission from [108].**

### The challenge of 3D X-ray imaging

Imaging of the morphology's nano-domains is challenging for three main reasons:

- There is weak contrast between the phases,
- The domains are small in size,
- As organic material it is susceptible to radiation damage.

However, OSC have been investigated with some success with X-ray ptychographic tomography [112], [113]. The resolution achieved in these cases (20 nm) was such to highlight with sufficient detail the layer stack of several layers, which were clearly

distinguishable and segmentable thanks to the astounding quantitiveness of the technique.

However, the active layer, arguably the most interesting part of the stack, could only be imaged in a limited number of voxel, with a resolution insufficient to resolve the morphology of the materials composing it. Some limitations are due to the intrinsic state of the technique. In 2D, ptychography itself, can achieve around a few nanometers resolution, which lowers to 10 to 20 nm roughly as an order of magnitude, in 3D. These record resolutions have been achieved on non-biological or inorganic materials. The limit imposed by radiation damage for coherent diffractive imaging has been discussed by Howells et al. [114]. As diffraction peaks of biological/organic samples fade with increasing dose, based on surveyed literature and their own experiments, they reported an empirical relation for degradation:

$$\text{dose [Gy]} = 1 \times 10^8 \times d \text{ [nm]}, \quad \mathbf{3.1}$$

connecting the maximum tolerable dose expressed in Grey to the aimed resolution  $d$ . Bragg peaks from higher resolution than  $d$  would not be distinguishable for the dose of Equation **3.1**, defined as the dose causing 50% spot-fading at resolution  $d$ . On the other side, based on the Rose criterion [115], they define a required dose for imaging, which they find to follow the trend  $d^{-4}$  in case of a coherent beam. The intersection between the trend of required dose for imaging and maximum tolerable dose marks the limit of what can be imaged before damage. They conclude that the limit for biological samples is not better than 10 nm.

It needs to be pointed out that, despite being often quoted as a general rule, this result is calculated for a certain protein against a background of water for X-ray energies of 1 keV and 10 keV. It might be questioned whether this result is applicable to a specific mix of polymers and in the soft X-ray regimes. Besides, the criteria for spot visibility and for imaging remain more or less arbitrary and do not account for later developments of phasing algorithms. Like Odstrcil points out in his thesis [116] the Rose criterion imposes a SNR of 5 for visibility of an object, but in CDI there are methods to improve resolution based on cumulative statistical analysis of the whole diffraction dataset [54].

This has in fact motivated our effort towards a comprehensive simulation framework, able to predict success of phase retrieval based on contrast, dose, flux, coherence. Finally we note that the concept of in situ CDI mentioned in section 2.2.2 might be particularly interesting for degradation studies and particularly for samples that are more vulnerable to radiation damage. In fact, as can be expected, radiation damage occurs first on the smallest structures to progressively affect longer range order [114]. In turn, this suggests that in an in situ degradation study, any wider structure less affected by radiation damage and containing the higher resolution fullerene domains and nanorods, might act as a static part, to be used as a constraint for phase retrieval of the dynamic changes of these finer structures.

### **3.1.1 Studies on organic blends**

Given the performance gap between lab- and large-scale devices [117], one purpose of these characterization studies is to find the crucial features of record devices. These could be eventually reproduced on devices made with roll to roll techniques. For this effort a wide variety of techniques has been exploited [118]. In the following we report some X-ray imaging studies and some examples from electron microscopy.

#### **X-ray imaging studies**

Films of F8T2-PC<sub>71</sub>BM annealed at different temperatures were probed with STXM at the C-edge 284 eV in [119], to quantify the degree of mixing of fullerene and domain size of the fullerene aggregates. They use energy-filtered TEM (EFTEM) data at S edge [120], which highlights the F8T2 matrix, to complement this data and conclude that higher mixing but not the domain size positively affect efficiency-related parameters. Van den Brande et al. [121] and Patil et al. [122] used 2Dptychography to study in situ the annealing process of the P3HT-PC<sub>61</sub>BM blend. It is known that thermal annealing produces a coarsening of the P3HT-PCBM morphology [122][109], and the authors were able to observe changes in domain sizes, but only at later steps in the annealing process, i.e. once they were sufficiently large. They point out that in their experimental conditions the achieved resolution (ca. 100 nm) was limited by radiation damage mostly,

as it did not clearly improve by increasing the exposure time or reducing the step-size. They mention the 'water window' for ptychography [123], i.e. in soft X-rays in the range between the K-edges of C and O as one of the viable options to improve resolution. Another option to enhance contrast, and thus potentially also the resolution, is the use of resonance, and chemical contrast in polymers has been demonstrated long ago in a spectroscopic STXM setup [124]. However, only very recently, Savikhin et al. [125] have had better success with ptychography using soft X-rays in the 700-800 eV range to investigate films of polymer:fullerene (P7B7:PC<sub>70</sub>BM) and polymer:polymer films (PII2T:PNDIT and PII2T:PPDIT). The mixture P7B7-PCBM is purposely chosen because its surface morphology has been imaged with atomic force microscopy (AFM) and is well known to form domains of 50 to 300 nm size, significantly larger than the nanorods of the best performing organic bulk heterojunction. The important result is that they were able to image the sub-surface morphology of these blends (Figure 3-3A and B), with a resolution between 30-50 nm and without observing radiation damage (Figure 3-3 C). According to the authors, this result allows for an increase of the exposure time, which could enable, combined with the use of cryo-stage, reconstructions below 10 nm. As they did exploit an enhanced contrast due to resonance of K-edge of F atoms, which are only contained in the P7B7 matrix, they suggest that a spectroscopic investigation requiring multiple projections, is also a future viable step.

It is worth pointing out the challenges of their outlook. Although the cryostage [126] helps preserving samples and minimizes thermal drifts that would cause sample instability and reduce the expectable resolution, it cannot achieve yet the same performance as at room temperature. However, so far for ptychography, sub-20 nm resolutions have been demonstrated in 2D for biological samples in a cryo-setup. A 3D case is not discussed by Savikhin et al. but it is worth pointing out that the number of necessary projections to acquire is significant and radiation damage might start to show after a few projections. As that would even change the sample and therefore hamper a tomographic reconstruction, the use of a cryo-setup would be more than recommendable in this case. So far a sub-30 nm resolution has been demonstrated in the 3D case, but only for high-contrast (although biological) materials.

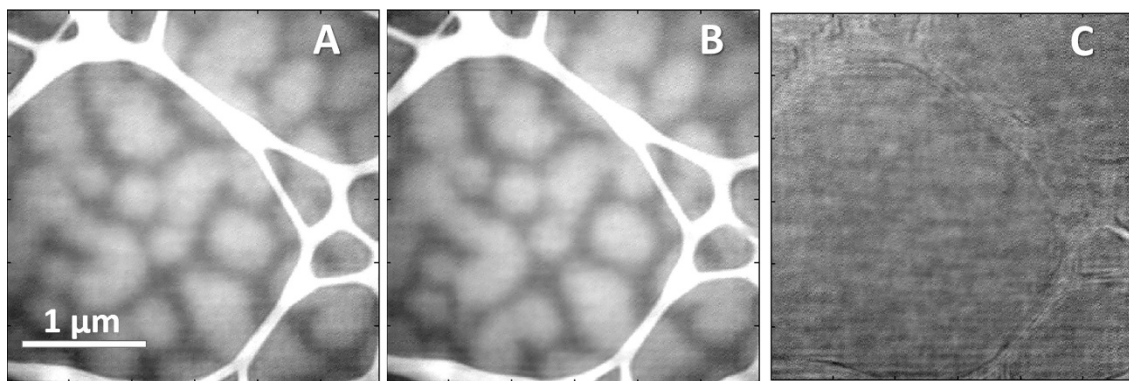


**Figure 3-3. Ptychographic projections through films of PTB7:PC<sub>71</sub>BM blend. Phase images are taken consecutively to test for beam damage: first image (A), second image (B), difference between the two (C). The white web is the lacey carbon supporting the sample, whereas the bright areas with varying size (up to 300 nm) are fullerene domains distributed in a P7B7 matrix. Reprinted (adapted) with permission from [125]. Copyright (2019) American Chemical Society.**

### **Electron microscopy literature**

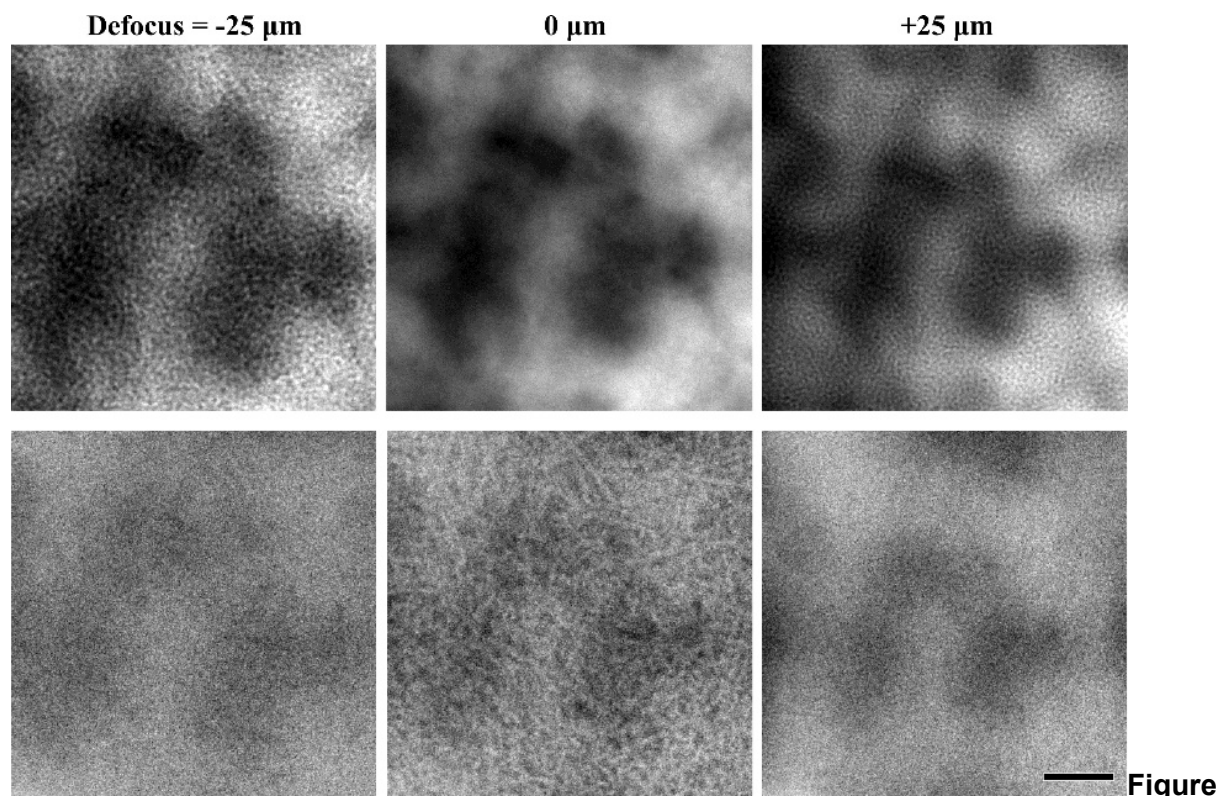
Electron microscopy is not affected by the critical point of size for the nanodomains of the morphology, as the resolution typically achieved in this field is easily below the nanometer.

Despite the above mentioned challenges for imaging, van Bavel et al were able to image with electron tomography the nanomorphology of P3HT:PCBM [127] before and after annealing. Their investigations highlighted the formation after solvent evaporation of a 3D nanoscale network with high crystallinity order.

The same structures were imaged by Herzing et al. [128] exploiting the spectroscopic contrast detected by EFTEM. These structures are shown in **Figure 3-4** and are best visible in focus and with the jump ratio of S (19 eV). The technique achieves elemental sensitivity by tracking only the electrons losing a certain energy (corresponding to certain elemental transitions), and in this case the authors take advantage of the lack of S in PCBM, to obtain S maps that are in fact maps of P3HT. The authors claim with this approach a contrast enhancement between phases and a consequent 'relaxation of the dose requirement' for imaging of organic blends. The contrast enhancement is also shown by other examples in literature of 2D EFTEM of organic blends, which refer to



the most studied blend P3HT-PCBM [129] [130], and rarely to others [120]. With respect to radiation damage, the authors of [130] claim them to be less radiation sensitive. In fact, they speculate that the heavy S atoms are less mobile than the organic matrix in which they are embedded and which is more likely to be damaged. In our group, Corazza et al. used EFTEM to enhance contrast between P3HT and PCBM, exploiting differences around the main peaks of the C absorption spectra [131], but without collecting S maps. Energy filtering was also more recently applied to scanning electron microscopy (SEM) by Masters et al. to P3HT:PCBM, achieving sub-nanometer resolution [132].



**3-4. EFTEM of P3HT-PCBM. Scale bar is 200 nm. Rows are obtained from different energy selections (0 and 19 eV), columns correspond to different focus distances. Reprinted (adapted) with permission from [128]. Copyright (2010) American Chemical Society.**

The most recent example we mention involves the 4D scanning transmission electron microscopy (4D STEM) [133], in which 2D images of a converged electron probe are recorded over a 2D grid of probe positions. The same setup has been used to

demonstrate electron ptychography [134]. Recently, Panova *et al.* demonstrated that 4D STEM can be successfully applied to any semicrystalline or ordered organic material [135]. As a scanning technique, the field of view is increased compared to EFTEM, which allows for characterization of  $\mu\text{m}$  wide area, and providing diffraction patterns paves the way for electron ptychography of organic blends.

### **3.1.2 Our experiment proposal**

After surveying the most suitable beamlines for the experiment, in September 2018 we submitted a beamtime proposal to the beamline 7.0.1 (COSMIC) of the Advanced Light Source, Berkeley lab. The beamline was chosen for the availability of ptychography, tomography, and tender X-rays ( $\sim 2.5$  keV).

We proposed a resonant ptychographic tomography experiment on a sample of an organic solar cell, with a blend of new materials that have recently reported record efficiency. The core of our proposal read:

‘Our hypothesis is that exploiting resonance of an element only present in one phase, combined with a proper choice of the materials used for the blend, can sufficiently enhance contrast to resolve the nanodomains composing the active layer of OSC. Interestingly, non-fullerene, small-molecule acceptors have emerged as a new branch of materials able to achieve record efficiency of 13% [136], and among them, PDI derivatives do not contain sulfur. Furthermore, non-fullerene acceptors have shown remarkable performance with PffBT4T-2DT as donor [137]. Therefore, we propose to investigate an (SF-PDI2) – (PffBT4T-2DT) based solar cell.’

Among contrasting judgments of the reviewers, the proposal was not granted beamtime. The main reasons relate both to the expected outcome of the experiment and to feasibility. One reviewer, in particular, argued that results of EFTEM on this sample are a prerequisite for our proposal. Senior researcher S. Bredmose and PhD student S. Colding-Jørgensen performed EFTEM and electron tomography on the sample. PhD student M. Fernandez prepared the samples.

### 3.1.3 EFTEM Investigation on non-fullerene blend

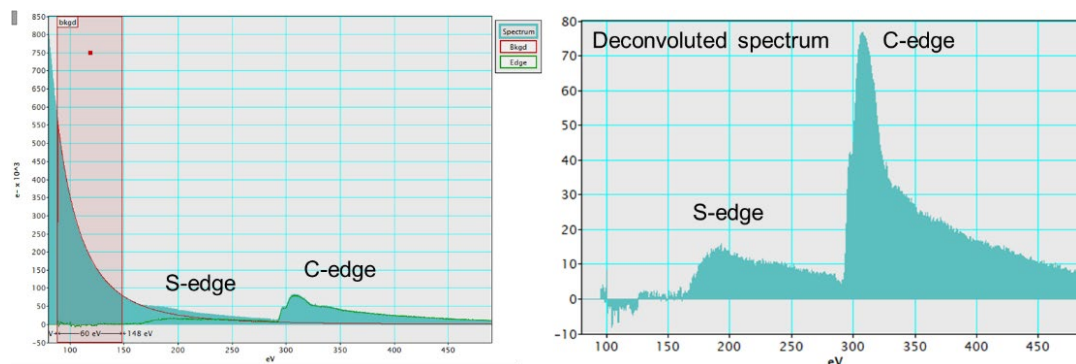


**Figure 3-5.** Electron energy loss spectrum for non-fullerene blend. The background (red area, left figure) covers the much smaller peak of the S-edge, which are however clearly distinguished once deconvoluted (right figure).

#### Methods

Samples were prepared according to a procedure that is standard for similar experiments [130], [138], in which: 1) a PEDOT:PSS thin layer is spin-cast on a Si wafer; 2) the organic blend is spin-cast on the PEDOT:PSS and dried; 3) the wafer is put in water where the PEDOT:PSS dissolves and samples of the organic thin film float off; 4) samples are picked up on TEM grids.

For the data analysis peaks relative to S and C can be identified in the spectrum once it is deconvoluted. The post-edge S peak is expected at 185 eV and is the one that most contributes to signal. The TEM microscope was operated at 80 keV with an exposure time of ca. 60 s.

## Results and discussion

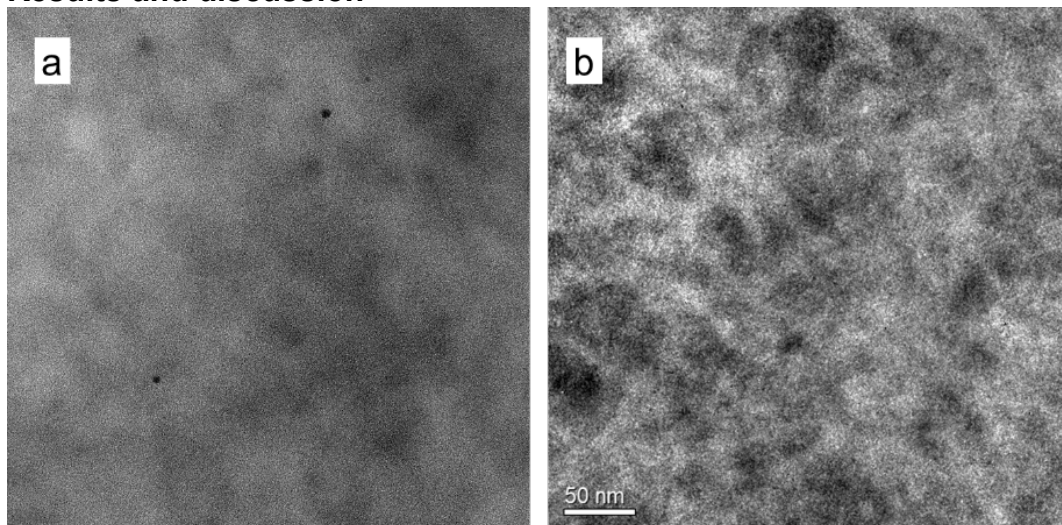


**Figure 3-6. EFTEM Image using zero-loss peak (a) and S-edge jump ratio (b).**

**Figure 3-6** shows the obtained zero-loss peak and the S map. The S map obtained with EFTEM is of quality comparable to that shown in [130]. The structures highlighted have similar dimension (10 to 20 nm) to the one observed in previous studies, not only from EFTEM studies, but also deduced from small angle X-ray scattering (SAXS) studies. The slightly lower clarity of the features can be attributed to a higher thickness of the employed samples (approx. 200 nm vs. 70 nm).

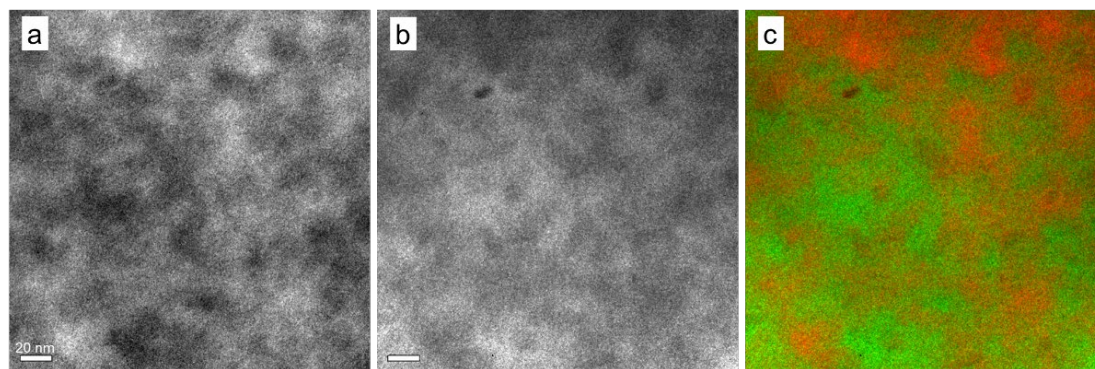


**Figure 3-7. S-edge jump ratio image (a), C-edge jump ratio image (b), Color mix with S=red and C=green.**

The comparison of S maps with C maps (**Figure 3-7**) shows that energy filtering at S-edge is necessary to highlight the structures of interest, as differences at C-edge do not yield sufficient contrast between the polymer and the small molecule to highlight features of the nanorods. In fact, as there is no apparent correlation between S-maps and C-maps or zero-loss maps, we conclude that energy-filtering at S edges appears as

the only reliable strategy to achieve meaningful contrast. It was verified that the same area would withstand radiation damage by taking two consecutive images of the same spot. No clear difference was observed, which encouraged a subsequent 3D investigation. However, it was not verified that the same spot would withstand a longer exposure.

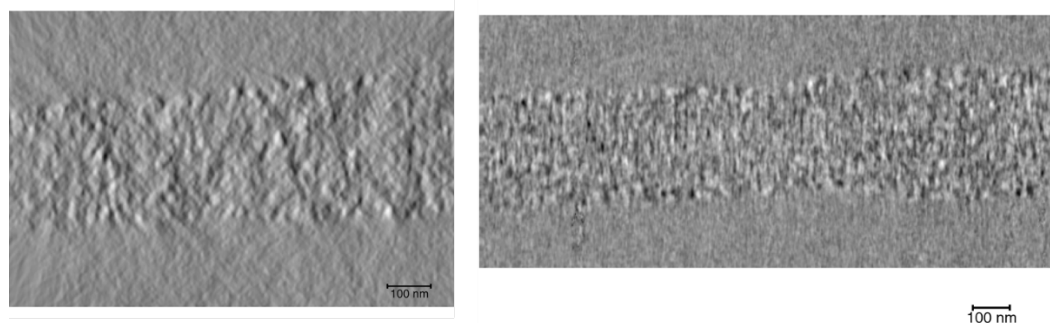


**Figure 3-8. Two slices of reconstruction of electron tomography.**

However, the tomography reconstruction based on mass thickness contrast, as described by Andersson et al. [139], does not seem to give a significant result (**Figure 3-8**). The features highlighted show a structure similar to that of the background. As observed by Herzing et al. on P3HT:PCBM [128], also for our blend it might be necessary to use energy filtering.

## 3.2 Kesterite solar cells

In literature, the cells we have studied go by the name of their stoichiometry ( $\text{Cu}_2\text{ZnSnS}_4$ , shortened as CZTS) or their crystalline structure (kesterite, after the mineral). At this stage of development of this technology, a considerable effort is still put in verifying that they are fully CZTS and kesterite. Cells with imperfect crystals or secondary phases can still give a few percent efficiency, but most of the cell needs to have the right stoichiometry and crystal structure.

Kesterite solar cells have been proposed as an alternative to other thin-film technologies like CdTe and CIGS [140], which achieve good efficiency and energy payback time, but contain toxic and/or rare materials.

Kesterite is reported among the emerging photovoltaic technologies and the last efficiency record of CZTS is of 11.4%, notably on a  $0.5 \text{ cm}^2$  area [141]. Kesterite is potentially an interesting candidate as a tandem partner for Si solar cells, assuming that

the best partner should be selected on the basis of their spectral efficiency – their efficiency resolved by the wavelength [142]. Kesterite has a tunable bandgap of 1.5 eV and a spectral efficiency that can very well complement that of Si (1.12 eV).

The ways kesterite is produced are reviewed in [143].

### **The quest for non-idealities**

An eminent paper by Scragg et al. [144] states what follows about the material characterization: ‘Unfortunately, detection of small quantities of secondary phases, especially confined to interfaces, is difficult for various reasons (e.g., overlapping signals in XRD and Raman, a small interaction volume, etc.) and is even more complicated if the CZTS films are nonstoichiometric.’

Siebentritt and Schrorr [145] described it as a challenging material because ‘one of the major challenges for these solar cells is the growth of single phase material, particularly because it is very hard to clearly detect secondary phases’. They also point out that the single phase region of kesterite is much narrower than for CuInSe<sub>2</sub>, and that even in the CZTS stoichiometry the structural variety of stannite can be detrimental because of a lower bandgap.

Another culprit for kesterite is the Cu/Zn disorder [146], i.e. swapping of Cu and Zn atoms within the crystal cell, and its effects were discussed in [147], [148]. Their conclusions are that these kind of defects are very likely to occur and are responsible for bandgap fluctuations contributing to the  $V_{oc}$  deficit.



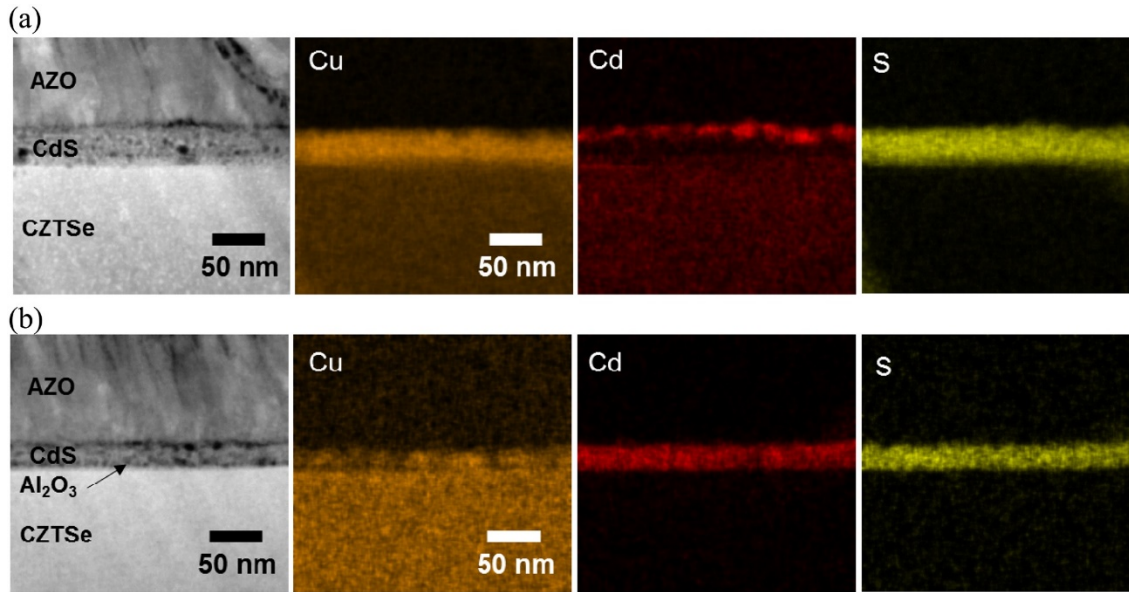


**Figure 3-9. STEM and energy dispersive spectroscopy (EDS) images of kesterite cells with and without an aluminum oxide passivation layer between the CdS and the CZTSe layers. The authors show that this layer prevents intermixing of Cd and Cu. Reprinted with permission from [149].**

A synthetic review of the way secondary phases are found in kesterite is given in the introduction of chapter 5.

The paper we are presenting shows an unprecedented combination of resolution, elemental sensitivity and size of the probed volume. These are some parameters of interest, but it is useful here to provide a context.

- TEM images have uniquely high resolution, showing even the single atoms in the crystal [150][151]. However the volume that can be examined is not representative of a full cell as it barely covers a small portion of a grain. However, crystal defects are out of reach for direct space X-ray imaging, and, unless a different configuration induces a measurable strain on the lattice, they are also out of reach for reciprocal space imaging.
- Berg et al. [152] answer in the most direct way the question about detectability of secondary phases. However, their important results do not relate to imaging. Their approach was to choose samples with selected amounts and kinds of secondary phases to inspect their detectability via Raman and XRD.

- Figure 3-9 shows an example of characterization with elemental sensitivity. This property is essential in this case for the authors to assess the intermixing of Cu and Cd.

The ideal imaging experiment proves to be sensitive to presence of all possible secondary phases and compares a good sample to a bad sample to find differences. However, in synchrotron imaging the number of samples that can be inspected is limited and a single sample containing all of the interesting secondary phases is impossible to fabricate for the same reasons it is hard to make pure kesterite, i.e. the conditions that allow different phases to form cannot be controlled on the scale of a nano-tomography sample. In short, it is hard to build a case around a bad sample.

In the following we present some complementary results we obtained on kesterite.

### 3.2.1 X-ray fluorescence of CZTS

A sample including only a CZTS layer, deposited on Mo-coated soda lime glass, was examined in a expert user-commissioning beamtime at NanoMax, MAX IV. The sample was scanned in an STXM setup, with the kesterite surface orthogonal to a 10.7 keV beam. The beam was focused to a 100 nm size (FWHM) with a Fresnel zone plate. Fluorescence was collected with a Si detector in a transmission geometry and diffraction patterns were recorded with a Pilatus 100K placed downstream of a 4.3 m flight-tube pressurized with He.

Fluorescence maps were analysed with PyMCA [153], accounting for the experimental geometry and the sample structure and composition, which allow to include self-absorption phenomena in the analysis. A ptychographic reconstruction of the diffraction patterns was not possible because of low scattering from the sample and/or loss of coherence at a certain point, due to an unexpected opening of the beam defining slits. Fluorescence maps on a 20×20 μm<sup>2</sup> area revealed a few spots with inhomogeneity in Cu and Zn concentration. A subsequent scan of one of these on a finer scale and a smaller area is reported in the Cu and Zn maps in **Figure 3-10** a and b, respectively. All the elements contained in the sample were not sufficient to fit well the measured spectrum of counts **Figure 3-10c**. The inclusion of W among the elements to fit was required to fit unassigned peaks. The W counts were most likely due to parasitic



scattering from the order sorting aperture, which could have been verified with an empty measurement.

The Cu excess was ascribed to one of the CuS droplets that were found on the surface of CZTS and were previously imaged with SEM. The Zn excess might be ascribed to the ZnS particle observed with RXPT, as a Cu excess was observed on top of a ZnS grain. It was not possible to detect any edges of grains in this imaging modality, possibly because of the geometry and/or the fluctuations in fluorescence counts. The Cu-Zn ratio derived from the background of fluorescence maps matched previous characterization but no absolute quantification was performed, as a fluorescence standard was not measured in the same geometry.

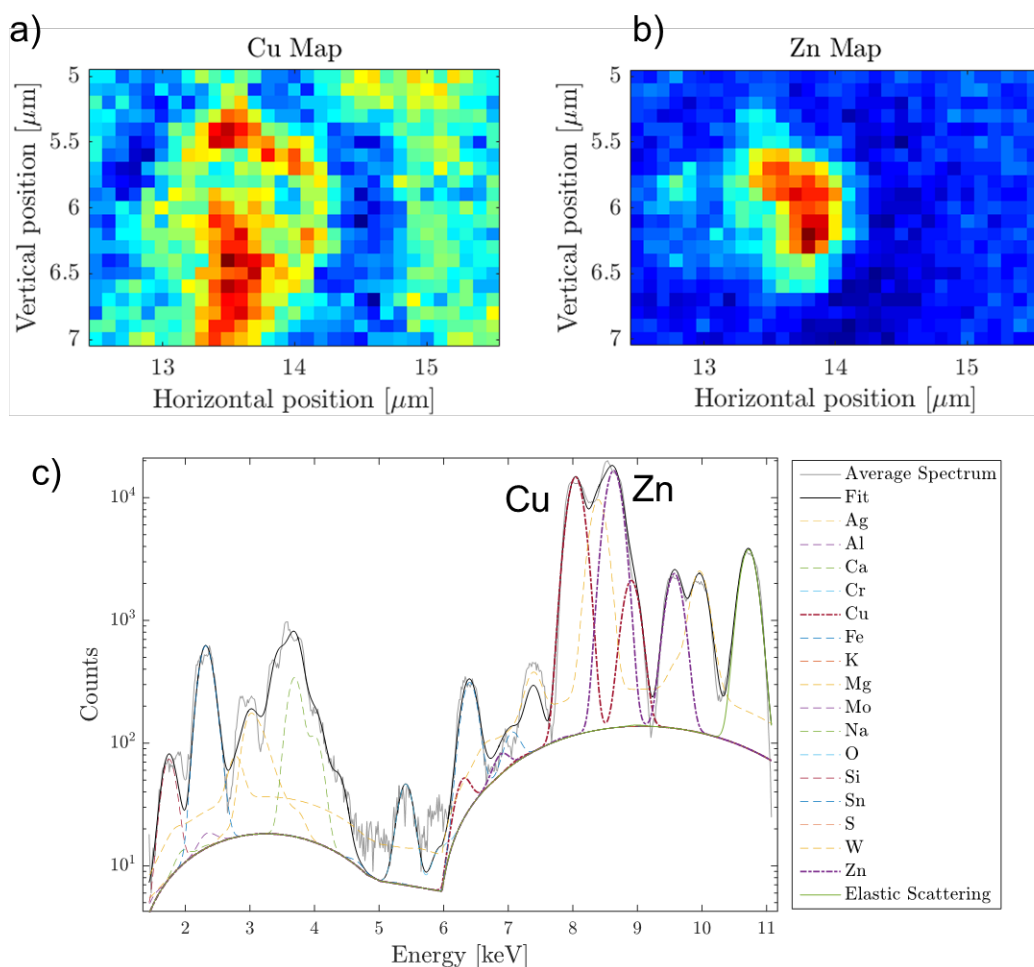


**Figure 3-10. Cu map (a) and Zn map (b) of PLD kesterite. Pixel size is 100 nm. Fluorescence spectrum of counts on all pixels (c).**

### 3.2.2 Ptychographic Tomography of Kesterite from Oxides

For methods refer to section Methods of section 5.1. Data presented in this section was acquired during the same beamtime and according to the same modality, but only at the off-resonance energy of 6.2 keV. The other difference concerns sample preparation, as in this case the sample has been lifted out at an angle rather than orthogonally to the layers. The angle has been chosen to mitigate phase wrapping. As the Mo layer has a high  $\delta$ , the phase shift  $\Phi(\mathbf{r}) = 2\pi/\lambda \int \delta(\mathbf{r}, z) dz$  would exceed  $2\pi$  when integrated along the whole sample thickness (5  $\mu\text{m}$ ). If it is tilted the phase shift is spread along less scattering layers (e.g. soda lime glass), which allows a range of projection angles to be immune from phase wrapping ( $\Phi(\mathbf{r}) < 2\pi$ ). An angle of 38 degrees was chosen to satisfy this condition.

### 3.2.3 Kesterite Solar Cells from Sulfurized Oxides

We present this data highlighting an important detail relative to CdS, confirming evidence from the main investigation in chapter 5. The grains of CZTS in this sample are sparse, unlike the compact bulk of the other samples. The reason has been attributed to formation of a gaseous phase during annealing, which prevents aggregation of individual grains. This feature has been observed with SEM on another region of the device. Because of the sparsity of the grains, CdS leaks all around them. That can be observed in the slices of **Figure 3-11**, where the slightly darker contours around each grain in the electron density images, which appear brighter in the absorption image, are due to CdS. The expected electron density is slightly higher than CZTS, but here it presents a ca. 10% porosity which has been already been reported in literature (cf. chapter 5).

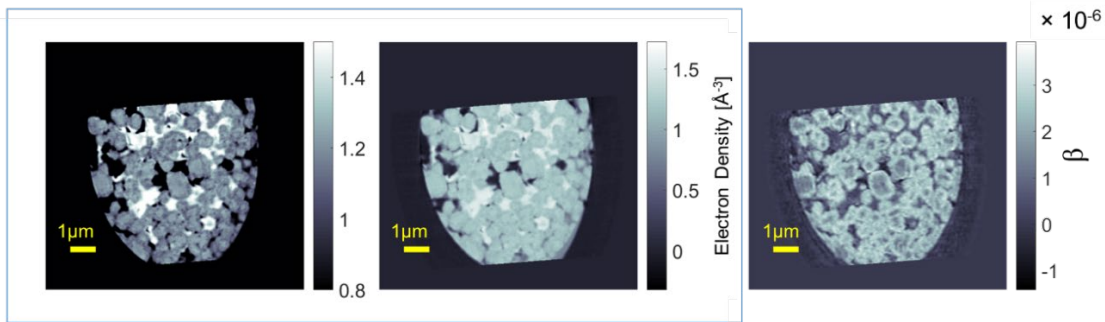


**Figure 3-11. Axial slice of kesterite device from oxide-precursors. Electron density in different scales (left, middle) from phase tomogram, and beta from absorption tomogram (right). Grains of kesterite are shown in this picture.**

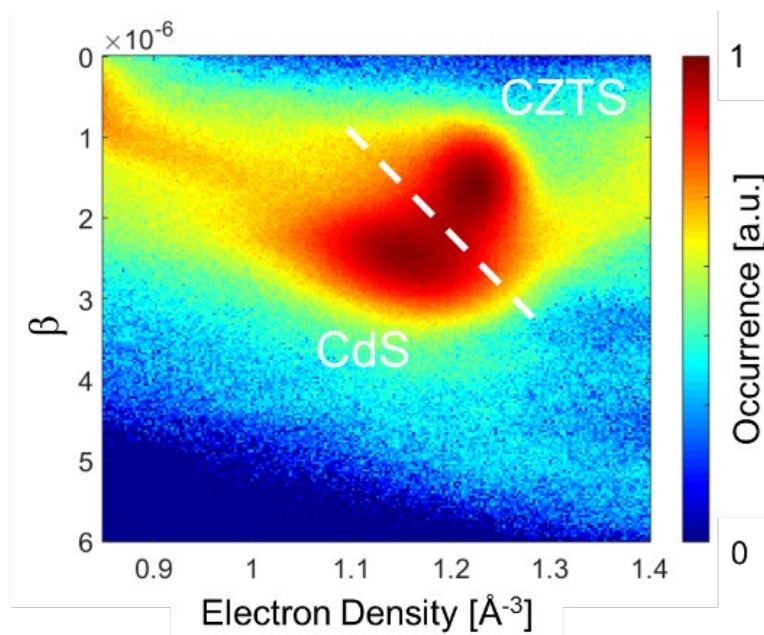


**Figure 3-12. Bivariate histogram for electron density and  $\beta$  for sample from oxide-precursors. Two clusters can be localized in the plot, one with lower electron density but with higher absorption compared to the other.**

In the bivariate histogram of the volumes of **Figure 3-12**, it is possible to estimate the measured electron density and absorption by localizing the centroids of the two clusters. These values match closely their expectations (see **Table 3-1**), corroborate the CdS porosity, highlighting that CdS cannot be mistaken by other layers because of its high absorption.

**Table 3-1. Expected values for electron density and beta of three layers of interest.**

Layer	Electron Density [ $\text{\AA}^{-3}$ ]	$\beta$ [ $1 \times 10^{-6}$ ]
CZTS	1.26	1.63
CdS	1.29	2.90
ZnO	1.57	0.85

Once again the histograms of measured electron density and absorption (**Figure 3-13**) highlight the low quantitiveness of the absorption tomograms alone. We report them for this sample because of the higher amount of CdS.

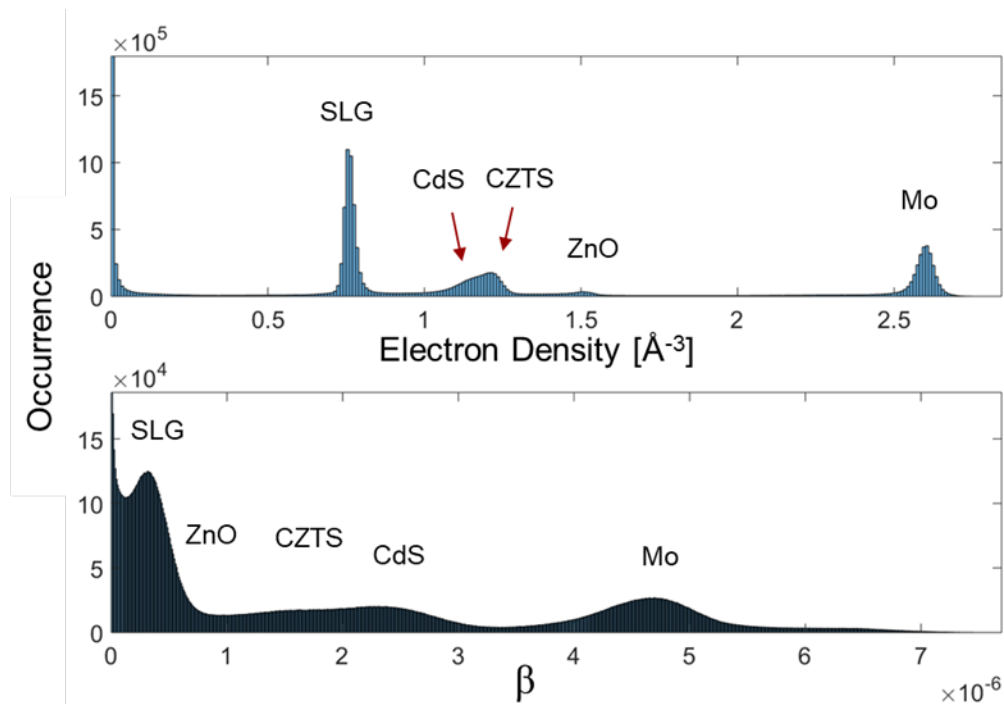


**Figure 3-13. Histogram of electron density (top) and  $\beta$  (bottom) measurements within the volume. The labels of the single layers point to their approximate range of values.**

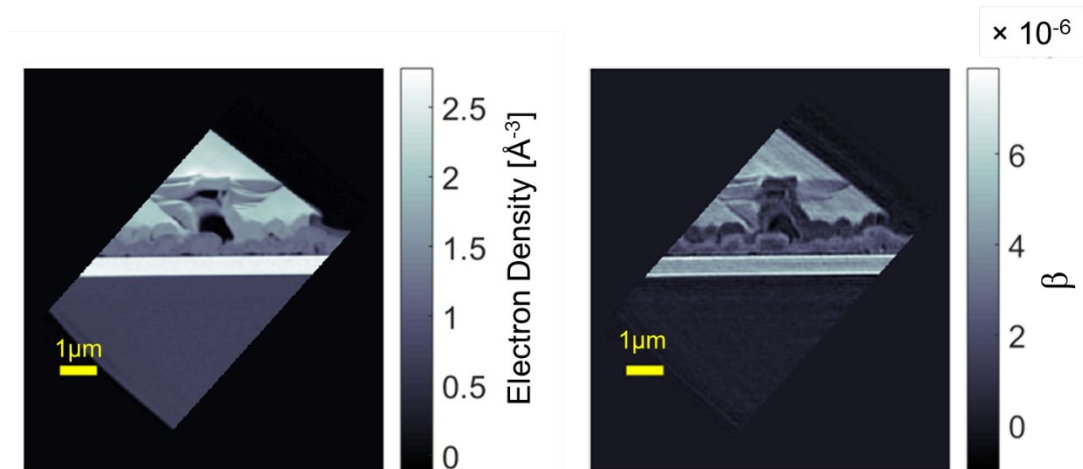


**Figure 3-14. Sagittal slice of sample with CZTS from Oxides. Electron density (left) and  $\beta$  (right).**

**Figure 3-14** shows a sagittal view of the sample and highlights an important aspect related to sample preparation. It can be observed in all sagittal slices of the samples displayed in chapter 5 that the Mo layer, which is highly scattering, appears narrower than the actual diameter of the cylinder. However, that is an expected and well-known reconstruction artefact. In those samples the Mo layer is not the main subject of our analysis and that does not affect our conclusions. However, in previously acquired data of OSC and with a different reconstruction code, a layer of interest was on top of a highly scattering layer. The reconstruction was problematic because of several phase-wrapping artefacts at the interface. That motivated a tilted geometry for sample preparation, in which the sample is lifted out of the device not in the direction of the normal to the device planes, but at an angle of 38 degrees. These result validate this sample preparation strategy as a way to prevent reconstruction artefacts due to highly scattering material.

## 4. Monte Carlo Ray Tracing Simulations of Coherent Diffractive Imaging

This paper reports an alternative simulation framework entirely based on ray tracing. In the overall project, it is meant as an aid for testing of phase retrieval algorithms, and as a more comprehensive simulation tools for experiments, as ray tracing programs are used to simulate entire beamlines and experiments.

It is an aid for testing, because it prevents the inverse crime. An inverse problem is one that solves for the unknown  $X$ , with the model  $A$ , and the measured data  $B$ :

$$AX = B \tag{4.1}$$

An algorithm to find  $X$ , will rely on  $A$  as a model, and will need a synthetic  $B$  to be tested. The inverse crime is committed when the synthetic data is produced with the same model, used for inversion, i.e. 4.1. As the paper will clarify, the model used for ptychography and the ray tracing model are substantially different, although, as we show, they give similar results. Therefore synthetic data can be produced with ray tracing and used to test phase retrieval, avoiding the inverse crime. As to the more comprehensive simulation, a ray tracing simulation allows multiple components to be placed in a scheme reproducing the actual beamline, and can potentially simulate vectorial wavefields and rays coming from parasitic scattering.

The ray tracing scheme was tested by comparing back-propagation and phase retrieval. Here we clarify that our choice of using two different images for amplitude and phase is a more difficult case than a real experiment. For a real sample, amplitude and phase of its transmission function have the same structure. However, simulations in literature use our same approach to show whether a mixing of amplitude and phase appears in the retrieval, which would not be observable with a real sample.

The work presented here stops at the simulation of a toy problem. We hope that the next PhD student will take over the task of demonstrating useful practical cases, such as the organic solar cells.

## 4.1 Journal article 1



## A Monte Carlo ray-tracing simulation of coherent X-ray diffractive imaging

Fevola, Giovanni; Bergbäck Knudsen, Erik; Ramos, Tiago; Carbone, Dina; Andreasen, Jens Wenzel

*Published in:*  
Journal of Synchrotron Radiation

*Link to article, DOI:*  
[10.1107/s1600577519014425](https://doi.org/10.1107/s1600577519014425)

*Publication date:*  
2020

*Document Version*  
Publisher's PDF, also known as Version of record

[Link back to DTU Orbit](#)

*Citation (APA):*  
Fevola, G., Bergbäck Knudsen, E., Ramos, T., Carbone, D., & Andreasen, J. W. (2020). A Monte Carlo ray-tracing simulation of coherent X-ray diffractive imaging. *Journal of Synchrotron Radiation*, 27(1), 134-145. <https://doi.org/10.1107/s1600577519014425>

---

### General rights

Copyright and moral rights for the publications made accessible in the public portal are retained by the authors and/or other copyright owners and it is a condition of accessing publications that users recognise and abide by the legal requirements associated with these rights.

- Users may download and print one copy of any publication from the public portal for the purpose of private study or research.
- You may not further distribute the material or use it for any profit-making activity or commercial gain
- You may freely distribute the URL identifying the publication in the public portal

If you believe that this document breaches copyright please contact us providing details, and we will remove access to the work immediately and investigate your claim.



# A Monte Carlo ray-tracing simulation of coherent X-ray diffractive imaging

Giovanni Fevola,<sup>a</sup> Erik Bergbäck Knudsen,<sup>b</sup> Tiago Ramos,<sup>a</sup> Dina Carbone<sup>c</sup> and Jens Wenzel Andreassen<sup>a\*</sup>

<sup>a</sup>Department of Energy Conversion and Storage, Technical University of Denmark, Frederiksborgvej 399, Roskilde 4000, Denmark, <sup>b</sup>Department of Physics, Technical University of Denmark, Fysikvej 311, Kgs Lyngby 2800, Denmark, and <sup>c</sup>MAX IV Laboratory, Lund University, 22484 Lund, Sweden. \*Correspondence e-mail: jewa@dtu.dk

Received 21 May 2019

Accepted 22 October 2019

Edited by V. Favre-Nicolin, CEA and Université Joseph Fourier, France

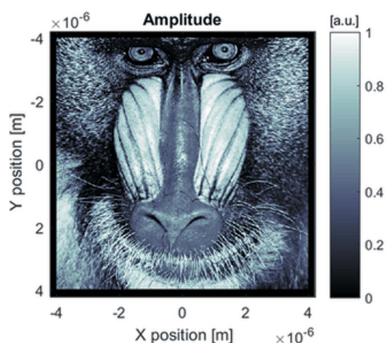
**Keywords:** X-ray microscopy; Monte Carlo simulations; ray tracing; coherent diffractive imaging; ptychography.

**Supporting information:** this article has supporting information at journals.iucr.org/s

Coherent diffractive imaging (CDI) experiments are adequately simulated assuming the thin sample approximation and using a Fresnel or Fraunhofer wavefront propagator to obtain the diffraction pattern. Although this method is used in wave-based or hybrid X-ray simulators, here the applicability and effectiveness of an alternative approach that is based solely on ray tracing of Huygens wavelets are investigated. It is shown that diffraction fringes of a grating-like source are accurately predicted and that diffraction patterns of a ptychography dataset from an experiment with realistic parameters can be sampled well enough to be retrieved by a standard phase-retrieval algorithm. Potentials and limits of this approach are highlighted. It is suggested that it could be applied to study imperfect or non-standard CDI configurations lacking a satisfactory theoretical formulation. The considerable computational effort required by this method is justified by the great flexibility provided for easy simulation of a large-parameter space.

## 1. Introduction

Coherent diffractive imaging (CDI) techniques have become increasingly popular in the X-ray community over the last two decades, to the point that most synchrotrons have at least one beamline dedicated to them (Miao *et al.*, 2015). CDI techniques are based on the inversion of coherent X-ray intensity data to obtain an image of the diffracting sample. This inversion is performed through algorithms that utilize boundary conditions in both real and reciprocal space, *e.g.* sample size and measured data, respectively, for the recovery of amplitude and phase of the sample-diffracted field (Veen & Pfeiffer, 2004). Thus, the recovered images are obtained without the use of lenses (Chapman & Nugent, 2010), which represents the most appealing feature of CDI, implying that the theoretical limit for the image resolution is determined only by the extent of reciprocal space that can be recorded with statistical significance (Noh *et al.*, 2016). The actual resolution, however, is affected by other factors related both to the physics of the experiment and to the processing of the collected data. Non-ideal conditions, such as partial coherence, mechanical instabilities and electronic noise, all contribute to the degradation of resolution by decreasing data quality. Although these can be accounted for in the reconstruction algorithms, and several strategies to mitigate their detrimental effects have been proposed in the literature (Thibault & Guizar-Sicairos, 2012; Godard *et al.*, 2012; Chang *et al.*, 2019), they still represent a strong limitation for the ultimate achievable resolution. This is demonstrated by the fact that, although remarkable for a non-destructive technique, the current



record resolutions for tomographic reconstructions based on full-field CDI [ $\sim 10$  nm (Takahashi *et al.*, 2010)] or ptychographic projections [14.6 nm (Holler *et al.*, 2017), 13.6 nm (Ramos *et al.*, 2017)] are probably an order of magnitude higher than the theoretical limit (Marchesini *et al.*, 2003; Dietze & Shpyrko, 2015), at least for inorganic materials (Howells *et al.*, 2009).

Due to the limited availability of coherent X-ray sources, it becomes of primary importance to be able to perform an offline optimisation of the experiment, prepare the data acquisition and predict the quality of its outcome. Therefore, reliable tools for the simulation of CDI experiments become an essential ingredient for the success of the experiment. The ability to reproduce data acquired under realistic conditions is essential to test and optimize retrieval algorithms and, furthermore, it helps to identify factors that could potentially limit the resolution and enables exploration of novel experimental configurations.

In the case of CDI, an inverse problem needs to be solved to retrieve the phase of the wavefield measured only through its intensities. What defines this inverse problem is the model that relates the object to the measurement: this model describes the interaction of X-rays with the sample and the propagation of the produced ‘exit’ wavefield to the detector, both of which depend on the chosen technique, *e.g.* measurement geometry, detector distance and X-ray wavelength. A typical example of such interaction is the attenuation and phase delay experienced by the X-ray beam when transmitted through a sample in the so-called forward scattering geometry. In this case, the propagation is well described by the Fresnel or the Fraunhofer propagator depending on whether the patterns are collected in the near- or far-field regime, respectively. These models can be used to simulate an experiment, and noise can be added to the simulated data by scaling the wavefields according to the expected flux and extracting values for shot noise from a Poisson distribution. Electronic noise can be added as well using, for example, a model of Gaussian distribution.

However, the described approach uses, for the inversion of data, the same model used to produce them [inverse crime (Colton & Kress, 1992)]; moreover, all noise is based on models and great care has to be taken to ensure that it is propagated correctly, however accurate they might be. Finally, other physical variables that might affect the experimental results, such as optical aberrations or the presence of other optical elements on the beam path, *e.g.* pinholes or beam-defining slits (Mastropietro *et al.*, 2011), are difficult to account for unless a specific and accurate model can be created to describe analytically their impact, which can in itself be a relatively complex task. We introduce here an alternative geometrical means for the simulation of coherent X-ray diffraction data, entirely based on ray tracing. This very general framework offers the possibility to customize the model of sample interaction (each intercepted element of the sample can modify any parameter of the ray), to include elements of the setup that affect data quality (optical elements, slits, pinholes, windows) and, for diffraction, relies on a very general and simple propagator based on Huygens

wavelets. This approach has the double advantage of producing diffraction data that are *intrinsically* noisy due to the Monte Carlo method used, and totally *independent* of the forward model on which reconstruction algorithms might rely, ensuring prevention of the inverse crime. The scheme for diffraction is not radically different from the already reported scheme for diffraction in *McXtrace* (Bergbäck Knudsen *et al.*, 2013), but it contains an important modification which is detailed in the following and, importantly, is applied for comparison to a realistic test case for which solutions from other approaches are available.

With respect to other tools available in the existing X-ray diffraction simulation software portfolio, our approach provides purely ray-tracing-based simulations for fully coherent X-ray diffraction experiments, which are still absent in the existing literature. While some notable tools such as *ShadowOUI* (Rebuffi & Sánchez del Río, 2016) and *OASYS* (Sanchez del Rio & Rebuffi, 2019) rely on hybrid models using both approaches, available software tools are mainly divided into those based on wave-propagation methods [*e.g.* *XRT* (Klementiev & Chernikov, 2014), *SRW* (Chubar *et al.*, 2013), *PHASE/REDUCE* (Bahrtdt, 2007)] and those based on ray tracing [*e.g.* *SHADOW* (Lai & Cerrina, 1986), *RAY* (Schäfers, 2008)]. The former exploit the laws of physical optics and Fourier integrals whereas the latter exploit the laws of geometrical optics. *McXtrace* (Bergbäck Knudsen *et al.*, 2013) falls into this second category and is, furthermore, Monte Carlo based. The ray-tracing approach might not appear the most suitable to describe diffraction, which is typically viewed as an undulatory phenomenon and is qualitatively explained by Huygens’ principle. On the other hand, when complemented with a Monte Carlo based approach, ray tracing provides all degrees of freedom when it comes to the difficult task of describing non-ideal conditions from first principles. For instance, partial coherence, extremely relevant for our study, has been suitably addressed in this context (Prodi *et al.*, 2011; Cipiccia *et al.*, 2014), and beam monochromaticity, divergence and polarization effects are particularly easy to simulate. Furthermore, this method does not rely on paraxial approximation and can be particularly effective for simulation of CDI datasets that extend far in the reciprocal space (Shapiro *et al.*, 2014). This will be relevant for experiments carried out with high flux in the soft X-ray regime that aim at extreme resolutions as will certainly be the case at the new diffraction-limited sources (Hettel, 2014).

Outside of the X-ray context, the use of a geometrical approach for simulating diffraction dates back to the work of Young & Keller (see Kumar & Ranganath, 1991) and ray-tracing simulation of diffraction is widely explored: Mahan *et al.* (2018) established the conditions under which a Fresnel–Huygens principle is well described; Andreas *et al.* (2015) reported a vectorial ray tracer applied to laser interferometry in non-paraxial cases; Mout *et al.* (2016, 2018) have described the theory that makes Monte Carlo ray-tracing consistent, demonstrating diffraction of a multiple-component microscope in this framework. These works bear strong similarities with the ray-tracing scheme we have used here to simulate

CDI, which will be described. In this manuscript, we demonstrate the efficacy of our approach by focusing on a couple of simple cases of CDI measured in forward geometry and under far-field conditions. For demonstrative purposes, we choose examples that can be solved with existing approaches for comparison. Our approach, however, can be extended to other more complex cases where other methods fail and its impact is potentially the highest. These include simulation of novel approaches such as near-field CDI, grazing-incidence ptychography, or where the use of standard inversion algorithms fails to converge. This is the case of CDI under the Bragg condition and in the presence of strongly distorted phase fields. In this case the knowledge obtained from the simulations could help to reduce the space of possible solutions with a hybrid approach of inversion and fitting procedures (Mastropietro *et al.*, 2013). Other cases include the simulation of wavefronts from imperfect optics, where it would be useful to disentangle contributions from sample and wavefield. Simulations from low-contrast samples would help to identify the minimum dose necessary for inversion of data, and to optimize beforehand the setup of the experiments.

## 2. Methods – ray tracing of CDI

We focus on the simulation of CDI measured under far-field conditions. The implementation of a proper simulation, in this case, is achieved by ensuring that the two main requirements for CDI are satisfied. The first proviso of CDI is the thin sample assumption (Rodenburg, 2008), which allows the sample to be described with a 2D object function [the conditions for meeting this assumption are discussed by Dierolf *et al.* (2010)]. That withstanding, the multiplication approximation also holds, *i.e.*  $\psi$  (the wavefield immediately after the sample) can be expressed as the product of  $P$ , the wavefield immediately before the sample (also referred to as the probe), and  $O$ , the object function. Namely,

$$\psi(x, y) = P(x, y) O(x, y), \quad (1)$$

where  $(x, y)$  indicates the position vector in the sample plane. The second condition is that the intensity measured in the Fraunhofer, or far-field, regime, has a Fourier transform relation with the wavefield  $\psi$ , *i.e.* the intensity  $I$  in the far field should respect the following relation,

$$I(X, Y) = |\Psi(X, Y)|^2 = |\mathcal{F}[P(x, y) O(x, y)]|^2, \quad (2)$$

where  $\mathcal{F}$  denotes the Fourier transform and  $(X, Y)$  is the position vector in the detector plane. In the following, we discuss how the multiplication approximation and the transformation into the far field were implemented and tested in *McXtrace*. Before entering into the details, we need to recall some key concepts regarding ray tracing, *i.e.* the Monte Carlo approach and the computational flow. Further details can be found in the work by Bergbäck Knudsen *et al.* (2013). In *McXtrace*, a ray is described by 12 variables, including its position  $(x, y, z)$ , propagation vector  $\mathbf{k} = (k_x, k_y, k_z)$ , weight  $p$  and phase  $\phi$ . It can conceptually be viewed as an ensemble of photons sharing the same position in space, the same propa-

gation vector and the same phase. The weight of a ray accounts for the number of photons that it represents. We neglect the remaining four variables for a ray, which relate to time and polarization, as they are not relevant for our discussion. Polarization has little effect for small scattering angles of the beam in both the horizontal and vertical directions. The time accounts for the longitudinal coherence, which in the thin object approximation is not relevant. Synthetically, we can write a set of rays as

$$r_i = (x, y, z, k_x, k_y, k_z, p, \phi), \quad i = 1, \dots, N, \quad (3)$$

where  $N$  defines the size of such set and is an input parameter. We define the ‘trace’ as the set of values that a ray assumes at all possible abscissae. If  $z$  is defined as the propagation direction, we define the trace  $T_i$  of the  $i$ th ray as

$$T_i = \{(x, y, z, k_x, k_y, k_z, p, \phi), \quad z_0 \leq z \leq z_{\text{end}}\}, \quad (4)$$

where  $z_0$  and  $z_{\text{end}}$  denote the boundaries of the region of interest. In this description, each component of an X-ray instrument can be introduced sequentially by placing it at specific positions ( $z_c$ ) along the beam path, with its own customizable parameters, effectively translating any (relevant) element of a beamline into software code. Formally, the instrument defines a rule  $BL$  to compute the trace of a ray,

$$BL: r_i \rightarrow T_i, \quad i = 1, \dots, N. \quad (5)$$

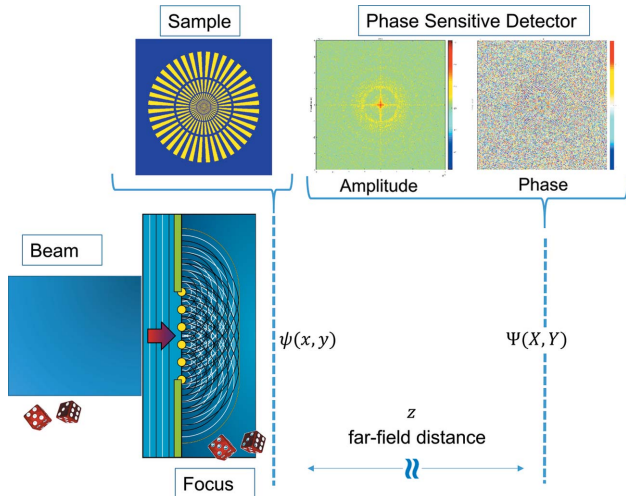
$BL$  describes the interaction of every specific component with the ray, and how it affects the propagation of the rays as well as of propagation in free space. A trace is updated as a result of simple propagation in space or as a result of a particular interaction with a component. As with all Monte Carlo methods, a single trace does not provide relevant information per se, but cumulative statistics of all traces do. In *McXtrace* the computational flow of a simulation is, in general, sequential and static, *i.e.* a pre-defined number of independent traces are computed in a sequential way. In some limited cases, the sequence may be purposely broken at discrete logical points in the simulation, but we have no need for this feature in our discussion.

Fig. 1 illustrates the components of a setup for a CDI measurement with a focused X-ray beam. The simulation of this measurement with *McXtrace* follows the path of the rays through the four components. For each ray the following operations are performed in order:

(i) A ray is instanced by the source according to constraints input by the user. For a source satisfying ideal plane wave conditions, all rays have identical  $\mathbf{k}$ -vectors (monochromatic and parallel beam), phases and weights.

(ii) The ray interacts with the focusing optics via diffraction: effectively it takes a new direction, mimicking a Huygens’ wavelet (this step is described in detail later).

(iii) The ray interacts with the sample: after being propagated from the exit of the focusing optics to the sample section, the exit ray is computed according to equation (1). If, instead of its transfer function, the sample is specified in terms of refractive indices, the amplitude and phase of the object function are computed using  $\exp(-k\beta\tau)$  and  $\exp(jk\delta\tau)$ , in



**Figure 1** Illustration of a general setup for simulation of CDI in *McXtrace*. The beam, focus, sample and detector are components in the graphical user interface, each consisting of a set of lines of code modifying parameters of the rays in the simulation. The dice illustrate components where a Monte Carlo process takes place. We refer to  $\psi$  as the wavefield immediately after the sample, and to  $\Psi$  as the wavefield on the detector.

which  $k$  and  $\tau$  indicate the wavenumber and the thickness of the sample, respectively, and  $\delta$  and  $\beta$  are the real and imaginary parts of the refractive index ( $j$  denotes the imaginary unit).

(iv) The ray is propagated to a numerical detector, referred to in the following as Phase Sensitive Detector (*PSD*), where it keeps its phase information and is accumulated coherently on the target pixel. Namely,

$$PSD_{\phi}(m, n) = \sum_{i \in T_{m,n}} c_i p_i \exp(j\phi_i), \quad (6)$$

where  $T_{m,n}$  is the subset of traces hitting a pixel with indices  $m, n$ . Rays with a weight  $p$  and phase  $\phi$  accumulate, with a scale factor  $c$ , over the coherent sum  $PSD_{\phi}$ ;  $c$  is dependent on the distance between the pixel and ray origin. Interference among rays is produced at this step.

Operations (ii) and (iv) deserve more space for an accurate description because they contain the core model of diffraction that we use to simulate a realistic coherent X-ray experiment properly. For simplicity, in the following we consider that the sample in step (iii) does not induce any further modification to the rays, *i.e.* it is  $O(x, y) = 1$  in equation (1). In conventional ‘incoherent’ ray-tracing simulations, rays travel in a straight line and constructive interference between different rays is not accounted for, *i.e.* all rays hitting the area of the detector pixel are summed incoherently. Here, instead we are interested in adding rays coherently to predict the correct interference diffraction pattern. The diffraction of the rays in our model is described by Huygens’ principle, which phenomenologically explains diffraction by modelling a plane wave as a sum of elemental spherical waves. Although it is possible to split one ray into many and rely on the law of large numbers and Monte Carlo sampling to generate the wavefront on a semicircle, in practice the procedure is impractical due to the number of

rays required for sufficient sampling of the wavefront. Instead, we have developed an approach that considers diffraction from the detector perspective, in which all detector pixels collect diffraction from every ray. Furthermore, diffraction is collected only on a sub-pixel level. This may be done efficiently as it amounts to locally substituting a ray with an associated spherical wavefront, and sampling that wavefront at the sites of detector sub-pixels. An additional upshot of this reverse procedure is that it inherently avoids sampling points outside the detector.

Besides computational efficiency, the need to define an appropriate sub-pixel size stems from the following argument. Let  $\Psi(X, Y)$  be the wavefield in the detector plane. Then the recorded value  $PSD_{\phi}$  on the pixel with indices  $(m, n)$  can be written as

$$PSD_{\phi}(m, n) = \iint_{-\infty}^{+\infty} \Psi(X, Y) \Lambda_W(mW - X, nW - Y) dX dY \\ = (\Psi \star \Lambda_W)(mW, nW), \quad (7)$$

where  $\star$  denotes the convolution operator,  $(X, Y)$  are the coordinates in the detector plane and  $\Lambda_W$  is the 2D top-hat function of size  $W$ ,

$$\Lambda_W(X, Y) = \begin{cases} 1, & \text{if } |XY| < 1, \\ 0, & \text{otherwise.} \end{cases} \quad (8)$$

Equation (7) states that the matrix of the recorded values is given by the convolution of the actual wavefield function with the pixel area, which causes an effective blurring of the wavefield at the detector plane that strongly depends on the value of  $W$  (see the example in Section S1 of the supporting information). One way to prevent blurring is to impose  $W \ll a$ , where  $a$  is the smallest feature in the object or illumination. In this way, the top-hat function can be approximated by a Dirac delta and its effect in the convolution becomes negligible. Another option to circumvent this problem is to translate all rays hitting a pixel to its centre ( $W = 0$ ). This is followed in the work by Mout *et al.* (2018), and has also been tested by us, yielding the same results. We emphasize that this requirement, and the way it is addressed in both cases, only relates to the way interference is evaluated in a ray-tracing context and should not be confused with the Nyquist sampling requirement of CDI.

Concerning the propagation mentioned in step (iv), we point out that no paraxial approximation is made. Instead, the distance between wavelet origin and detector pixel is determined on a pixel-by-pixel and ray-by-ray basis, and thus the exact distance is taken into account. The factor  $c_i$  in equation (6) scales the weight accordingly, *i.e.*  $c_i \propto 1/r$ , where  $r$  is the distance between the ray origin and (sub)pixel. This term can be held constant in the far-field approximation and set to  $1/z$  for each ray, whereas it must be evaluated for each ray in the near-field. However, this is carried out at no extra cost in a ray-tracing context as the distances ( $r$ ) are computed regardless.



### 3. Results and discussion

We describe three study cases we have examined to show the correctness and the applicability of our approach: diffraction from a grating, full-field CDI from a complex object illuminated by a uniform beam with flat wavefront, and ptychography of a complex object with an experimental probe function (unpublished data). For all examples, the wavelength  $\lambda$  and the sub-pixel size  $W$  are set to 1 Å and the sample-to-detector distance  $z$  is set to 5 m. The diffraction patterns, when noted, are reported on a logarithmic scale, whereas they are always normalized with respect to the number of simulated rays  $N$  to allow a comparison. Details of the analysis of the more basic case of diffraction from a single slit are reported in Appendix A and Appendix B.

#### 3.1. Grating-like source

As a first test, we show the simulation of a  $5 \times 5$  grating in Fig. 2. The grating consists of a square grid of square apertures of size  $w = 1$  nm separated by a distance  $d = 1$  μm. Each aperture is an elementary source where a ray is emitted from a randomly chosen position within the region defined by the

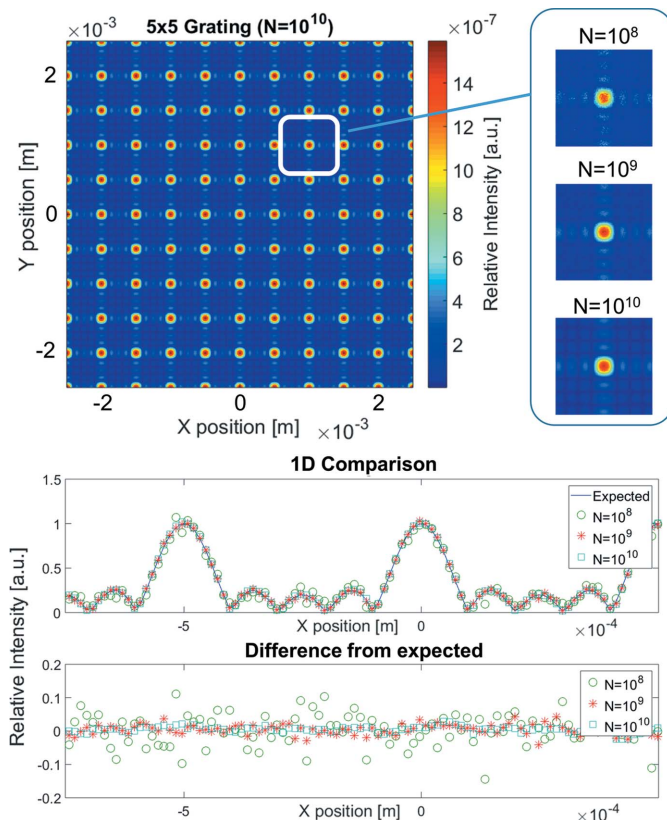


**Figure 2** Simulated diffraction of a  $5 \times 5$  grating. The distance between the apertures is 1 μm, and an  $800 \times 800$  pixel detector of 0.5 cm size is used. Intensities are on a linear scale, and the ray weight is normalized to  $N$ , thus allowing the comparison for simulations with varying  $N$ . The three cases  $N = 10^8$ ,  $10^9$  and  $10^{10}$  are considered for comparison in the inset and the 1D plot. The diffraction patterns show slight blur and non-zero background for the first case, whereas they become clear in the others. The profile comparison (bottom plot) shows in detail the fluctuations for the three cases.

aperture. The simulated diffraction pattern of the grating presents all the characteristics predicted by theory. Namely:  $n - 2$  subsidiary maxima between two main peaks can be observed when the illumination function is a grid of  $n \times n$  apertures; the distance  $y$  between the main peaks is related to the distance between the apertures  $d$  by the following equation,

$$d \sin \theta = d \frac{y}{z} = l \lambda, \quad (9)$$

in which  $l$  is an integer and  $z$  is the sample-to-detector distance; the envelope observable in the diffraction pattern depends on the size of the apertures and follows the expected trend of

$$\text{sinc}\left(\frac{w}{z\lambda} X\right) \text{sinc}\left(\frac{w}{z\lambda} Y\right), \quad (10)$$

where  $w$  is the size of the aperture and  $X, Y$  are coordinates in the detector plane. In particular, we show in Fig. 2 that, for a sufficiently high number of simulated rays ( $N = 10^{10}$  in this case), the simulated trend follows closely the one predicted by theory,

$$|\Psi(X, 0)| = \left| \Psi_0 \sin\left(\frac{N\pi d X}{\lambda z}\right) \sin\left(\frac{\pi d X}{\lambda z}\right) \right|. \quad (11)$$

The same results are obtained by using a Fourier transform as in equation (2) with  $P(r) = 1$ . This test is an extension of the basic diffraction experiments of single and double slits already reported by Bergbäck Knudsen *et al.* (2013). It demonstrates that interference of multiple point-like sources distributed on a grid placed at a given section is properly modelled and recorded with our approach and, therefore, represents a test-bench simulation. Moreover, it serves us to roughly estimate the number of rays needed for simulation of imaging cases, which we have learned is dependent on the density of rays at the source and at the detector. However, this is difficult to extend to more general cases. We find in this case that a choice of  $N = 10^8$  leads to poor cancellation of the zeros and fluctuations in the profile with standard deviation  $\sigma = 0.054$ , whereas  $N = 10^9$  already gives satisfactory results ( $\sigma = 0.035$ ), and  $N = 10^{10}$  can be regarded as an ideal noiseless case ( $\sigma = 0.033$ ). For an estimation of values and trend of the error as a function of  $N$ , see Appendix B, where we evaluate it in a simpler case.

This also allows us to assert that, despite the high number of phase evolutions, the machine numerical precision does not seem to interfere with the phasor accumulation, as we are eventually able to obtain accurate cancellations of zeros and no systematic errors on the profile. This we have tested and observed for several reasonable detector distances and sizes.

#### 3.2. Full-field CDI

In a full-field CDI (Miao *et al.*, 1999) experiment, the entire sample is illuminated by a coherent beam and the diffraction pattern is recorded in the Fraunhofer regime. As the information about the structure of the object is encoded in the phase and only intensity measurements are available, a phase

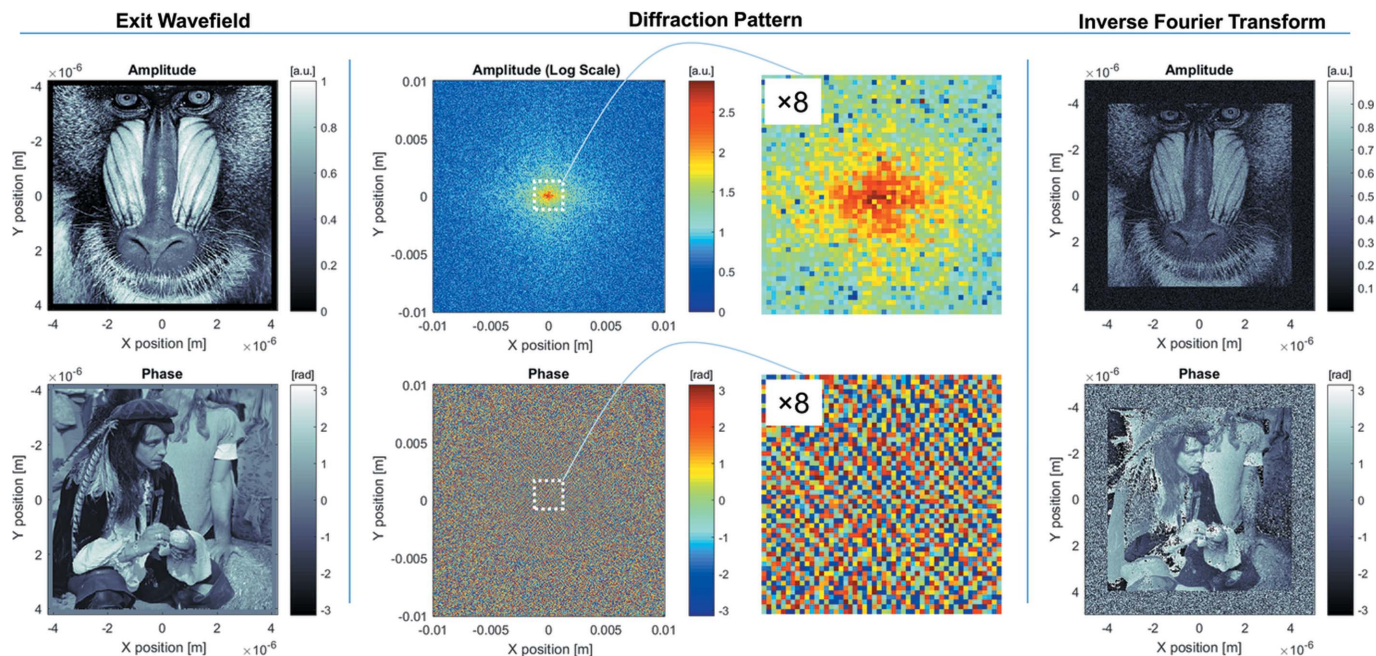


**Figure 3**

Full-field CDI. Columns, left to right: wavefield immediately after the object; far field, recorded on a 2 cm-size detector (second column) and zoom on the inner portion (third column); inverse Fourier transform of the diffraction pattern in column 2. Upper and lower figures display amplitude and phase of each recorded wavefield, respectively. Wavelength and sample-to-detector distances are 1 Å and 5 m, respectively. A uniform amplitude and constant phase have been selected for the illuminating beam to allow an immediate visual comparison of the results.

retrieval algorithm is required to recover the initial object. This algorithm exploits the setup configuration by imposing the support constraint, which provides the *a priori* knowledge that the object is limited in size and fully illuminated by the beam as well as the exact knowledge of the diffracted intensity data.

To illustrate the outcome of our tests we refer to Fig. 3. In this simulation, we assume the validity of the multiplicative assumption to verify the second requirement of CDI techniques — the correct propagation in the far-field zone. For this reason, we used a two-dimensional mask of complex refractive indices, with amplitude and phase mimicking popular test images (baboon and man) to demonstrate how the information of attenuation and phase shift of a thin sample is propagated by the simulator into reciprocal space. In this case, the setup is that of a full-field CDI experiment. The images are input with  $480 \times 480$  pixel square masks of  $8 \mu\text{m}$  lateral size; the object is fully covered by a slightly larger beam, with a uniform intensity profile and constant phase to allow for a direct visual comparison.<sup>1</sup> A  $400 \times 400$  pixel detector with 2 cm lateral size is set at a distance of 5 m from the sample. The object and detector sizes determine the sampling requirement for CDI (Spence *et al.*, 2004), which yields in this case  $\sim 30 \mu\text{m}$  as the minimum pixel size, lower than the  $50 \mu\text{m}$  pixel size of this detector. Therefore, this configuration produces the undersampled diffraction patterns represented

<sup>1</sup> The constant phase is not in general a requirement of a CDI experiment. Conceptually, it is not a useful addition to use a realistic probe in this case, as CDI phase retrieval algorithms do not typically retrieve the probe function (but only the wavefield  $\psi$ ) and because we are using a Fourier transform to invert the pattern.

in the second column of Fig. 3 (an example of an oversampled simulation follows below). Given the use of a constant phase beam, the validity of our simulation can be verified by simple inverse Fourier transform of the simulated patterns. The result, depicted in the last column of the same figure, with a reconstructed pixel size of 25 nm, proves that the information about the object has been properly encoded. The noise introduced by the Monte Carlo process produces a mixing of amplitude and phase of the retrieved object which can be observed for a lower number of traced rays.

Our simulation tool allows us to assess how the Monte Carlo approach affects the quality of the patterns. To illustrate this, we use a detector with a pixel size of  $10 \mu\text{m}$ , which is hence oversampling and small enough to resolve the speckles produced by the largest dimensions of the sample. The speckle size is expected to be  $62.5 \mu\text{m}$  in this case. In Fig. 4 we illustrate how speckle visibility is affected by the number of simulated rays. The higher the number of simulated rays the better the speckles are resolved, particularly the least intense ones farthest out in reciprocal space. The effect of enhanced speckle visibility with increasing  $N$  on a retrieved image is reported in Section S2.2 of the supporting information, together with an estimation of the noise.

### 3.3. Ptychography

In ptychography (Rodenburg & Faulkner, 2004; Pfeiffer, 2018), the sample is illuminated by the beam one portion at a time and the object size is not limited by the size of the beam. A scan pattern is defined to illuminate the object at different



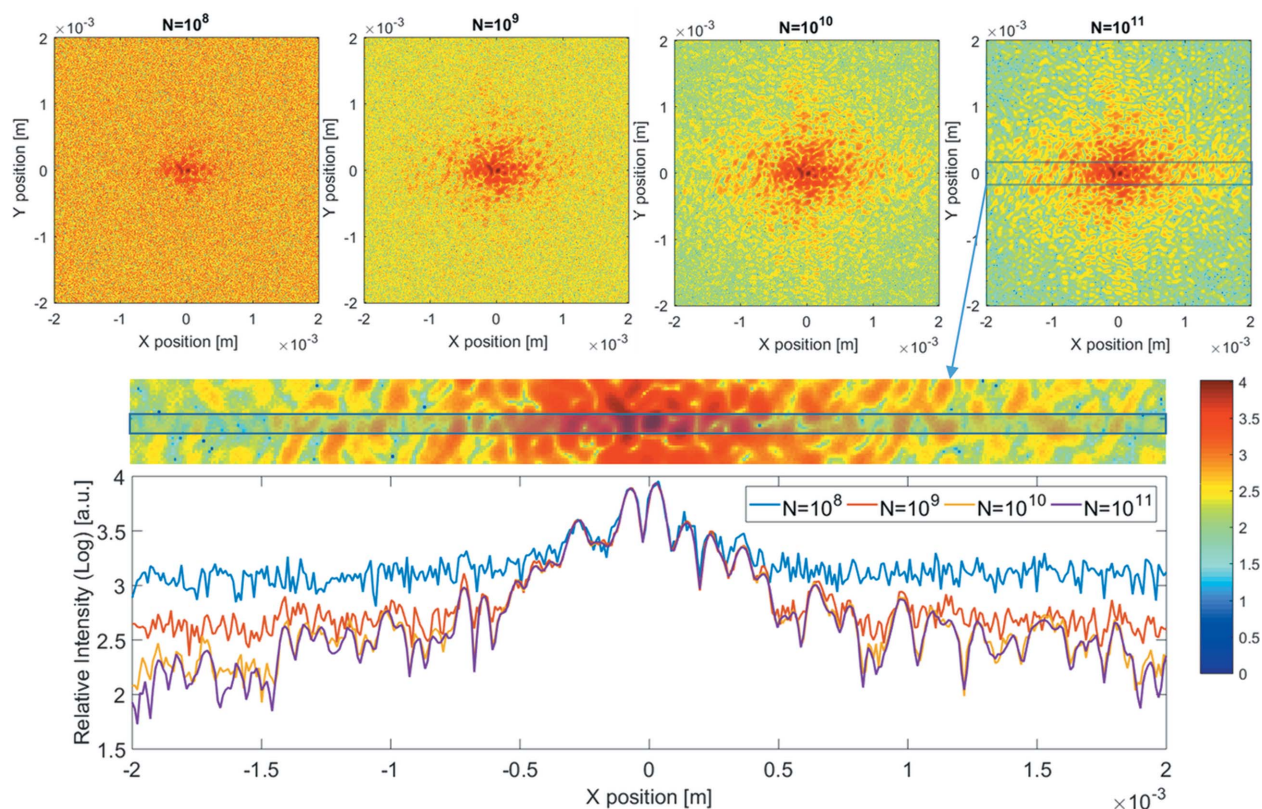


**Figure 4** Full-field CDI. Speckle resolution as a function of simulated rays. Three test cases are shown for a 4 mm-sized detector with 400 pixels set at a 5 m distance from the sample. All plots are on a logarithmic scale, with the same color bar. The profile is plotted along the  $X$  direction and is averaged on a length of seven pixels along the  $Y$  direction. Averaging helps to distinguish between speckles and fluctuations on a smaller scale due to noise. The speckles at higher spatial frequency are better resolved for increasing numbers of simulated rays  $N$ , whereas they are buried into background noise with fewer rays.

positions in overlapping areas and a set of diffraction patterns is collected. With respect to the definition of the setup, a sufficient amount of overlap between the illuminated portions of the sample must be ensured, and any symmetry of the scanning pattern that may cause raster-grid pathology (Thibault *et al.*, 2008) must be broken.

Here we discuss the implementation of our method for a ptychography scan applied to the same object of Fig. 3. In this case, we use the probe produced by Fresnel zone plate focusing optics and obtained with phase retrieval approaches from experimental data obtained in a previous experiment [Fig. 5(a)]. These data are used to describe the complex mask component that is inserted right before the sample in our instrument. The same probe could be produced by our simulation package by using a complete description of the focusing optics in Fig. 1. We prefer to use a real experimentally determined probe for our simulation. Some projections of the ptychography dataset generated in this test are reported in Fig. 5(c). The probe is shifted over the sample according to the Fermat spiral scheme depicted in Fig. 5(b), with steps sufficiently small to ensure 80% probe overlap [evaluated as in Huang *et al.* (2014)] and complete, uniform coverage (except for the corners). In this particular case, 160 steps are sufficient. We prefer the Fermat spiral scheme over a Cartesian grid or other geometries as it efficiently mitigates reconstruction artefacts. In this simulation, the specimen is  $\sim 3.1 \mu\text{m} \times 3.1 \mu\text{m}$

in size and its transfer function input is a  $480 \times 480$  matrix. A  $200 \times 200$  pixel detector of 3.5 cm lateral size [similar to Pilatus 100 K (Bech *et al.*, 2008)] is used. A total of  $10^{10}$  rays are used for each scan position. Each step runs for 12 min on a 16-core node. The phase and amplitude of the object are reconstructed via the inversion of the simulated diffraction patterns using cSAXS Matlab code. The result of the ptychography phase retrieval is shown in Fig. 6 and was obtained by running 300 iterations (with as many probe and object updates) of the algorithm ePIE (Maiden & Rodenburg, 2009). A good guess of the probe, its real part in our case, had to be provided to ensure convergence. The level of noise introduced by the simulation is acceptable for the pattern to return a fair reconstruction of the specimen and the probe (refer to Section S2 of the supporting information for a resolution assessment).

The reconstruction quality is comparable with that of the full-field case (see Section S2 of the supporting information for a resolution assessment). In this case, the single diffraction patterns are obtained with one-tenth of the rays used in Fig. 3. However, because of the multiple illuminations, a significantly larger total number of rays impinge on the sample. This results in estimates of the average signal-to-noise ratio being on the same order of magnitude (5.4 in CDI versus 3.3 in ptychography). We find that decreasing  $N$  by one order of magnitude in the ptychography case (*i.e.* going from  $10^{10}$  to  $10^9$ ) leads to

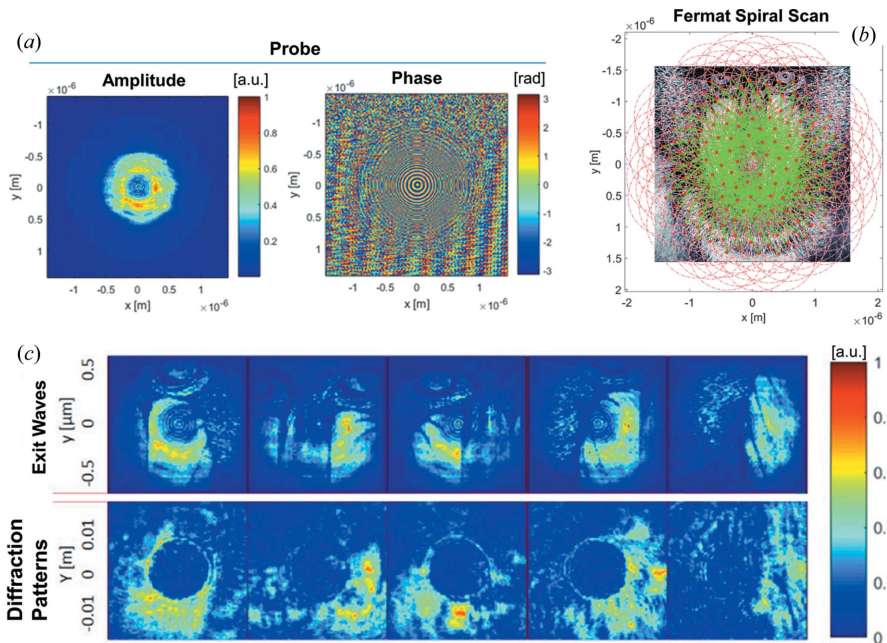


**Figure 5** Ptychography: (a) amplitude and phase of the probe used for illumination,  $500 \times 500$  pixels; (b) illumination scheme of Fermat spiral scan; (c) some results from the simulated ptychography dataset. The exit waves are in the top row, with each relative diffraction pattern below. The exit waves are recorded on a  $\sim 1 \mu\text{m}$ -wide detector covering most of the probe. Aside from high-frequency features, some near-field features are still visible in the diffraction patterns.

failure of the reconstruction, although the diffraction patterns do not suffer considerable loss in quality. As in Fig. 4, the difference between the cases  $10^{10}$  and  $10^{11}$  does not appear substantial, but can nonetheless mark the threshold for convergence in phase retrieval.

#### 4. Outlook

Relevant features of the method reported by Mout *et al.* (2018) can be applied to our implementation for further testing of more complex and unsolved cases. Specifically, the

vectorial expression for the accumulation of rays at each step allowing for a cascaded system indicates a viable path for the implementation of thick samples through cascaded objects. Given the similarity of our framework, we presume that this procedure is applicable to our case, at least with respect to the forward imaging mode. Concerning the general 3D case, we note that CDI techniques can already be simulated on a 3D object with the support of the *ASTRA* toolbox (van Aarle *et al.*, 2015). The line integration of the refractive indices represents a computationally expensive operation that could in principle be performed in *McXtrace*, but not as efficiently as in *ASTRA*. If the sample is thin enough, the internal scattering is negligible and it is recommended to use *ASTRA*, otherwise a 3D sample can be represented by a stack of masks along the ray direction, using a multi-slice approach as in the work by Maiden *et al.* (2012). Simulation of 3D volumes would allow a comparison with experimental data and would provide definitive evidence of the validity of this tool.

Another interesting case is the grazing incidence setup, where the theoretical analytical expression has proved significantly distant from actual measurement in some cases and seems only applicable to describe the height function of truncated crystals (Zhu *et al.*, 2015). Imperfect temporal coherence is also easily simulated by assigning different wavelengths to the rays. In particular, it is possible to assign to the rays energy values distributed on a Gaussian centered on the main energy, with a deviation. In principle, non-paraxial cases and near-field cases can be tested but have not been explored in this work for imaging (Appendix A reports a

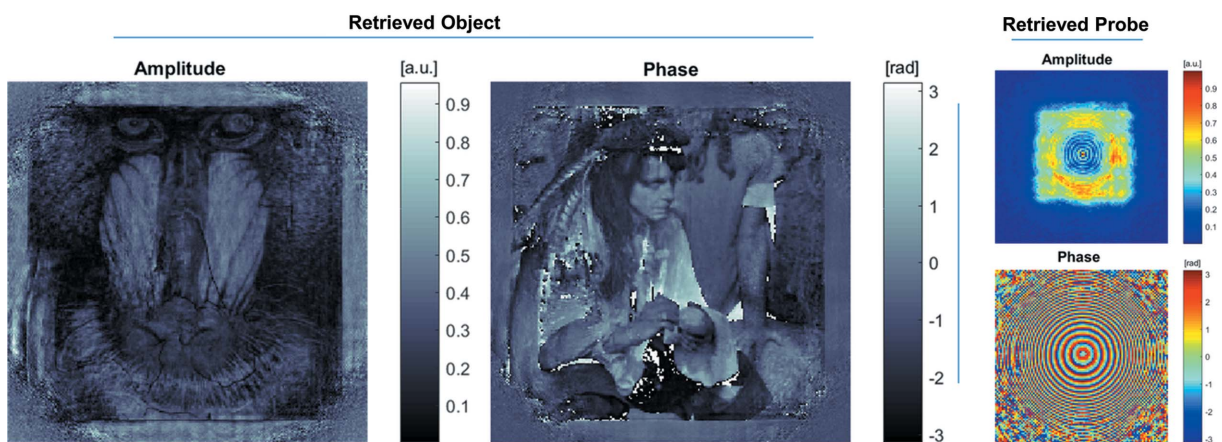


**Figure 6** Left to right: amplitude and phase of the retrieved object; plot of the retrieved probe, amplitude (top) and phase (bottom). The phase retrieval is performed with 300 iterations of ePIE after providing a good guess of the probe.



comparison with the Fraunhofer propagator in the case of wider angles with diffraction from a single slit). The model does not in fact assume paraxial propagation, and the spherical factor in the amplitude is accounted for each ray rather than set to the detector distance as in the far-field hypothesis.

Mout *et al.* (2018) also used a general expression for the weight of the rays, which could help to optimize the number of traced rays to achieve an adequate signal-to-noise ratio, reducing the computational cost of this method. We show in a basic example in Appendix B that not all portions of a detector are affected equally by Monte Carlo noise, which points to the study of specific, dynamical sampling strategies. The other main route to decrease computational cost is through parallelization. Formulated in this framework, any setup is easily parallelized, and GPU parallelized code can easily reduce processing time. Furthermore, the number of rays modern hardware can afford to simulate has increased exponentially over the years, making the cost of ray tracing for imaging within reach and with good prospects. While we routinely run simulations of billions of rays, the first *SHADOW* publication quotes 5000 as the maximum number of traceable rays, and as a result regards simulation of imaging experiments as ‘unsuitable’ (Lai & Cerrina, 1986). If one is only interested in a single portion of the reciprocal space, this method can already have a reasonable cost.

We finally note that future work should generally aim to: assess the signal-to-noise ratio of simulated diffraction patterns of a volume of refractive indices, representing realistic volumetric samples; simulate CDI experiments with complex sample-interaction mechanisms (Vartanyants *et al.*, 2007), and in combination with tomography and focusing optics. With respect to the simulated noise, it is of interest to characterize it statistically and assess whether it is Poisson-like as in real experiments and to relate the number of simulated rays to the simulated signal-to-noise ratio.

## 5. Conclusions

We reported a scheme for simulating CDI techniques in a ray-tracing framework. We have implemented it in the open-source simulator *McXtrace* and demonstrated its function for a novel problem in the configurations of full-field CDI and Ptychography in the far field and using a forward direction geometry. Possibly the main advantage of this method is to assist non-specialists in the simulation of coherent imaging experiments. All user-defined distances and parameters are real space quantities and do not need conversion to reciprocal coordinates, and allow for deviation from ideal test situations (translation or rotation of a component).

We acknowledge that like all Monte Carlo methods this one does not stand out for elegance (as it is not based on a physical insight of a setup) or efficiency and is hardly recommendable for standard cases where an analytical solution is available. However, this simple approach bears no attached hypothesis and is possibly extendable to less standard, unsolved cases; the scheme is suitable for GPU parallelization and therefore has wide room for improvement with regard to efficiency. The

rationale behind our endeavour is to eventually offload the complexity of a special setup to brute computational force. The main contribution of this paper lies in the definition of adequate constraints for simulation of diffraction, such as the sampling requirements and an estimate of the number of rays to trace to achieve a satisfactory signal-to-noise ratio. We believe that these are potentially applicable to the simulation of other untested CDI variants, although more tests are still to be made. In line with the open-source spirit of *McXtrace*, we trust that current and future users can exploit and help to develop the lines of inquiry mentioned in the outlook.

## 6. Related literature

The following references, not cited in the main body of the paper, have been cited in the supporting information: Nieuwenhuizen *et al.* (2013); Van Heel & Schatz (2005); Vila-Comamala *et al.* (2011); Huang *et al.* (2009).

## APPENDIX A Comparison with Fraunhofer propagator

In this section, we compare the ray-tracing simulation of diffraction from a single slit with the solution obtained with a numerical implementation of the Fraunhofer propagator,

$$\Psi(X, Y) = -\frac{j \exp(jkz)}{\sqrt{N_x N_y}} \exp\left(jk \frac{X^2 + Y^2}{z}\right) F(\psi), \quad (12)$$

in which  $N_x$  and  $N_y$  are the number of pixels in the horizontal and vertical directions. The single slit has 100 nm width; the detector has  $200 \times 200$  square pixels of  $400 \mu\text{m}$  size, corresponding to a detector size of  $8 \text{ cm} \times 8 \text{ cm}$  at a distance  $z = 4 \text{ m}$  from the slits. These parameters produce a real space pixel size of 5 nm, which is relatively far in reciprocal space. The comparison of the two cases is illustrated in Fig. 7. An overall agreement is found at low frequencies, whereas a slightly faster decay of intensity is observed for the Fraunhofer propagator solution, and a worse cancellation of the zeros is observed for the ray tracing due to the stochastic way it is achieved. The faster decay is highlighted in Fig. 8. A third comparison is made with the sinc pattern derived from geometrical optics, here recalled,

$$\Psi(X, Y) = \text{sinc}\left(\frac{wX}{\lambda z}\right) \text{sinc}\left(\frac{wY}{\lambda z}\right), \quad (13)$$

where  $w$  denotes the slit width,  $\lambda$  the wavelength and  $z$  the detector distance. The ray-tracing simulation shows a closer resemblance with this last function and shows significant relative deviation from the Fraunhofer approach at high angles. The decay is similar when other line profiles are evaluated. It is interesting in this case to define a cut-off in detector space where the two approaches match. We find that for  $|X| < 2 \text{ cm}$  the relative difference between them is below 10%.

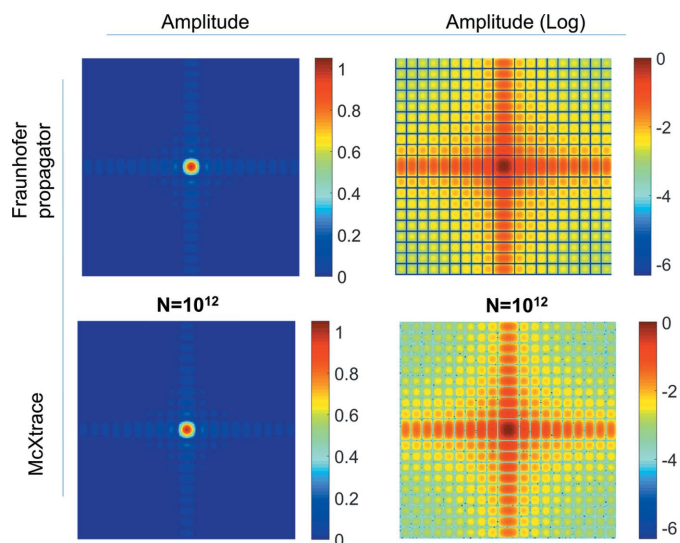


**Figure 7**  
Comparison of diffraction patterns from the Fraunhofer propagator and ray-tracing simulations from a single slit.  $N = 10^{12}$  rays are traced in the *McXtrace* simulation.

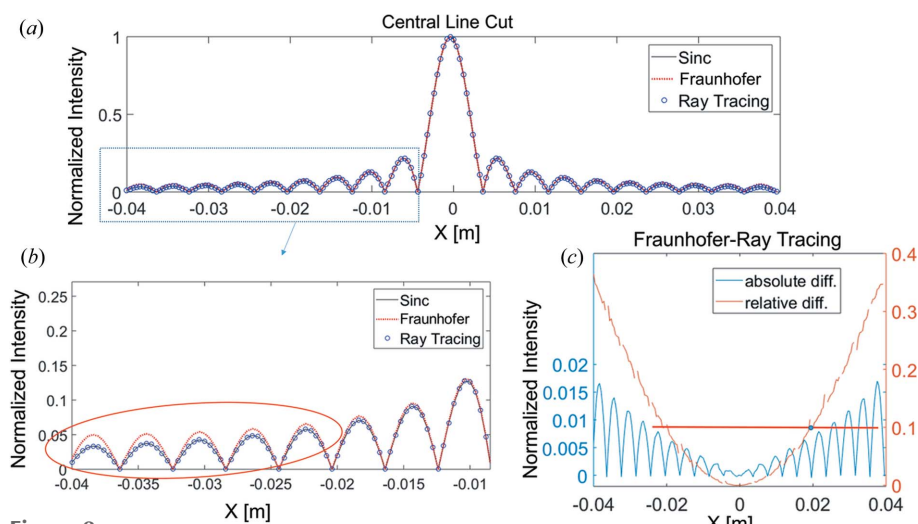


**Figure 8**  
Line-cut of a single-slit diffraction pattern taken in the centre of the diffraction at  $y = 0$ . The ray-tracing simulation is compared with the solution obtained with the Fraunhofer propagator and with the sinc function from geometrical optics. (a) Profile across the entire detector, showing an overall agreement among the three solutions; (b) the ray-tracing simulation matches the sinc pattern but deviates significantly from the Fraunhofer propagator solution at high frequencies; (c) plot of the difference between the Fraunhofer solution and ray tracing for a single line-cut. The difference is below 10% of the Fraunhofer solution for  $|X| < 2$  cm.

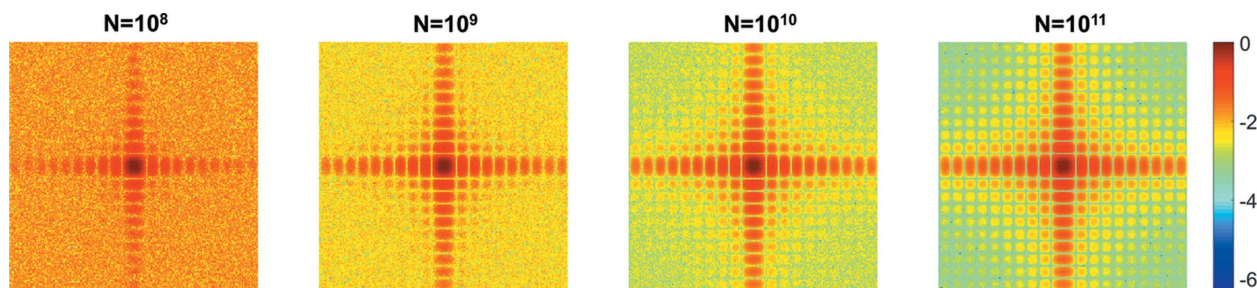


**Figure 9**  
Diffraction patterns of a single slit for an increasing number of simulated rays ( $N = 10^8$ – $10^{11}$ ). The same colour axis and scale refers to the four log scale plots. The weight of the rays is normalized by  $N$  so that the sum of all weights equals unity.

## APPENDIX B Characterization of noise in Monte Carlo ray tracing

We evaluate noise in the above-mentioned case of the single slit where satisfactory results are obtained even with a relatively low number of rays and, additionally, an analytical solution exists. For the analysis, we focus solely on the simulated amplitude of the diffraction patterns. Error is evaluated as the difference from the true solution. For that we refer to two options: the simulation of the highest number of rays and the sinc pattern from equation (13). We test numbers of rays ranging from  $10^8$  to  $10^{11}$ , whereas the best guess of a solution has  $10^{12}$  rays.

Figs. 9 and 10 show the strong signal–noise dependence (*i.e.* the noise pattern reflects the single slit patterns in Fig. 9) with the largest relative error for low signal, which is also a characteristic of Poisson counting statistics and points to a useful modelling of noise. Mean and variance of this noise do not match in this case in general, as it should be for a Poisson-like noise, but they obviously match for the event (the number of rays hitting a pixel) numbers on the detector [Fig. 11(a)]. This

second fact implies that when the flux is set to match the number of rays, and there is fully constructive interference, the counts are Poisson distributed. Aside from this case, the variance is not observed to match the mean counts for all pixels.

The norm of the error decreases as  $1/\sqrt{N}$  [Fig. 11(b)], as expected for a Monte Carlo method. The same conclusions apply whether the error is evaluated as the difference from the best guess with  $N = 10^{12}$ , or as the difference from the sinc pattern.

### Acknowledgements

We gratefully acknowledge P. S. Jørgensen, A. F. Pedersen, H. Simons and P. K. Willendrup for fruitful scientific discussions.

### Funding information

Data processing (Fourier ring correlation and ptychography reconstructions)

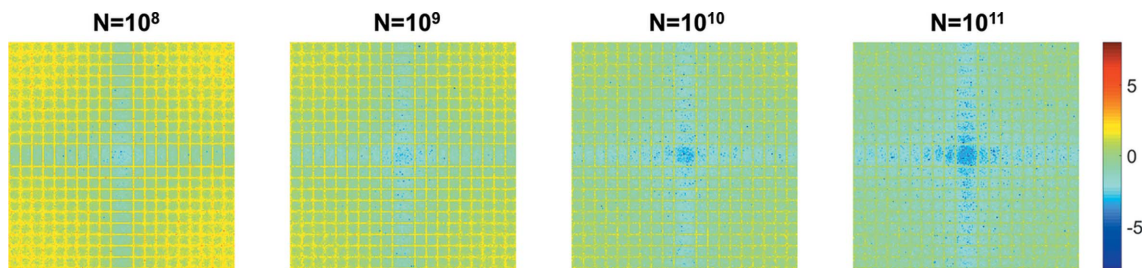


**Figure 10** Relative error patterns. The same colour axis and scale refers to the four log scale plots. The simulated patterns from Fig. 9 are subtracted from and normalized by the simulation with the largest number of traced rays ( $N = 10^{12}$ ). The total error decreases with increasing  $N$  and is higher where the signal is lower.

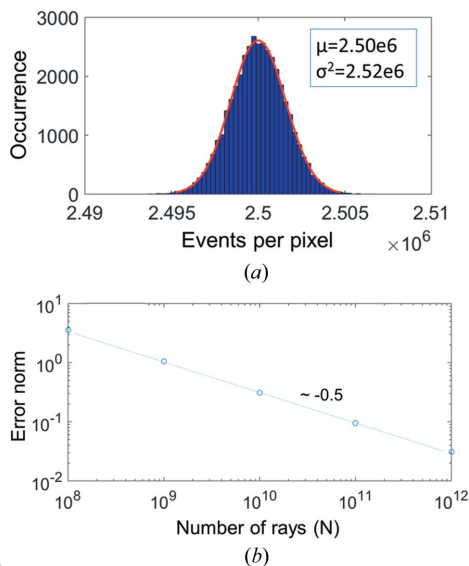


**Figure 11** (a) Event statistics, which follow a Poisson distribution; the reported case refers to  $N = 10^{11}$ . (b) Error trend on logarithmic axes. The total error is evaluated as L2-norm of the difference with the sinc pattern. The points fit on a straight line with  $-0.5$  slope.

was carried out using the cSAXS ptychography MATLAB package developed by the Science IT and the coherent X-ray scattering (CXS) groups, Paul Scherrer Institut, Switzerland. This study was supported by the European Research Council (ERC) under the European Union’s Horizon 2020 research and innovation programme (SEEWHI Consolidator grant No. ERC-2015-CoG-681881) and by the Ministry of Higher Education and Science (DANSCATT grant No. 7055-00007B).

**References**

Aarle, W. van, Palenstijn, W. J., De Beenhouwer, J., Altantzis, T., Bals, S., Batenburg, K. J. & Sijbers, J. (2015). *Ultramicroscopy*, **157**, 35–47.  
 Andreas, B., Mana, G. & Palmisano, C. (2015). *J. Opt. Soc. Am. A*, **32**, 1403.  
 Bahrtdt, J. (2007). *Phys. Rev. ST Accel. Beams*, **10**, 060701.  
 Bech, M., Bunk, O., David, C., Kraft, P., Brönnimann, C., Eikenberry, E. F. & Pfeiffer, F. (2008). *Appl. Radiat. Isot.* **66**, 474–478.  
 Bergbäck Knudsen, E., Prodi, A., Baltser, J., Thomsen, M., Kjær Willendrup, P., Sanchez del Rio, M., Ferrero, C., Farhi, E., Haldrup, K., Vickery, A., Feidenhans'l, R., Mortensen, K., Meedom Nielsen, M., Friis Poulsen, H., Schmidt, S. & Lefmann, K. (2013). *J. Appl. Cryst.* **46**, 679–696.

Chang, H., Enfedaque, P., Zhang, J., Reinhardt, J., Enders, B., Yu, Y.-S., Shapiro, D., Schroer, C. G., Zeng, T. & Marchesini, S. (2019). *Opt. Express*, **27**, 10395–10418.  
 Chapman, H. N. & Nugent, K. A. (2010). *Nat. Photon.* **4**, 833–839.  
 Chubar, O., Fluerasu, A., Berman, L., Kaznatcheev, K. & Wiegart, L. (2013). *J. Phys. Conf. Ser.* **425**, 162001.  
 Cipiccia, S., Vittoria, F. A., Weikum, M., Olivo, A., Jaroszynski, D. A., Dino, A. & Jaroszynski, D. A. (2014). *Opt. Express*, **22**, 2395–2398.  
 Colton, D. & Kress, R. (1992). *Inverse Acoustic and Electromagnetic Scattering Theory*, p. 121; p. 289. Springer: Berlin.  
 Dierolf, M., Menzel, A., Thibault, P., Schneider, P., Kewish, C. M., Wepf, R., Bunk, O. & Pfeiffer, F. (2010). *Nature*, **467**, 436–439.  
 Dietze, S. H. & Shpyrko, O. G. (2015). *J. Synchrotron Rad.* **22**, 1498–1508.  
 Godard, P., Allain, M., Chamard, V. & Rodenburg, J. (2012). *Opt. Express*, **20**, 25914–25934.  
 Hettel, R. (2014). *J. Synchrotron Rad.* **21**, 843–855.  
 Holler, M., Guizar-Sicairos, M., Tsai, E. H. R., Dinapoli, R., Müller, E., Bunk, O., Raabe, J. & Aeppli, G. (2017). *Nature*, **543**, 402–406.  
 Howells, M. R., Beetz, T., Chapman, H. N., Cui, C., Holton, J. M., Jacobsen, C. J., Kirz, J., Lima, E., Marchesini, S., Miao, H., Sayre, D., Shapiro, D. A., Spence, J. C. H. & Starodub, D. (2009). *J. Electron Spectrosc. Relat. Phenom.* **170**, 4–12.  
 Huang, X., Miao, H., Steinbrener, J., Nelson, J., Shapiro, D., Stewart, A., Turner, J. & Jacobsen, C. (2009). *Opt. Express*, **17**, 13541–13553.  
 Huang, X., Yan, H., Harder, R., Hwu, Y., Robinson, I. K. & Chu, Y. S. (2014). *Opt. Express*, **22**, 12634–12644.  
 Klementiev, K. & Chernikov, R. (2014). *Proc. SPIE*, **9209**, 92090A.  
 Kumar, P. B. S. & Ranganath, G. S. (1991). *Pramana J. Phys.* **37**, 457–488.  
 Lai, B. & Cerrina, F. (1986). *Nucl. Instrum. Methods Phys. Res. A*, **246**, 337–341.  
 Mahan, J. R., Vinh, N. Q., Ho, V. X. & Munir, N. B. (2018). *Appl. Opt.* **57**, D56–D62.  
 Maiden, A. M., Humphry, M. J. & Rodenburg, J. M. (2012). *J. Opt. Soc. Am. A*, **29**, 1606.  
 Maiden, A. M. & Rodenburg, J. M. (2009). *Ultramicroscopy*, **109**, 1256–1262.  
 Marchesini, S., Chapman, H. N., Hau-Riege, S. P., London, R. A., Szoke, A., He, H., Howells, M. R., Padmore, H., Rosen, R., Spence, J. C. H. & Weierstall, U. (2003). *Opt. Express*, **11**, 2344.  
 Mastropietro, F., Carbone, D., Diaz, A., Eymery, J., Sentenac, A., Metzger, T. H., Chamard, V. & Favre-Nicolin, V. (2011). *Opt. Express*, **19**, 19223–19232.  
 Mastropietro, F., Eymery, J., Carbone, G., Baudot, S., Andrieu, F. & Favre-Nicolin, V. (2013). *Phys. Rev. Lett.* **111**, 215502.  
 Miao, J., Charalambous, P., Kirz, J. & Sayre, D. (1999). *Nature*, **400**, 342–344.  
 Miao, J., Ishikawa, T., Robinson, I. K. & Murnane, M. M. (2015). *Science*, **348**, 530–535.  
 Mout, M., Flesch, A., Wick, M., Bociort, F., Petschulat, J. & Urbach, P. (2018). *J. Opt. Soc. Am. A*, **35**, 1356.



- Mout, M., Wick, M., Bociort, F., Petschulat, J. & Urbach, P. (2016). *Appl. Opt.* **55**, 3847–3853.
- Nieuwenhuizen, R. P. J., Lidke, K. A., Bates, M., Puig, D. L., Grünwald, D., Stallinga, S. & Rieger, B. (2013). *Nat. Methods*, **10**, 557–562.
- Noh, D. Y., Kim, C., Kim, Y. & Song, C. (2016). *J. Phys. Condens. Matter*, **28**, 493001.
- Pfeiffer, F. (2018). *Nat. Photon.* **12**, 9–17.
- Prodi, A., Knudsen, E., Willendrup, P., Schmitt, S., Ferrero, C., Feidenhans'l, R. & Lefmann, K. (2011). *Proc. SPIE*, **8141**, 814108.
- Ramos, T., Jørgensen, J. S. & Andreasen, J. W. (2017). *J. Opt. Soc. Am. A*, **34**, 1830–1843.
- Rebuffi, L. & Sánchez del Río, M. (2016). *J. Synchrotron Rad.* **23**, 1357–1367.
- Sanchez del Rio, M. & Rebuffi, L. (2019). *AIP Conf. Proc.* **2054**, 060081.
- Rodenburg, J. M. (2008). *Advances in Imaging and Electron Physics*, Vol 150, pp. 87–184. San Diego: Academic Press.
- Rodenburg, J. M. & Faulkner, H. M. L. (2004). *Appl. Phys. Lett.* **85**, 4795–4797.
- Schäfers, F. (2008). *Modern Developments in X-ray and Neutron Optics*, edited by A. Erko, M. Idir, T. Krist & A. G. Michette, pp. 9–41. Berlin, Heidelberg: Springer.
- Shapiro, D. A., Yu, Y.-S., Tyliczszak, T., Cabana, J., Celestre, R., Chao, W., Kaznatcheev, K., Kilcoyne, A. L. D., Maia, F., Marchesini, S., Meng, Y. S., Warwick, T., Yang, L. L. & Padmore, H. A. (2014). *Nat. Photon.* **8**, 765–769.
- Spence, J. C. H., Weierstall, U. & Howells, M. (2004). *Ultramicroscopy*, **101**, 149–152.
- Takahashi, Y., Zettsu, N., Nishino, Y., Tsutsumi, R., Matsubara, E., Ishikawa, T. & Yamauchi, K. (2010). *Nano Lett.* **10**, 1922–1926.
- Thibault, P., Dierolf, M., Menzel, A., Bunk, O., David, C. & Pfeiffer, F. (2008). *Science*, **321**, 379–382.
- Thibault, P. & Guizar-Sicairos, M. (2012). *New J. Phys.* **14**, 063004.
- Van Heel, M. & Schatz, M. (2005). *J. Struct. Biol.* **151**, 250–262.
- Vartanyants, I. A., Grigoriev, D. & Zozulya, A. V. (2007). *Thin Solid Films*, **515**, 5546–5552.
- Veen, F. & Pfeiffer, F. (2004). *J. Phys. Condens. Matter*, **16**, 5003–5030.
- Vila-Comamala, J., Diaz, A., Guizar-Sicairos, M., Manton, A., Kewish, C. M., Menzel, A., Bunk, O. & David, C. (2011). *Opt. Express*, **19**, 21333–21344.
- Zhu, C., Harder, R., Diaz, A., Komanicky, V., Barbour, A., Xu, R., Huang, X., Liu, Y., Pierce, M. S., Menzel, A. & You, H. (2015). *Appl. Phys. Lett.* **106**, 101604.

## 4.2 Supporting information

### 4.2.1 Effect of subvoxel size

The blurring effect mentioned in section 4.1 is illustrated in Figure 4-1. Such an effect is due to an improper choice of the subpixel size  $W$ . The effect starts becoming visible as the subvoxel size approaches the size of the illumination. In this case, the size of the grating covers a  $5 \times 5 \mu\text{m}^2$  area and the effects become visible with a  $0.1 \mu\text{m}$  subvoxel size.

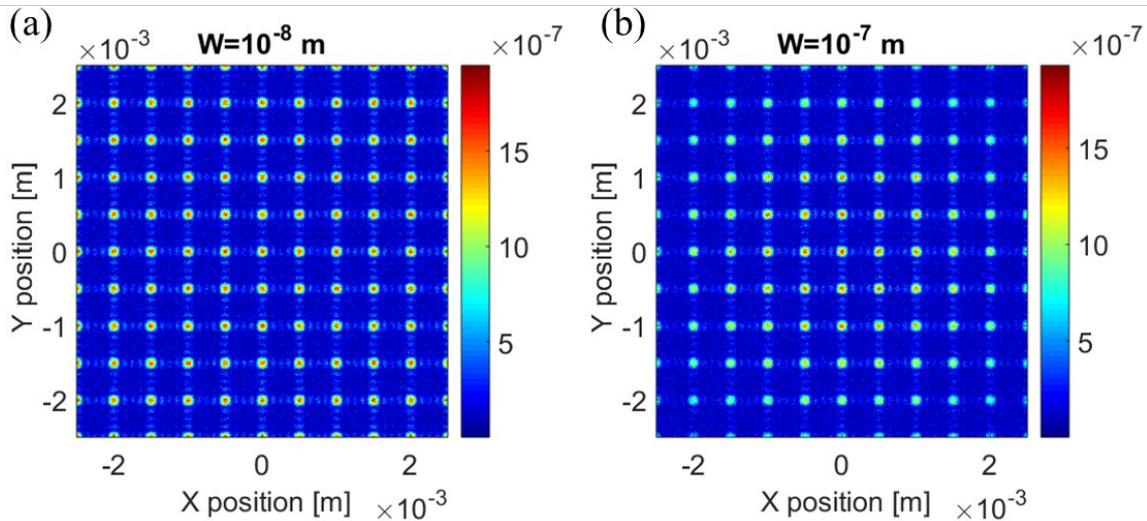


**Figure 4-1. Diffraction pattern of grating from section Results of section 4.1 for different subvoxel sizes. No blurring appears in (a), whereas the peaks at higher angular values are dampened in (b). In both patterns  $N=10^8$  rays are traced.**

### 4.2.2 Resolution assessment

We have used Fourier Ring Correlation (FRC) method [154], [155] to compare objects retrieved in the CDI and ptychography simulations. All plots are computed with the FRC function in the "cSAXS matlab package" [20].

As the comparison is made with the ground truth, we chose to use the 1-bit threshold criterion. Also, we only refer to the amplitudes of the retrieved objects, as the phases give overly pessimistic estimates due to phase wrapping artifacts present in the reconstructions.

## Full field CDI vs. Ptychography

A slightly smaller portion of the object has been used for FRC in the ptychography case, to exclude borders where reconstruction is less effective because of lower overlap. The areas used for the FRC are depicted in Figure 4-3.

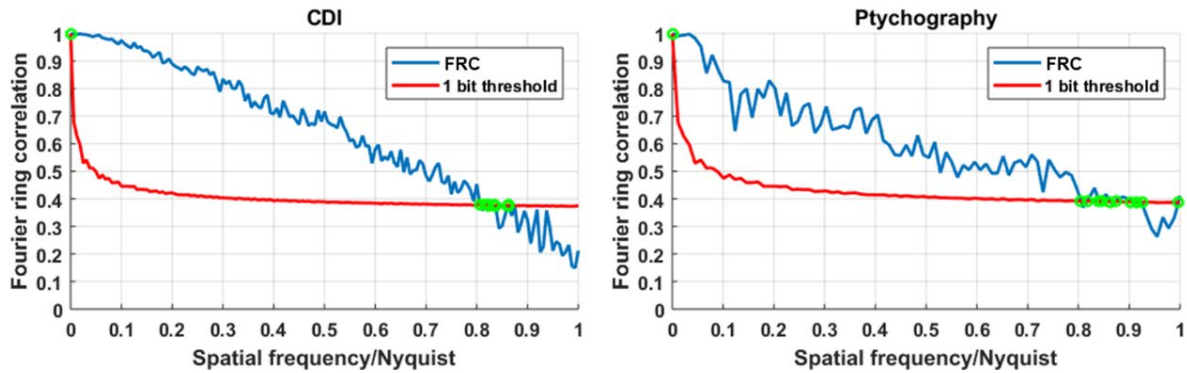


**Figure 4-2. Comparison of Fourier Ring Correlation for amplitudes of the objects retrieved from the CDI and the ptychography simulation. As correlations are independent of the reconstructed pixel size, different in the two cases, a comparison can be made. The object simulated and retrieved with ptychography correlates up to a higher frequency than that of CDI.**

**Table 4-1. Summary of FRC results for CDI and ptychography.**

	Reconstructed Pixel Size [nm]	Intersections [1] (min, max)	Resolution [nm] (max, min)	Average SNR [1]
CDI	25	(0.81, 0.86)	(31.0, 29.0)	5.53
Ptychography	14.29	(0.80, 0.99)	(17.8, 14.3)	3.33

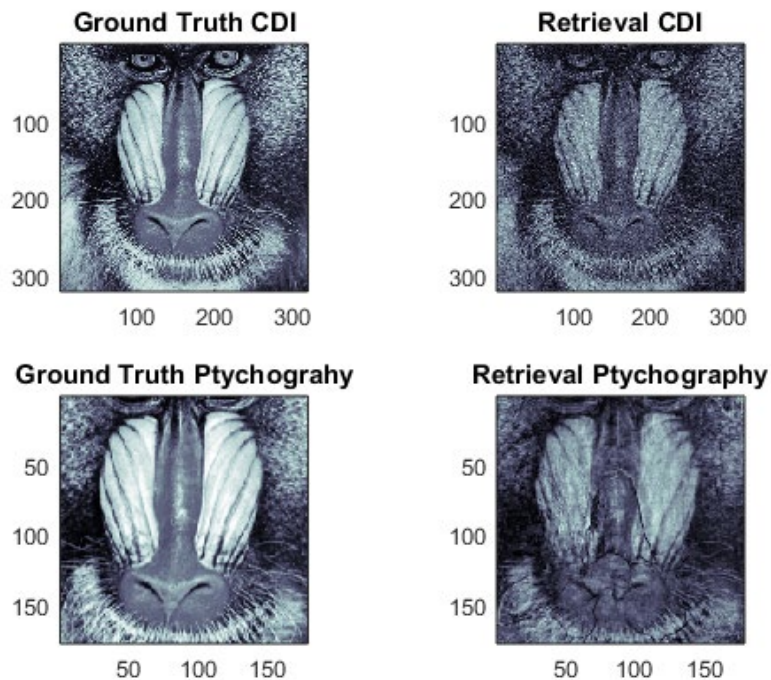


Figure 4-3. Areas of the retrieved objects' amplitudes selected for FRC.

### Speckle example, CDI

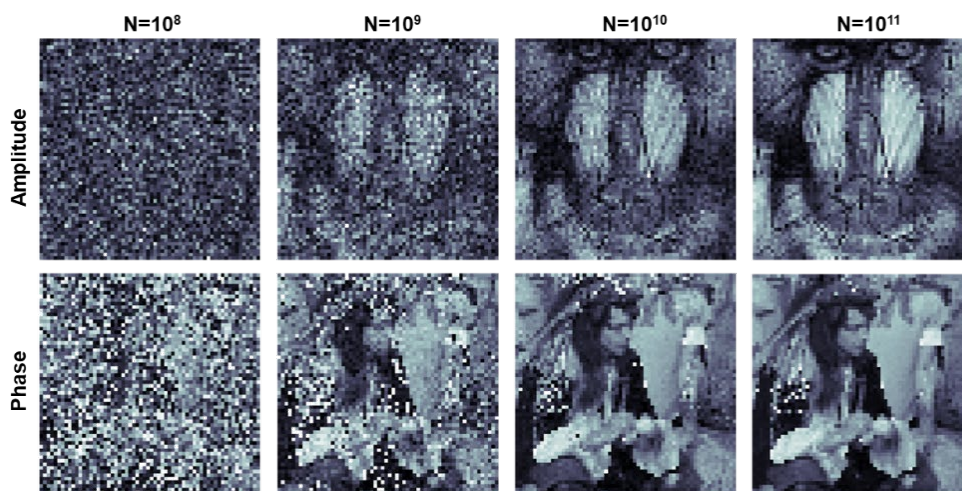
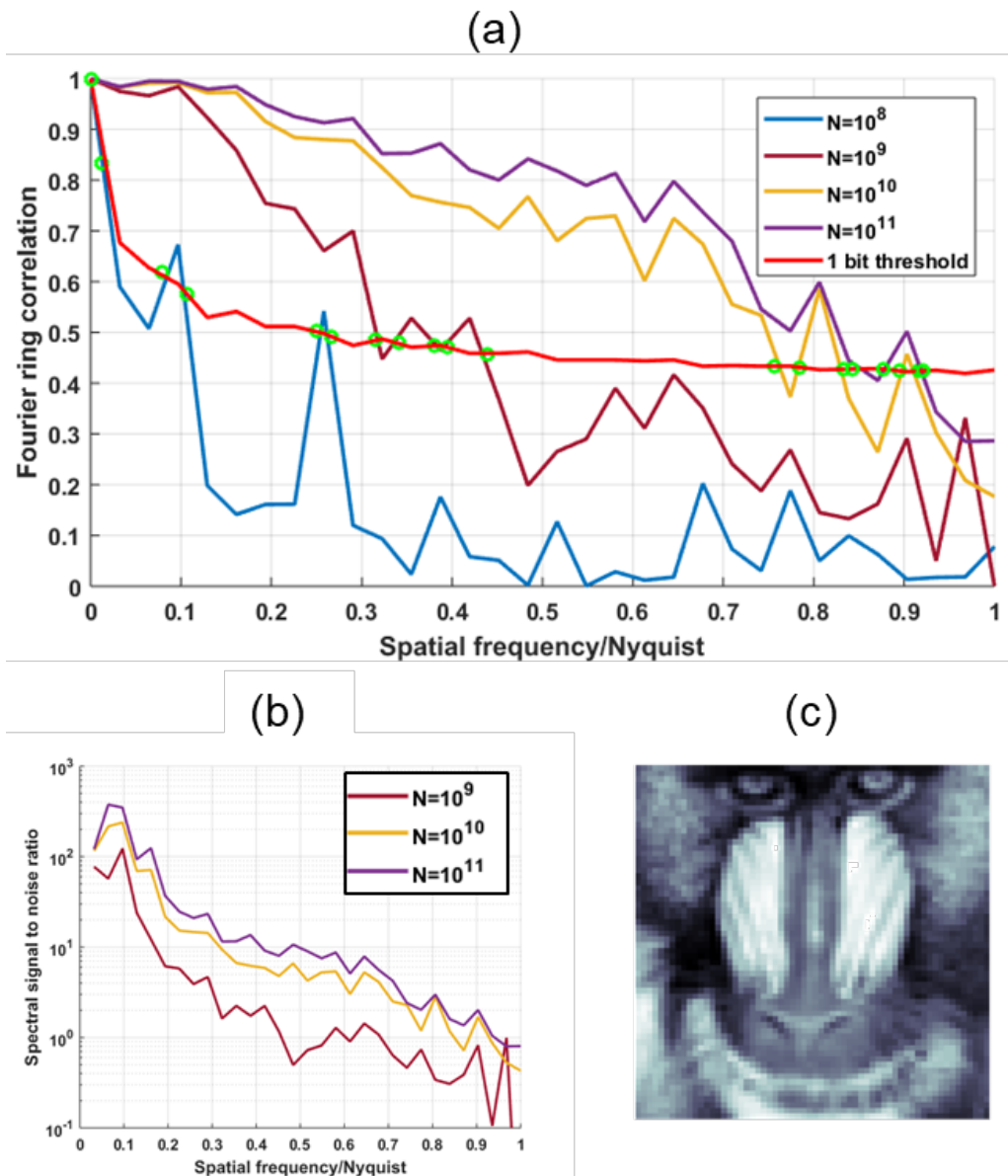


Figure 4-4. Inverse Fourier Transform of the speckle patterns in Figure 4 of section 4.1. Due to the reduced size of the detector, the reconstructed pixel size is larger than the previous example (125 nm) and therefore the retrieved object is represented on a  $72 \times 72$  pixel array.



**Figure 4-5. a) FRC of the four images in Figure 4-4; b) spectral signal to noise ratio for the three cases where a visible image is retrieved; c) ground truth correlated with the amplitude of the four images. The spectral signal to noise ratio is evaluated as in [156]. The average SNR from the spectral signal to noise ratio are respectively: 2.5; 7.5; 11.6 for the cases  $N = 10^9; 10^{10}; 10^{11}$ .**



## 5. Resonant X-ray Ptychographic Nano-Tomography of Kesterite Solar Cells

This article reports the 3D X-ray imaging of a complete, functioning, kesterite solar cell. It fulfills the experimental goal of the project by applying state-of-the-art 3D X-ray imaging techniques to image a kesterite solar cell.

Ptychographic tomography is a quantitative technique that provides an optical measurement of the electron density of the sample when the energy of the beam is far from absorption edges. This measurement is based on phase-contrast and thus depends on the real part of the scattering factor. Close to absorption edges, however, each element displays a reduced scattering power because of core electron resonance, which is the principle underlying our experiment, illustrated in Figure 5-1. This property confers elemental sensitivity to ptychography, which in turn gives us the opportunity to distinguish phases with similar electron density, but different chemical composition.

In the same figure, we plot an *apparent* electron density, which is the optical measurement we would have if we ignored the reduction in scattering power due to resonance. This is an artifice we use to compare measurements at different energies.

The comparisons made throughout the text involve the actual electron density of the material (when known) and the optical measurements taken off-resonance and at the resonant edges of Cu, Zn, and Sn. Throughout the paper, it is shown that the off-resonance measurement is in general very accurate, and that the effect of resonance on optical measurements of electron density, is small but measurable and reliable.

We show that standard ptychographic tomography alone would have highlighted important features of the device, such as the layer structure, voids, pinholes, and the grain morphology, and some secondary phases, but it would have overlooked some other features, like the Cu intermixed in the CdS layer and other secondary phases.

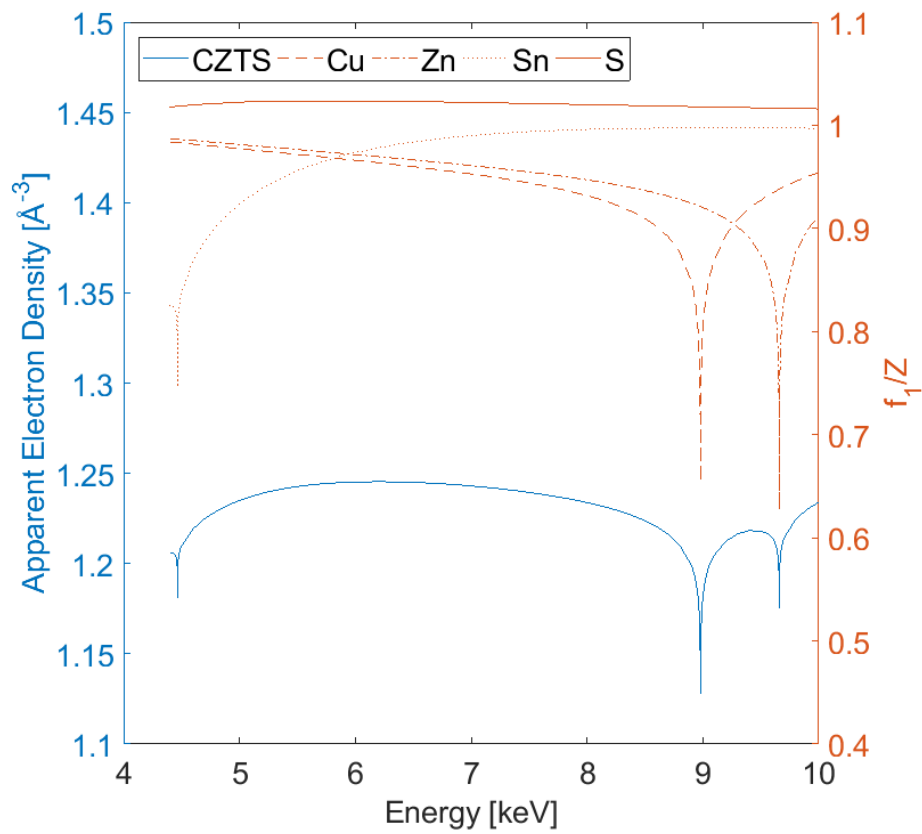


**Figure 5-1.** Apparent electron density of CZTS as a function of energy (blue line) and real part of atomic scattering factor  $f_1$  as a function of energy for Cu, Zn, Sn, S (orange lines).  $f_1$  is normalized to the atomic number of each element.

## 5.1 Journal Article 2



## Resonant x-ray ptychographic nanotomography of kesterite solar cells

**Fevola, Giovanni; Jørgensen, Peter S.; Verezhak, Mariana; Slyamov, Azat; Crovetto, Andrea; Balogh, Zoltan Imre; Rein, Christian; Canulescu, Stela; Andreasen, Jens Wenzel**

*Published in:*  
Physical Review Research

*Link to article, DOI:*  
[10.1103/physrevresearch.2.013378](https://doi.org/10.1103/physrevresearch.2.013378)

*Publication date:*  
2020

*Document Version*  
Publisher's PDF, also known as Version of record

[Link back to DTU Orbit](#)

*Citation (APA):*  
Fevola, G., Jørgensen, P. S., Verezhak, M., Slyamov, A., Crovetto, A., Balogh, Z. I., Rein, C., Canulescu, S., & Andreasen, J. W. (2020). Resonant x-ray ptychographic nanotomography of kesterite solar cells. *Physical Review Research*, 2(1), [013378]. <https://doi.org/10.1103/physrevresearch.2.013378>

---







### General rights

Copyright and moral rights for the publications made accessible in the public portal are retained by the authors and/or other copyright owners and it is a condition of accessing publications that users recognise and abide by the legal requirements associated with these rights.

- Users may download and print one copy of any publication from the public portal for the purpose of private study or research.
- You may not further distribute the material or use it for any profit-making activity or commercial gain
- You may freely distribute the URL identifying the publication in the public portal

If you believe that this document breaches copyright please contact us providing details, and we will remove access to the work immediately and investigate your claim.

## Resonant x-ray ptychographic nanotomography of kesterite solar cells

Giovanni Fevola <sup>1</sup>, Peter S. Jørgensen,<sup>1</sup> Mariana Verezhak,<sup>2</sup> Azat Slyamov <sup>1</sup>, Andrea Crovetto <sup>3,4</sup>, Zoltan I. Balogh,<sup>5</sup> Christian Rein <sup>1</sup>, Stela Canulescu <sup>6</sup>, and Jens W. Andreasen <sup>1,\*</sup>

<sup>1</sup>Department of Energy Conversion and Storage, Technical University of Denmark, DK-2800 Kgs. Lyngby, Denmark

<sup>2</sup>Paul Scherrer Institute, CH-5232 Villigen PSI, Switzerland

<sup>3</sup>Department of Physics, Technical University of Denmark, DK-2800 Kgs. Lyngby, Denmark

<sup>4</sup>Helmholtz-Zentrum Berlin für Materialien und Energie, D-14109 Berlin, Germany

<sup>5</sup>DTU Nanolab, Technical University of Denmark, DK-2800 Kgs. Lyngby, Denmark

<sup>6</sup>Department of Photonics Engineering, Technical University of Denmark, DK-2800 Kgs. Lyngby, Denmark



(Received 31 December 2019; accepted 21 February 2020; published 30 March 2020)

The  $\text{Cu}_2\text{ZnSnS}_4$  kesterite is currently among the most promising inorganic, nontoxic, earth-abundant materials for a new generation of solar cells. Interfacial defects and secondary phases present in the kesterite active layer are, however, detrimental to the performance of the device. They are typically probed with techniques that are destructive or limited to the surface, and x-ray diffraction cannot reliably distinguish small amounts of zinc sulfide or copper tin sulfide from kesterite. Conversely, resonant ptychographic tomography, which relies on electron density contrast, overcomes these limitations. Here, we demonstrate how this technique can enable localization and quantification of secondary phases, along with measurements of adherence at the interfacial layers, on complete and functioning devices. In our experiment, we utilize an x-ray energy value far from absorption edges as well as three single energies corresponding to the absorption edges of Cu, Zn, and Sn, to gain elemental sensitivity to these elements and enhance contrast between phases with similar electron density. As a result, we image and identify in the active layer grains of a secondary phase, namely, zinc sulfide, which is not easily discriminated by other standard characterization techniques. In addition, we are able to observe Cu diffused from the active layer into the CdS buffer layer as well as Cu in the form of copper sulfide at their interface. Other relevant morphological features are best resolved off-resonance at the optimal energy for the synchrotron beamline with  $\sim 20$  nm resolution.

DOI: [10.1103/PhysRevResearch.2.013378](https://doi.org/10.1103/PhysRevResearch.2.013378)

## I. INTRODUCTION

The  $\text{Cu}_2\text{ZnSnS}_4$  (CZTS) kesterite is regarded among the most promising inorganic, earth-abundant, nontoxic materials to employ as a bulk active layer in a new generation of thin-film solar cells [1]. This quaternary compound is a direct semiconductor, with intrinsic *p*-type conductivity, and a suitable bandgap (1.5 eV), which can also be tuned with Se alloying [2]. Besides these features, it shares with its successful parent chalcogenide technology of  $\text{Cu}(\text{In,Ga})\text{Se}_2$  (CIGS) a high theoretical efficiency (28% for kesterite), but while efficiency above 20% has been demonstrated for CIGS, the current record for kesterite is around 12% [3]. The lower performance of kesterite is largely attributed to the open-circuit voltage deficit, as outlined in previous studies [4]. The causes can be grouped into defects in the bulk kesterite [5], and defects at its interfaces with the buffer CdS layer [6] or with the  $\text{MoS}_2$  electrode [7]. In fact, the formation of pure kesterite is limited by a very unforgiving single-phase region

and defect chemistry [8,9] so that, in practice, secondary compounds (sulfides with different stoichiometry than CZTS) are likely to form together with the desired phase. It is well known that some secondary phases are more benign than others and that, for instance, it is preferable to grow kesterite in a Zn-rich environment, even though the effect on the nanoscale of these phases on a functioning device is not precisely known [2].

Some of the possible secondary phases are not easily detected. Cheng *et al.* were among the first to use SEM (scanning electron microscopy), Raman, and x-ray diffraction (XRD) to identify secondary phases in CZTS films [10]. They pointed out that although the main XRD peaks of CZTS, ZnS, and  $\text{Cu}_2\text{SnS}_3$  (CTS) overlap, one can identify three minor peaks that unambiguously characterize CZTS, but that does not rule out the potential presence of ZnS and CTS. The topic of detection and discrimination limits of secondary phases was investigated by Berg *et al.* [11], which highlighted that, besides complementing it with Raman, XRD can be further refined with Rietveld analysis. Even so, XRD can only discriminate these phases if they make up a large fraction of the overall film (at least 10% ZnS and 50% CTS). They also conclude that quantitative analysis is not possible for XRD and that ZnS is indiscernible for Raman with green light alone, even in ZnS-rich samples. In-depth Raman analysis [12] shows that with UV wavelengths ZnS is discerned due to the induced resonant vibrational modes. Likewise, Lafond *et al.* concluded that resonance of Cu and Zn is

\*jewa@dtu.dk

Published by the American Physical Society under the terms of the Creative Commons Attribution 4.0 International license. Further distribution of this work must maintain attribution to the author(s) and the published article's title, journal citation, and DOI.

determining to enhance contrast for detection of the Cu/Zn disorder with XRD [13]. The general conclusion by Kumar *et al.* is that “the defect concentration in CZTS is lower than the detectable limit for most techniques but sufficient enough for poor device performance” [9]. Hence, they emphasize the need in particular for novel characterization techniques and for a deeper understanding of defects and secondary phase formation.

Conventional techniques for secondary phase characterization are either destructive or are applied at an intermediate stage of the fabrication of the device. As the active layer is polycrystalline, with grains that can be larger than a micron, a full device should contain at least a few of these grains and be therefore at least a few microns in size. X-ray ptychographic tomography [14] makes it possible to quantitatively image a volume with a few tens of microns thickness and is thus uniquely suitable for a nanoscale investigation of a full device. The capabilities offered by the technique when applied to organic thin-film solar cells have been elucidated by previous experiments [15,16]. For the case of kesterite, however, despite the remarkable overall accuracy of the technique [17], secondary phases can lack sufficient contrast with respect to the main compound. In fact, Cu and Zn being neighboring elements in the periodic table, the relative difference in electron density can easily be below the limits of detection [17]. On the other hand, resonant x-ray ptychographic tomography (RXPT) [18] has been introduced to provide not only elemental sensitivity but also information on the chemical state. The method relies on the reduction in scattering power exhibited by a given element when the beam energy matches an absorption edge and, in its near-edge version, can be seen as the combination of x-ray absorption spectroscopy with ptychographic tomography. RXPT has already been applied to functional materials to detect a single element of interest (Fe) [19] and its oxidation state [20]. More recently, RXPT was reported in the soft x-ray regime, in the near-edge case (also referred to as spectroptychographic tomography) [21,22], and notably probing two different elemental edges (Zn-L<sub>1</sub> and Al-K) [23]. Here we apply RXPT for the first time to a solar cell, where we illustrate that kesterite makes an interesting case, in which certain phases risk being overlooked by standard ptychographic tomography alone. In addition to the standard off-resonance energy, we probe three additional energies corresponding to characteristic x-ray absorption edges of Cu, Zn, and Sn in a wide energy range (4.5 to 9.7 keV), to gain elemental sensitivity to these elements and discriminate secondary phases. We demonstrate that alterations of electron density contrast are a means to highlight important features in solar devices.

## II. METHODS

### A. Sample description and preparation

The fabrication process of the investigated kesterite solar cells is described by Cazzaniga *et al.* [24]. The layer stack is a conventional architecture used in kesterite solar cells. Briefly, the precursors of CZTS are deposited on Mo-coated soda lime glass (SLG) substrates from ablation of a CZTS target in vacuum. The precursors grown by pulsed layer deposition (PLD) are annealed in a high-temperature sulfurized

atmosphere, where the kesterite (<450 nm) and the MoS<sub>2</sub> (500 nm) layers are formed. Subsequently, a CdS buffer layer (60 nm) is produced by chemical bath deposition (CBD) [25]; the intrinsic ZnO window layer (50 nm) and the Indium Tin oxide (ITO) contact layer (200 nm) are deposited by sputtering; an MgF<sub>2</sub> anti-reflection coating (100 nm) is finally evaporated.

Two cylindrically shaped samples with a diameter of 5  $\mu\text{m}$  were prepared with the focused ion beam (FIB) lift-out technique [26] from the complete kesterite solar cells and mounted on OMNY pins [27]. Images from this process are available in the Supplemental Material [28], Fig. S1. The samples, hereafter referred to as E1 and E2, were milled out of two kesterite solar cells whose electrical parameters are given in Table S1. These two areas were intentionally selected from solar cells of significantly different efficiencies (1.6% for E1, 0.8% for E2). The layer stack is a conventional geometry used in kesterite solar cells.

### B. Experimentals

RXPT was carried out at the cSAXS beamline of the Swiss Light Source (SLS) at the Paul Scherrer Institute, Villigen, Switzerland, using the fIOMNI setup described in detail elsewhere [29]. The energies for tomography were selected after an energy scan of ptychographic projections with 1 eV resolution over a region of the kesterite active layer. The selected values are reported in Table I. For RXPT we used photon energies of 6.20 keV (off-resonance), 8.99 keV (Cu K-edge), 9.67 keV (Zn K-edge), and 4.47 keV (Sn L<sub>1</sub>-edge). The sample was placed after the focal spot defined by a Fresnel Zone Plate [30] where the beam had a diameter of approximately 3  $\mu\text{m}$  for each energy. The ptychographic scans were performed with a  $9 \times 3 \mu\text{m}$  field of view (H  $\times$  V), following a Fermat spiral pattern [31] with a step size of 300 nm. Exposure time was set to 0.1 s for all scans except for those at 4.47 keV, for which decreased flux was counteracted by doubling the exposure time. Scan duration was approximately 5 hours for each tomogram. Radiation damage was assessed by visual inspection of the three dimensional (3D) reconstructions and by cross-correlation alignment of the ptychographic projections versus measurement time. Despite the repeated measurement of each sample, there is no clear evidence of radiation damage on the scale of observation, although that cannot be ruled out on a finer scale (see note in Supplemental Material [28]).

The ptychographic projections were reconstructed using cSAXS Matlab code in an area of  $800 \times 800$  pixels of the Eiger detector placed 5268 mm downstream from the sample, resulting in a pixel size and resolution stated in Table I using 300 iterations of the difference map algorithm [32] followed up by 500–900 iterations of a maximum likelihood refinement [33]. For tomography, 280 projections equally spaced in a 180-degree angular range were recorded. The phase of the reconstructed projections was used after post-processing alignment and removal of constant and linear phase components, and a modified filtered back projection algorithm was applied for the tomographic reconstruction [34,35]. The 3D resolution from Table I was determined by Fourier shell correlation (FSC) [36,37] with the 1/2-bit threshold criterion.

TABLE I. Energies probed with RXPT and resolution assessment of the resulting tomograms.

Edge	Off-resonance	Cu (K-edge)	Zn (K-edge)	Sn (L1-edge)
Symbol	$\lambda_{\text{off}}$	$\lambda_{\text{Cu}}$	$\lambda_{\text{Zn}}$	$\lambda_{\text{Sn}}$
Energy [keV]	6.201	8.986	9.666	4.468
Electron Binding Energy in Natural Form [keV]	—	8.979	9.659	4.465
Voxel size [nm]	17.55	25.24	18.77	24.36
3D resolution from FSC [nm]	17.55	25.98	18.77	24.54
2D resolution based on line profiling [nm]	26	31	37	27

The FSC method over an interior region of the whole stack results in values close to single pixel resolution due to very high contrast features with very sharp interfaces (e.g., MgF<sub>2</sub>-ITO or Mo-MoS<sub>2</sub> interface). However, based on averaged line profiles over 3 cuts across the Mo-MoS<sub>2</sub> interface (also see Fig. S2), we obtain slightly worse estimates of resolution reported in Table I.

### C. Theoretical basis

The theory behind resonant ptychographic tomography is described in its first experimental demonstration [18] and can be summed up as follows. Tomography measures the sample as a volume of complex refractive indices  $n = 1 - \delta + j\beta$ , where  $\beta$  relates to the absorption and  $\delta$  to the phase shift of the single voxel. The dependence on the wavelength of refractive indices can be traced back to the atomic scattering factor  $f_0 = f_1 + jf_2$ , and they are related as follows:

$$\begin{aligned} n(\lambda) &= 1 - \delta(\lambda) - j\beta(\lambda) \\ &= 1 - \frac{r_0}{2\pi} \lambda^2 \sum_k n_{\text{at}}^k [f_1^k(\lambda) + jf_2^k(\lambda)], \end{aligned} \quad (1)$$

$$\begin{aligned} \delta_{\text{off}} &= \frac{r_0}{2\pi} \lambda^2 [n_{\text{at}}^{\text{Cu}} f_1^{\text{Cu}}(\lambda_{\text{off}}) + n_{\text{at}}^{\text{Zn}} f_1^{\text{Zn}}(\lambda_{\text{off}}) + n_{\text{at}}^{\text{Sn}} f_1^{\text{Sn}}(\lambda_{\text{off}}) + n_{\text{at}}^{\text{S}} f_1^{\text{S}}(\lambda_{\text{off}})], \\ \delta_{\text{Cu}} &= \frac{r_0}{2\pi} \lambda^2 [n_{\text{at}}^{\text{Cu}} f_1^{\text{Cu}}(\lambda_{\text{Cu}}) + n_{\text{at}}^{\text{Zn}} f_1^{\text{Zn}}(\lambda_{\text{Cu}}) + n_{\text{at}}^{\text{Sn}} f_1^{\text{Sn}}(\lambda_{\text{Cu}}) + n_{\text{at}}^{\text{S}} f_1^{\text{S}}(\lambda_{\text{Cu}})], \end{aligned} \quad (3)$$

where  $\delta_{\text{Cu}}$  is the on-resonance measurement at the Cu edge. When subtracting the two, the term  $n_{\text{at}}^{\text{Zn}} (f_1^{\text{Zn}}(\lambda_{\text{off}}) - f_1^{\text{Zn}}(\lambda_{\text{Cu}}))$  can hardly be neglected, and if included adds its own uncertainty to the sum.

Therefore, in our analysis, we refer to the quantity

$$n_e(\lambda) = \frac{2\pi \delta(\lambda)}{\lambda^2 r_0}, \quad (4)$$

to examine contrast variations at the different energies.  $n_e$  provides an indirect, optical measurement of the electron density of the material. Such measurement closely matches the actual electron density far from absorption edges, whereas it gives a lower, *apparent* electron density in proximity of the edges. Differently from  $\delta$ ,  $n_e$  accounts for the strong  $\sim \lambda^2$  dependence and can therefore be compared for the four energies. An apparent electron density lower than the expected one signals the presence of a resonating element.

where  $k$  refers to the  $k$ th atomic species,  $n_{\text{at}}$  is the atomic density of such species,  $r_0$  is the classical electron radius, and  $j$  is the imaginary unit.  $f_1$  and  $f_2$  are the dispersion corrections to the atomic scattering factor that modifies both phase and absorption contrast of a voxel. RXPT relies on the fact that  $f_1$  exhibits a dip in the proximity of resonant edges, whereas it equals the atomic number of the element otherwise. If the  $k$ th element is the only one close to a resonant edge, its atomic density can be obtained by subtracting tomograms measured on-resonance and off-resonance:

$$n_{\text{at}}^k = \frac{1}{\Delta f_1^k} \frac{2\pi}{r_0} \left( \frac{\delta_{\text{off}}}{\lambda_{\text{off}}^2} - \frac{\delta_{\text{on}}}{\lambda_{\text{on}}^2} \right), \quad (2)$$

where  $\Delta f_1^k = f_1^k(\lambda_{\text{off}}) - f_1^k(\lambda_{\text{on}})$ . Although the measurements taken are in principle sufficient to determine the atomic density of elements in kesterite (including S), in our case the precise determination of the atomic density is not the optimal strategy to distinguish between phases, as the factor  $\Delta f_1^k$  can be strongly affected by element speciation. Besides, even assuming pure kesterite, the Cu and Zn edges are not distant enough to assume that Cu's contribution cancels at Zn edge and vice versa. In symbols, with respect to  $\delta$ , Eq. (1) in our case becomes

### D. Data post-processing

The expected values of  $\delta$  or  $n_e$  can be accurately computed with Eq. (1) using an experimental scattering factor database [38] when resonance does not occur. These predictions give an excellent match with measured values (see section Results and Discussion). For instance, ZnS and CZTS values, which are the only easily noticeable peaks in the bulk layer histogram differ by less than 2%. It is a more complicated matter to predict the expected  $\delta$ /apparent density of secondary phases if they contain elements for which the absorption edge is shifted due to possibly different oxidation state and specific near edge fine structure. Therefore, the following procedure is conceived to scan tomograms for secondary phases and identify them.

First, we consider the list of secondary phases that are most likely to be found in kesterite. We predict the phase and absorption contrast using Eq. (1), as shown in the Supplemental Material [28].



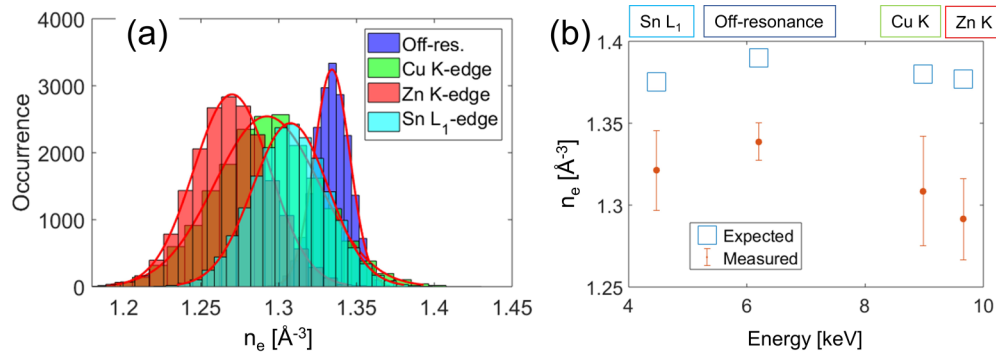


FIG. 1. Histograms of electron density value for voxels in a  $\text{MoS}_2$  slice of E1 (a) and comparison with calculated  $\delta$  of  $\text{MoS}_2$  from tabulated values (b). The measured values are about 95% of the expected ones.

Then, for any given secondary phase:

(1) The expected value of electron density is computed for all tomograms which are off-resonance for that phase. For example, for  $\text{Cu}_3\text{SnS}_4$  we predict the expected  $n_e(\lambda_{\text{off}})$  and  $n_e(\lambda_{\text{Zn}})$ .

(2) Voxels with those expected values are segmented out by thresholding. The dispersions computed from the  $\text{MoS}_2$  analysis (see below) are used to define the upper and lower threshold, with a coverage factor of 3. For example, for  $\text{Cu}_3\text{SnS}_4$  we consider the voxels that fit the range of the predicted values in the tomograms measured at  $\lambda_{\text{off}}$  and  $\lambda_{\text{Zn}}$ . Because of similar electron density, other phases (CZTS) mainly, might also be included in this range.

(3) Multivariate histograms of the segmented voxels are computed to highlight different peaks and associations. For example, for  $\text{Cu}_3\text{SnS}_4$ , histograms of  $n_e(\lambda_{\text{Cu}})$  and  $n_e(\lambda_{\text{Sn}})$  are computed for the voxels previously segmented.  $\text{Cu}_3\text{SnS}_4$  can be distinguished from CZTS at this point because of its higher Cu atomic density and therefore lower  $n_e(\lambda_{\text{Cu}})$ .

The tomograms of E1 and E2 were interpolated to the largest voxel size of the available tomograms at different energies. That corresponds to 25 nm of the Cu tomogram for E1 and of the Sn tomogram for E2. The interpolation is made with an FFT-based function and the subsequent alignment with a subpixel registration procedure [39].

### E. Uncertainty

The outstanding quantitiveness of ptychographic nanotomography has been discussed by Diaz *et al.* [17]. Because of upgrades to the beamline and because the resonant scans are taken in different conditions, we need to reevaluate uncertainty. We have used the same approach as Diaz *et al.* to assess quantitiveness of our measurements. Absolute values for dispersion of measurements can be assumed to be independent of the average measured values. Therefore, such deviation can be measured in any uniform volume, including air, and then used as tolerance for thresholding around an expected value.

The  $\text{MoS}_2$  layer is used as a reference to estimate the uncertainty of each tomogram. The hypothesis, in this case, is that it is a relatively uniform layer and shows little or no subvoxel porosity. The distribution of measured electron density is displayed in Fig. 1. The measurements are numerous enough to fit well a Gaussian. Means and standard deviation

are summed up in Table II. The illustrated statistics refer to sample E1, but the same values are also found in E2, confirming reproducibility of the measurements. The values computed according to Eq. (1) fit the trend of the slight dependence with energy. The measured values suggest an average of  $5 \pm 1\%$  subvoxel porosity of the layer. It is worth pointing out in this instance the error bias of reporting the electron density of a set of voxels on histograms, as voxels can be partially filled by material whereas they cannot be over-filled. Therefore histograms are more likely to be overpopulated on the low end than the high, leading to underestimation of the average value.

## III. RESULTS AND DISCUSSION

Two solar cells (herein referred to as E1 and E2) were inspected and prepared with focused ion beam (FIB) as 5  $\mu\text{m}$  in diameter and 2  $\mu\text{m}$  minimal height cylindrical samples for tomography. They were imaged with a 3D resolution between 18 and 37 nm at four x-ray energies. The slices and volume rendering we report here display the indirect optical measurement  $n_e$  of the electron density of materials, which is in general what ptychography provides in off-resonance conditions. However, elemental resonance induces a reduction in the scattering power of given elements, which results in the measurement of a lower *apparent* electron density. For further details about samples and the theoretical basis for our experiment refer to Sec. II. The results are organized in three subsections presenting, respectively: morphological features observed in off-resonance tomograms; chemical features highlighted by the combined analysis with resonant phase tomograms; a comparison between phase and absorption-based tomograms. The other two subsections include a discussion of the obtained results as well as a brief outlook on future experiments.

### A. Morphological features

As expected from previous studies, the whole layered structure is accurately resolved by ptychographic nanotomography. As illustrated by Fig. 2(a), there is sufficient contrast between all adjacent layers. The kesterite layer has a nominal electron density close to that of CdS and  $\text{MoS}_2$  (see Table S2), but even a rough threshold-based segmentation

TABLE II. Average measured electron density in MoS<sub>2</sub> slice comprising ca. 20 000 voxels. Off-resonance, the dispersion of values is less than 1% of the measured value and is below 3% in all cases. The small mean values measured in the air surrounding the sample are subtracted from the whole tomogram to correct for nonzero-mean noise.

	Mean	Standard deviation	Percent deviation	Air	Air-adjusted
	[Å <sup>-3</sup> ]	[Å <sup>-3</sup> ]	[%]	[Å <sup>-3</sup> ]	[Å <sup>-3</sup> ]
Off-resonance	1.33	0.012	0.86	-0.005	1.34
Cu K-edge	1.29	0.034	2.60	-0.017	1.31
Zn K-edge	1.27	0.025	1.94	-0.023	1.29
Sn L <sub>1</sub> -edge	1.31	0.024	1.86	-0.014	1.32

can distinguish the three layers. The only exception is the couple of layers between the active kesterite layer and the ITO electrode layer. Even in the higher resolution tomograms, the CdS *n*-type layer and the electron transport ZnO layer, which

are both around 50 nm in thickness and have been observed with SEM [24], cannot be clearly distinguished at any energy, but they are instead somehow mixed in a single layer of 4–5 voxels. Most importantly, although the electron density of CdS and particularly of ZnO is not lower than that of kesterite, a 4–5 voxels thin double layer appears with a lower electron density compared to kesterite. This is shown on the cross-sectional profile plot in Fig. 2(b), where a distinguishable dip in electron density between the kesterite and the ITO layers can be observed. Based on observations at other energies, we later elaborate on the analysis of this layer.

The profile plot also illustrates a relatively good match between measured and expected electron density of the layers (Table S2). The slightly lower values for the MoS<sub>2</sub> and the ITO layers can be attributed to variation in the stoichiometry and/or to subvoxel porosity. For ITO in particular, the apparent electron density of this layer measured at the Sn edge is lower because of In, which presents an appreciable decrease of scattering power at that energy. For the off-resonance tomogram, the distribution of electron densities as measured on each voxel follows that of the phase  $\delta$ , which is reported later when it is compared to that of the absorption  $\beta$ .

Figure 3 shows morphological features in the obtained tomograms. Our analysis focuses on the active layer (kesterite) and its interfaces with CdS and MoS<sub>2</sub>. The interface between kesterite and MoS<sub>2</sub> (the latter being formed as well during the sulfurization process) appears to be very smooth and there is no particular detail to highlight aside from a couple of pinholes [d1 in Fig. 3(a)]. Other features visible in our tomograms include a discontinuity in the ITO layer (d2), thinning of the CZTS layer (d3), and some larger CdS precipitates in the buffer layer (d4) due to the CBD process. These features can be observed in the movie S1 provided in Supplemental Material [28].

Figure 3(b) depicts the morphology of the grains in the upper part of the kesterite layer. With a layer thickness of ca. 400 nm and a voxel size of 25 nm, the layer is imaged in 16 slices. From the 4 top slices shown in Fig. 3(b), it can be noticed that the grain contours appear better defined in the higher part of the layer, where grain separation increases. Grain contours can be observed at all energies, although they are evidently best resolved at the off-resonance energy because of the better resolution, as shown in Fig. 3(c). Individual grains can be distinguished due to the presence of wider grain boundaries, i.e., voids considerably wider than the lattice parameter. In fact, although we refer to them as grains, they are likely to contain subgrains with different lattice orientations but without any gap. For the latter there will be no

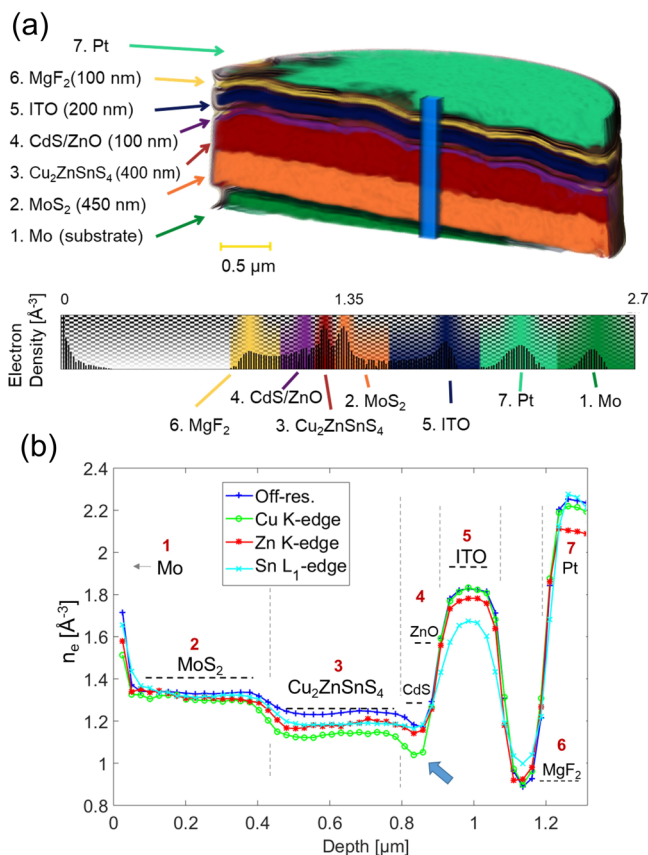


FIG. 2. (a) Volume rendering of the layer stack from the resulting tomographic reconstruction of sample E1. Layers are enumerated in ascending order from bottom to top and their expected size are reported in parenthesis. False colors are assigned as in the colorbar to the main peaks of the histogram of electron densities to distinguish between the layers. (b) Apparent electron density profile of E1 sample at the different energies. The profile is evaluated across the blue slab in the center of (a), averaging on an area of  $8 \times 8$  pixels ( $200 \times 200 \text{ nm}^2$ ). Profile measurements can be compared to the actual electron densities of the compounds (dashed black lines), also reported in Table S2. The area is chosen within a regular grain, with flat surface and no additional features. The dip of electron density in proximity of the CdS layer measured at Cu edge is interpreted as evidence of Cu migration into the layer.



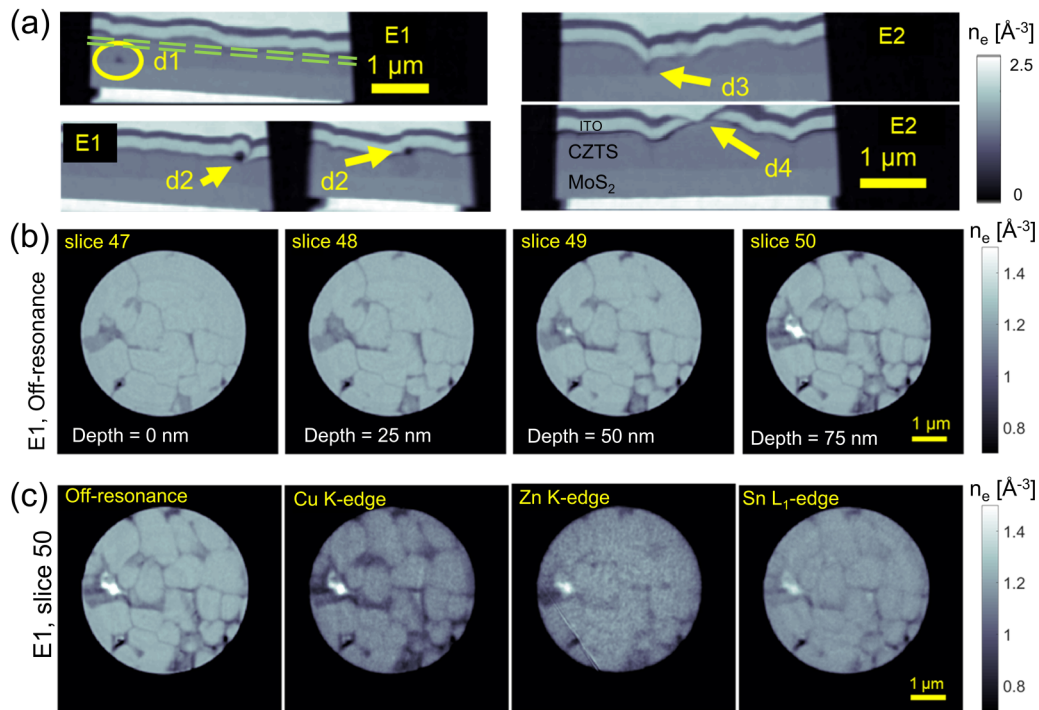


FIG. 3. Morphological features from phase tomograms of the CZTS layer. (a) Sagittal slices of E1 and E2 highlighting different types of defects: pinholes (d1), CdS precipitates (d2), thinning of CZTS layer (d3), discontinuity of ITO (d4). The dashed green lines in E1 indicate the range of depth of axial slices illustrated next. (b) Grain morphology of the active layer illustrated by four consecutive axial slices of the active layer, from bottom (slice 47) to top (slice 50). Distance between each slice equals the voxel size (25 nm). Grain size is around 1  $\mu\text{m}$  and the grain boundaries are clearly resolvable. (c) A comparison of the same slice at different edge energies showing that morphological features are best highlighted at the off-resonance energy. The colorbar is truncated in (b) and (c) to enhance gray level contrast.

appreciable change in electron density on the nanometer scale (ca. 20 nm) and the structure would appear homogeneous at the experimental resolution. Aside from sporadic voids, the lower part of the kesterite layer appears compact up to the voxel level, and the well-defined grain contours fade although a grain separation still exists. As previously observed with SEM, average grain lateral size is around 1  $\mu\text{m}$  [24]. For a 3D view of the grain morphology in E1 refer to movie S2 of Supplemental Material [28].

### B. Chemical features

Differences between aligned tomograms recorded at different energies reveal information about secondary phases. The CZTS layer correctly displays a decreased electron density compared to the off-resonance case, confirming that the scan energy at every resonant edge has been correctly selected. The measured electron density off-resonance is  $1.237 \text{\AA}^{-3}$ , in excellent agreement with the  $1.246 \text{\AA}^{-3}$  calculated with Eq. (1) (see Sec. II) and with the  $1.26 \text{\AA}^{-3}$  deduced from material properties (Table S2). This value is shifted down to 1.117, 1.142,  $1.167 \text{\AA}^{-3}$  when measured at Cu, Zn, and Sn edge-energies, respectively, which in all cases are 10% below the original value. The shift is clearest at the Cu edge because Cu is the most abundant element in kesterite.

Following previous characterization results [24], it is reasonable to assume that most of the active layer's composition is pure CZTS, and if secondary phases are present they are likely to be a minority given our measurements of the device

performance. The most legitimate objection to this argument is that most of the bulk layer (#3 in Fig. 2) might be CTS, which still can perform as a decent absorber material and has virtually the same density as kesterite. However, relying on our data, that is ruled out by the fact that most of the bulk layer exhibits a decrease in apparent electron density when scanned at the Zn edge, whereas CTS would not, being Zn-free. Some chemical features are depicted in Fig. 4. The most evident difference between the energy tomograms are some grains of a few hundred nm in E2 and three larger ones in E1. They extend roughly from bottom to top of the active layer in height, and they have a size of up to 500 nm. A 3D view of these grains and their localization in the active layer of E1 is available in movie S2. As shown in Fig. S3 and Table S3, these grains are identifiable as ZnS. The difference between the on- and off-resonance measurements increases at Zn edge and the electron density measured off-resonance is compatible with the expected values of this phase.  $\text{SnS}_2$  phase would also be possible but is excluded in this case as no inversion of contrast with kesterite at Cu edge is observed (see Fig. S3). Instead, contrast with the main phase is decreased at Cu- and Sn- edges, which is as expected for ZnS.

The bivariate histograms of Fig. 5 illustrate the case of ZnS. These histograms are computed including voxels with electron density within the predicted range of ZnS, at all energies except for the Zn-edge energy. Porous voxels of other material at interfaces or at grain boundaries also fall within this range. Therefore, when the correlation between apparent (on-resonance) and actual (off-resonance) electron densities

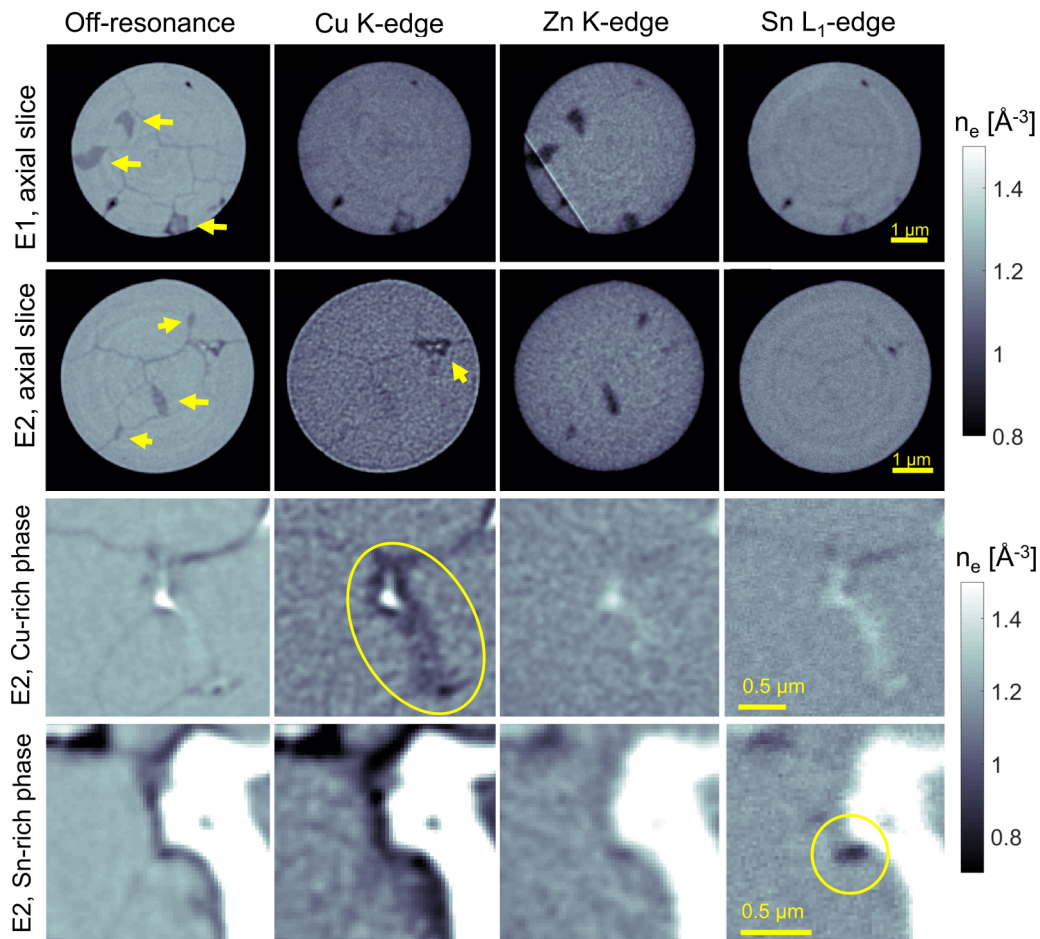


FIG. 4. Chemical features revealed by contrast variation at different energies. Each row reports the same slice or area at the four different energies (columns). ZnS grains (yellow arrows) are found in E1 and E2 (row 1 and 2). Cu- and Sn-rich clusters (circled in yellow) from E2 are highlighted in row 3 and 4, respectively. Colorbars are truncated to enhance gray level contrast.

is evaluated two clusters appear. The larger one relates to CZTS, whereas the smaller one relates to ZnS. If supported

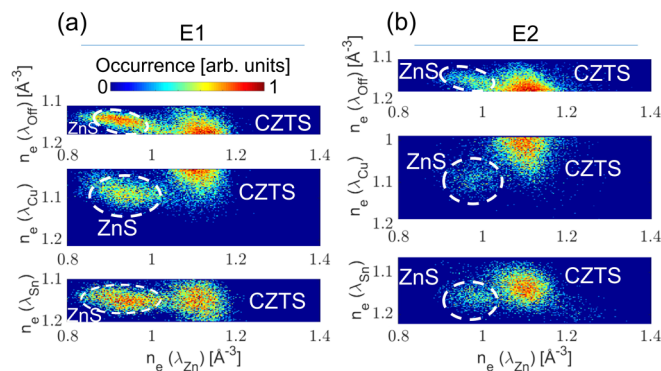


FIG. 5. Bivariate histograms of ZnS in E1 (a) and E2 (b). The apparent electron density at the Zn edge is reported on the x axis vs. the other energies. The active layer of E1 contains significantly larger amounts of ZnS. Clusters in the top row plots are asymmetrical because of the lower dispersion off-resonance. The apparent electron density of ZnS is shifted down to ca.  $0.95 \text{ \AA}^{-3}$  at the Zn-edge. Expected shift values are reported in Table S3 of Supplemental Material [28].

by enough statistics so that they can be clearly identified, the centroids of the ZnS clusters could provide also the information of zero atomic density of Cu and Sn, which can in principle support a more detailed analysis<sup>1</sup> (see subsection Theoretical Basis in METHODS). The continuum of points connecting the ZnS small cluster to the main cluster of CZTS relates to voxels at the grain boundaries, which are better resolved at the off-resonance energy. In this case, the higher detail mixes CZTS with ZnS points and gives the impression that the cluster are better separated with the on-resonance tomograms in spite of their lower quality. Moreover, as Zn is more present in ZnS than in CZTS, the distance between the two clusters' centroids is in fact increased, which corresponds to the desired effect of contrast enhancement. We note that even in the case of E1, where entire grains of ZnS are present, the total volume in the two samples is  $<2.5\%$  of total CZTS volume ( $0.13 \mu\text{m}^3$  ZnS versus  $5.13 \mu\text{m}^3$  CZTS in E1). These levels are below the detection limit for XRD [11].

<sup>1</sup>If ZnS is assumed, then  $n_{\text{at}}^{\text{Cu}} = n_{\text{at}}^{\text{Sn}} = 0$  can be set in the system of Eqs. (3), which becomes in this case overdetermined, having four equations and only two unknowns, allowing for an experimental indirect measurement of the scattering factor corrections.

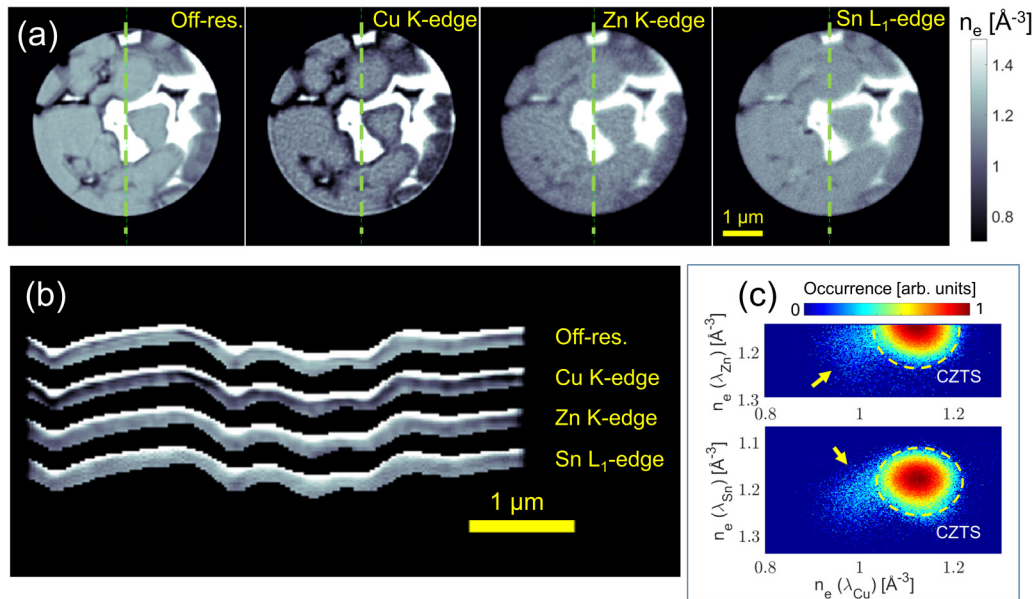


FIG. 6. Images of the CdS/CZTS interface. (a) Axial slice of E2 at the four different energies. The dashed green line refers to the cross section of the segmented interface in (b). The image taken at the Cu K-edge appears darker than the others highlighting Cu migration into the CdS layer. That is illustrated by the trail of points (yellow arrows) around the CZTS cluster in the bivariate histograms of (c). These points show a lower electron density at the Cu edge and similar or higher density at Zn or Sn edge (nominal electron density of CdS is  $1.28 \text{ \AA}^{-3}$ ).

Figure 6 shows the contrast enhancement of the interfacial CdS layer at the Cu K-edge. All the grain boundaries appear thicker from all axial views of previous figures. When segmented, the CdS layer shows lower apparent electron density at the Cu K-edge, highlighting the presence of Cu. The resonant effect of ZnO within this layer is hardly noticeable. From the profile plot of Fig. 3(b), after the kesterite layer, the profile lines would rejoin the off-resonance line if there were no resonant elements, but instead the dip continues for the profile recorded at the Cu edge. Further evidence of the same phenomenon is shown in Fig. S4 of Supplemental Material on a wider stretch of the CdS layer.

Other evident differences are observed at the other resonant energies (Fig. 4). Closer to the interface, some spots are identified where electron density is slightly higher than kesterite off-resonance, while it is decreased at the Cu edge and in the off-resonance absorption-based tomogram. This behavior suggests the presence of CuS or  $\text{Cu}_3\text{SnS}_4$  phases. The lack of these features in other tomograms is consistent with the depicted contrast scenario (cf. Figs. S3 and S5).

### C. Absorption versus phase-based tomograms

Absorption ( $\beta$ )-based tomograms provide valuable redundancy or additional information to the observations from the phase ( $\delta$ ) tomograms, that allows discrimination between different phases of similar electron density. While the phase contrast exhibits a dip around the resonant edge, absorption is increased, implying a substantially different contrast scenario (see Fig. S5 in Supplemental Material [28]). As the quality of absorption-based tomograms is significantly inferior to that of phase tomograms at these energies, both with respect to resolution and to quantitiveness, their information alone is insufficient to reliably discriminate small aggregates of

secondary phases and would yield numerous false positives. Nevertheless, in Fig. 7 the absorption-based tomogram clarifies the picture of the Cu-rich aggregate described in Fig. 4. Since it has lower  $\beta$  values than kesterite, the Cu-rich aggregate cannot be  $\text{Cu}_3\text{SnS}_4$  (cf. Fig. S5) nor CdS with diffused Cu (CdS has approximately double the absorption coefficient of kesterite). The ZnS grains in the two samples can also be identified in the bivariate histograms of absorption versus phase (Fig. S6).

### D. Discussion

Given the important, still unclear role of grain boundaries in kesterite solar cells, the ability to resolve them is crucial. It has been reported that they help charge transport of electrons to the electrode, and secondary phases, not all detrimental, can be found in their proximity [9]. However, Ito's review [2] concludes that results from theoretical [40] and experimental [41] investigations on the role of grain boundaries in kesterites are not fully consistent, but lean toward its benign nature as in CIGS or CdTe devices, rather than a detrimental one like in Si devices. Therefore, we believe the ability to clearly resolve them off-resonance with tomographic methods could have significant impact. It is also shown, however, that grain boundaries still remain a subvoxel feature. Although it would be of interest to compare grain boundaries at different energies, it would be inconclusive on the scale of the achieved experimental resolution.

The single-voxel uncertainty estimated empirically is significantly below the expected 5% uncertainty reference [17] and makes it possible to distinguish most secondary phases only based on a prediction of electron density. Even with a coverage factor of 2 (confidence interval of 95%), the uncertainty is below  $\pm 2\%$  (for details see Sec. II). Based on



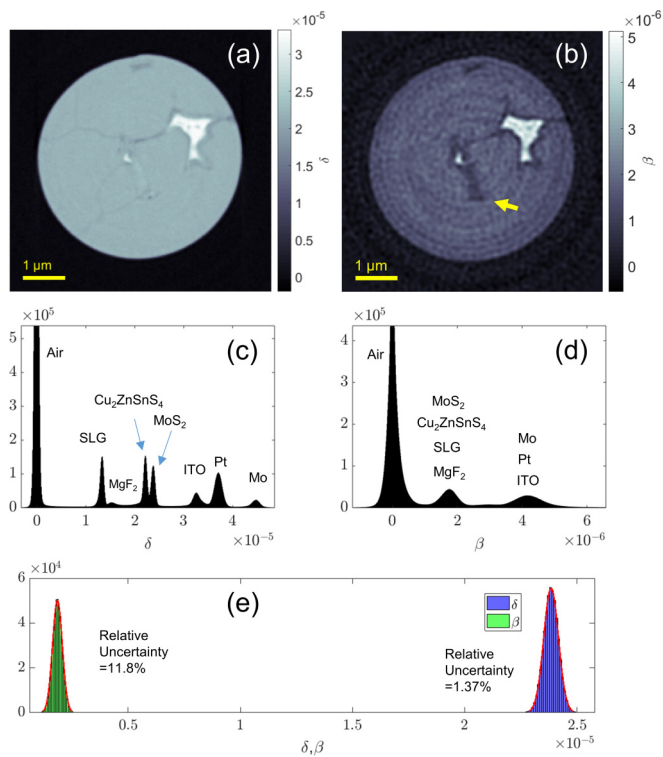


FIG. 7. Top row: comparison of an axial slice of the active layer of E2, phase  $\delta$  (a) vs. absorption  $\beta$  (b) off-resonance tomograms. The slice contains a feature (yellow arrow) illustrated in Fig. 4. In this case the dark feature in the absorption-based tomogram rules out  $\text{Cu}_3\text{SnS}_4$  in favor of  $\text{CuS}$ . The higher contrast of phase tomograms is illustrated by the histogram of occurrences of  $\delta$  (c) and  $\beta$  (d) in the total volume. The dispersion of measured values is small enough for the  $\delta$  to allow high contrast between layers (c), whereas  $\beta$  values are roughly centered around two values only (d). In (e) the dispersion of measured values is quantified on a slice of  $\text{MoS}_2$ . The dispersion of measurement is only slightly higher for  $\delta$  values, which are an order of magnitude higher than  $\beta$ , providing superior relative accuracy.

that,  $\text{Cu}_3\text{SnS}_4$ ,  $\text{Sn}_2\text{S}_3$ , and  $\text{SnS}_2$  are the only phases that do not show sufficient contrast with respect to pure kesterite. However, without elemental sensitivity it is not possible to distinguish a subvoxel porosity (voids, gaps between grains) from lower density inherent to the secondary phases. Unlike the large grains found in E1, a few  $\text{ZnS}$  particles found in E2 are sufficiently small to be mistaken for porous kesterite or voids. In that case, the resonant tomogram at Zn edge provides definitive evidence about their nature. It also occurs that a kesterite grain can fit well within the  $\text{Sn}_2\text{S}_3$  range, and in that case the resonant tomogram at the Cu-edge excludes it.

The biggest defects in the interfacial layer (bubbles with diameter up to ca. 200 nm) are due to the CdS deposition step. These are CdS precipitates arising from the CBD process. Besides, although only a few, some grains are spaced enough from each other to allow CdS to fill this gap (see also Fig. S4). Although this can in principle short-circuit the CdS and  $\text{MoS}_2$  layers, there is no electrical contact between the layers, as an open circuit voltage different than zero has been measured in both cells.

Cu migration into the CdS layer has been reported in literature [42,43], and it has also been argued that Cu has a crucial role in determining the performance of the CdS/kesterite interface [44]. Therefore, it is of interest to quantify our observations with respect to the interface. The lower electron density of the CdS layer can be attributed to subvoxel porosity or in principle to Cu substitution, as Cu is significantly lighter than Cd. The weight of each factor is not easy to estimate, considering that thickness of this layer is barely above the resolution. Porosity alone would imply a value of 8% in E1 and 11% in E2. The amount of Cu could in principle be estimated by Eq. (2) (see Methods), if the scattering factor of Cu were available. The role of Cu in decreasing the electron density is supported by the fact that a lower value is observed concurrently with a higher Cu presence, which is what the comparison between E1 and E2 suggests. As no post-annealing was performed on this cell, Cu migration must have occurred in the CBD step. This same observation is reported by Kim *et al.* [44], who noted a lower performance in a cell with intermixing of interfacial layers, while the reasons for that were unclear.

ZnS presence appeared less sporadic than expected. A grain of similar size as those in E1 (500 nm) was observed in a previous investigation of ours in a sample prepared from the same device. Thus, these ZnS grains, rather than an exception, here appear as the rule. As they can escape quantification and localization with XRD [11], they were not detected in the previous characterization. Moreover, they can qualify as a further responsible for the performance gap previously outlined [24]. The performance gap was attributed to the nonuniformity of the ITO layer, which has also been observed here, but only in one instance. As kesterite is grown in a Zn-rich environment, this finding is not unexpected.

On the contrary, the observation of a  $\text{CuS}$  aggregate was not expected.  $\text{CuS}$  droplets were observed before as a byproduct of the PLD step [24]. These droplets could be removed by KCN-etching, but that was judged as unnecessary, as they seemed to disappear after annealing. It was also previously shown that the appearance of the film changes radically after annealing, and it is assumed that all the excess Cu is absorbed into the kesterite layer. Our findings show that part of it could still form Cu-rich phases other than kesterite. A portion of the aggregate is also compatible with  $\text{Cu}_3\text{SnS}_4$  values, but this option seems to be ruled out by the absorption-based tomograms.

Only two of the Sn-rich phases shown in Fig. 4 have been found in the two samples. They are about 100 nm in size, therefore larger than the assessed resolution, and they are arguably not artifacts as they are systematically obtained in different reconstructions. However, they do not match any of the most likely Sn-rich phases summarized in Table S3. To be identified as  $\text{SnS}_2$  or  $\text{Sn}_2\text{S}_3$ , they would have to show significantly enhanced contrast at Cu energy, which does not appear to be the case. The absorption-based tomograms do not help in this respect because of the small size of the feature. As Sardashti *et al.* have observed  $\text{SnO}_2$  after air annealing [42], this hypothesis has to be considered, but the electron density of  $\text{SnO}_2$ , over  $1.8 \text{ \AA}^{-3}$ , is significantly higher than that of kesterite and would be evident at off-resonance energies. Although very unlikely to form [45], we have to consider

$\text{Cu}_2\text{ZnSn}_3\text{S}_8$  as a possibility as it should have similar resonant behavior as kesterite at all energies except than at the Sn edge. However, the easier interpretation is that of a subvoxel mix of particles rich of  $\text{Sn}_x\text{S}$  with  $1 < x < 2$ , which would explain why nothing is visible off-resonance.

It is unclear whether we can relate our findings on a 5  $\mu\text{m}$ -diameter cylinder to efficiency measurement of the whole tested area. Nonetheless, we note that E1 had higher efficiency than E2 (1.6% versus 0.8%). The overall comparison shows that E1 contains significantly more ZnS, but no Cu- or Sn-rich secondary phases. Besides, it shows less Cu at the interface than E2, a more uniform thickness of the active layer (although smaller grains), and no discontinuity in the CdS/ZnO nor in the ITO layer.

### E. Outlook

The only element of kesterite whose resonant edge has not been probed is S. Sulfur K-edge is around 2.5 keV and is outside of the capabilities of the beamline. However, with our experimental design, it would not provide much new information as all secondary phases are sulphides and the S density contrast is supposedly not higher than the off-resonance electron density contrast. Beamlines that can probe such low energy are typically devoted to soft x-ray techniques, and therefore are unable to probe the energies of Cu and Zn or samples of this size. However, kesterite systems have extensively been studied around the S K-edge with near edge spectroscopy [46,47]. An imaging experiment at the S K-edge could exploit the near edge fine structure provided by different oxidation states of the elements within different phases rather than by atomic densities.

To draw conclusions on the smallest features, one should ideally have the same resolution and accuracy at all energies. Doubling the exposure time has led in the case of the Sn edge to an improvement of quantitiveness and resolution. As kesterite is known for its stability and our samples tolerated a dose of four tomograms, it can be beneficial to increase the exposure time also in the other cases to reduce the dispersion of measurements and allow detection of clusters in bivariate histograms that are even closer than the illustrated cases. It is also useful to point out that there exists a trade-off between resolution and quantitiveness. Defects of bigger size and lower contrast could be highlighted by binning/interpolation. Further increase of quantitiveness is particularly desirable for automatic analysis of data, as it would determine better success rate for segmentation.

Arguably, more interesting observations can be made at interfaces on a scale finer than tens of nanometers, which could be observed with electron microscopy methods. However, these methods limit sample size well below the typical grain size in kesterite. Compared to other synchrotron techniques, RXPT probes a larger scale than XRD but provides real space information, and has superior resolution and accuracy for quantification than 3D fluorescence even in its most advanced correlative version [48]. Elemental sensitivity, which is the main advantage of fluorescence, is obtained in this case for the elements of interest at the cost of a change of energy and

additional scans. Although 3D information can in principle be obtained with fluorescence, tomographic reconstruction might pose major challenges due to self absorption [49] and would not achieve a resolution comparable to RXPT. The most important feature of this technique is the possibility for *in situ* or *operando* studies. The impact of these defects and features can be quantified with measurements of x-ray beam induced current or voltage (XBIC/XBIV [50–52]), which is the natural extension of this study. The missing requirements for such studies are the ability to electrically contact the prepared samples and a different scheme for the ptychographic scan. The first requirement is easily overcome by a laminographic stage [53,54], suitable for planar devices and which does not require milling to micron size. The second requirement is simply met by placing the sample closer to the focus point, so that the measured XBIC/XBIV map can have a resolution closer to the focus size. We foresee this approach to have a massive impact for the characterization of photovoltaic materials, especially with the introduction of fourth-generation synchrotrons.

### IV. CONCLUSIONS

We have used RXPT to image in 3D a full kesterite solar cell on the nanoscale. We demonstrated the capability of the technique to detect not only morphological features, such as grain boundaries, pinholes, thinning of layers, but also chemical features such as migration of Cu into the CdS layer and presence of secondary phases that are not easily detected with conventional techniques. Secondary phases are mapped here thanks to a different contrast mechanism, based on electron density, and to alterations of contrast induced by elemental resonance. Importantly, the ability to discriminate phases is only limited by spatial resolution, i.e., as long as a ZnS particle is larger than 40 nm it can be detected independently of the percentage of the total volume, enabling examination of state-of-the-art rather than defective devices. As the technique enables imaging of morphological and chemical features relevant for performance of solar devices in a nondestructive way, it potentially allows for *in situ* or *operando* studies. In combination with XBIC measurement and a laminographic stage, it can be used to determine the impact of nanoscale defects on the overall performance of solar devices.

### ACKNOWLEDGMENTS

We thank the staff of the Swiss Light Source (SLS) at the Paul Scherrer Institute (PSI) for the support with RXPT experiments. X-ray nanotomography experiments were carried out at the cSAXS beamline, Paul Scherrer Institute, Switzerland. This study was supported by the European Research Council (ERC) under the European Union's Horizon 2020 research and innovation programme (SEEWHI Consolidator Grant No. ERC-2015-CoG-681881) and by the Ministry of Higher Education and Science (DANSCATT Grant No. 7055-00007B). M.V. acknowledges funding from SNSF Grant No. 200021L\_169753. M.V. and A.C. acknowledge financial support from the European Union's Horizon 2020 research and innovation program under the Marie Skłodowska-Curie Grant Agreements No. 701647 (M.V.) and No. 840751 (A.C.).

- [1] S. Giraldo, Z. Jehl, M. Placidi, V. Izquierdo-Roca, A. Pérez-Rodríguez, and E. Saucedo, *Adv. Mater.* **31**, 1806692 (2019).
- [2] K. Ito, *Copper Zinc Tin Sulfide-Based Thin-Film Solar Cells* (John Wiley & Sons Ltd, Chichester, UK, 2014).
- [3] S. K. Wallace, D. B. Mitzi, and A. Walsh, *ACS Energy Lett.* **2**, 776 (2017).
- [4] S. Siebentritt, *Thin Solid Films* **535**, 1 (2013).
- [5] S. Levchenko, J. Just, A. Redinger, G. Larramona, S. Bourdais, G. Dennler, A. Jacob, and T. Unold, *Phys. Rev. Appl.* **5**, 024004 (2016).
- [6] A. Crovetto, A. Cazzaniga, R. B. Ettliger, J. Schou, and O. Hansen, *Sol. Energy Mater. Sol. Cells* **187**, 233 (2018).
- [7] P. D. Antunez, S. Li, D. M. Bishop, D. B. Farmer, T. S. Gershon, J. B. Baxter, and R. Haight, *Appl. Phys. Lett.* **113**, 033903 (2018).
- [8] I. D. Olekseyuk, I. V. Dudchak, and L. V. Piskach, *J. Alloys Compd.* **368**, 135 (2004).
- [9] M. Kumar, A. Dubey, N. Adhikari, S. Venkatesan, and Q. Qiao, *Energy Environ. Sci.* **8**, 3134 (2015).
- [10] A.-J. Cheng, M. Manno, A. Khare, C. Leighton, S. A. Campbell, and E. S. Aydil, *J. Vac. Sci. Technol. A Vacuum Surfaces, Film.* **29**, 051203 (2011).
- [11] D. M. Berg, M. Arasimowicz, R. Djemour, L. Gütay, S. Siebentritt, S. Schorr, X. Fontané, V. Izquierdo-Roca, A. Pérez-Rodríguez, and P. J. Dale, *Thin Solid Films* **569**, 113 (2014).
- [12] X. Fontané, L. Calvo-Barrio, V. Izquierdo-Roca, E. Saucedo, A. Pérez-Rodríguez, J. R. Morante, D. M. Berg, P. J. Dale, and S. Siebentritt, *Appl. Phys. Lett.* **98**, 181905 (2011).
- [13] A. Lafond, L. Choubrac, C. Guillot-Deudon, P. Fertey, M. Evain, and S. Jobic, *Acta Crystallogr. Sect. B Struct. Sci. Cryst. Eng. Mater.* **70**, 390 (2014).
- [14] M. Dierolf, A. Menzel, P. Thibault, P. Schneider, C. M. Kewish, R. Wepf, O. Bunk, and F. Pfeiffer, *Nature* **467**, 436 (2010).
- [15] E. B. L. Pedersen, D. Angmo, H. F. Dam, K. T. S. Thydén, T. R. Andersen, E. T. B. Skjønsgjell, F. C. Krebs, M. Holler, A. Diaz, M. Guizar-Sicairos, D. W. Breiby, and J. W. Andreasen, *Nanoscale* **7**, 13765 (2015).
- [16] H. F. Dam, T. R. Andersen, E. B. L. Pedersen, K. T. S. Thydén, M. Helgesen, J. E. Carlé, P. S. Jørgensen, J. Reinhardt, R. R. Søndergaard, M. Jørgensen, E. Bundgaard, F. C. Krebs, and J. W. Andreasen, *Adv. Energy Mater.* **5**, 1400736 (2015).
- [17] A. Diaz, P. Trtik, M. Guizar-Sicairos, A. Menzel, P. Thibault, and O. Bunk, *Phys. Rev. B* **85**, 020104(R) (2012).
- [18] C. Donnelly, M. Guizar-Sicairos, V. Scagnoli, M. Holler, T. Huthwelker, A. Menzel, I. Vartiainen, E. Müller, E. Kirk, S. Gliga, J. Raabe, and L. J. Heyderman, *Phys. Rev. Lett.* **114**, 115501 (2015).
- [19] J. Ihli, A. Diaz, Y. Shu, M. Guizar-Sicairos, M. Holler, K. Wakonig, M. Odstrcil, T. Li, F. Krumeich, E. Müller, W.-C. Cheng, J. Anton van Bokhoven, and A. Menzel, *J. Phys. Chem. C* **122**, 22920 (2018).
- [20] Y.-S. Yu, M. Farmand, C. Kim, Y. Liu, C. P. Grey, F. C. Strobridge, T. Tylliszczak, R. Celestre, P. Denes, J. Joseph, H. Krishnan, F. R. N. C. N. C. Maia, A. L. D. D. Kilcoyne, S. Marchesini, T. P. C. Leite, T. Warwick, H. Padmore, J. Cabana, and D. A. Shapiro, *Nat. Commun.* **9**, 921 (2018).
- [21] M. Hirose, N. Ishiguro, K. Shimomura, N. Burdet, H. Matsui, M. Tada, and Y. Takahashi, *Angew. Chemie* **130**, 1490 (2018).
- [22] J. Wu, X. Zhu, M. M. West, T. Tylliszczak, H.-W. Shiu, D. Shapiro, V. Berejnov, D. Susac, J. Stumper, and A. P. Hitchcock, *J. Phys. Chem. C* **122**, 11709 (2018).
- [23] J. Wu, X. Zhu, D. A. Shapiro, J. R. I. Lee, T. Van Buuren, M. M. Biener, S. A. Gammon, T. T. Li, T. F. Baumann, and A. P. Hitchcock, *J. Phys. Chem. C* **122**, 25374 (2018).
- [24] A. Cazzaniga, A. Crovetto, C. Yan, K. Sun, X. Hao, J. Ramis Estelrich, S. Canulescu, E. Stamate, N. Pryds, O. Hansen, and J. Schou, *Sol. Energy Mater. Sol. Cells* **166**, 91 (2017).
- [25] G. Hodes, *Chemical Solution Deposition of Semiconductor Films* (CRC Press, Boca Raton, FL, 2002).
- [26] R. M. Langford and C. Clinton, *Micron* **35**, 607 (2004).
- [27] M. Holler, J. Raabe, R. Wepf, S. H. Shahmoradian, A. Diaz, B. Sarafimov, T. Lachat, H. Walther, and M. Vitins, *Rev. Sci. Instrum.* **88**, 113701 (2017).
- [28] See Supplemental Material at <http://link.aps.org/supplemental/10.1103/PhysRevResearch.2.013378> for: SEM images from sample preparation; electrical characterization of devices; resolution assessment through line profiling; electron density of compounds; expected contrast simulations; sagittal chemical view of CdS buffer layer filling; bivariate histogram of absorption-based tomograms; note on radiation damage; movie S1, sagittal slice view of sample E1 (MPG); movie S2, volume rendering of sample E1 (MPG).
- [29] M. Holler, J. Raabe, A. Diaz, M. Guizar-Sicairos, C. Quitmann, A. Menzel, and O. Bunk, *Rev. Sci. Instrum.* **83**, 073703 (2012).
- [30] M. Odstrčil, M. Lebugle, M. Guizar-Sicairos, C. David, and M. Holler, *Opt. Express* **27**, 14981 (2019).
- [31] X. Huang, H. Yan, R. Harder, Y. Hwu, I. K. Robinson, and Y. S. Chu, *Opt. Express* **22**, 12634 (2014).
- [32] P. Thibault, M. Dierolf, A. Menzel, O. Bunk, C. David, and F. Pfeiffer, *Science* **321**, 379 (2008).
- [33] P. Thibault and M. Guizar-Sicairos, *New J. Phys.* **14**, 063004 (2012).
- [34] M. Guizar-Sicairos, A. Diaz, M. Holler, M. S. Lucas, A. Menzel, R. A. Wepf, and O. Bunk, *Opt. Express* **19**, 21345 (2011).
- [35] M. Guizar-Sicairos, J. J. Boon, K. Mader, A. Diaz, A. Menzel, and O. Bunk, *Optica* **2**, 259 (2015).
- [36] M. Van Heel and M. Schatz, *J. Struct. Biol.* **151**, 250 (2005).
- [37] R. P. J. Nieuwenhuizen, K. A. Lidke, M. Bates, D. L. Puig, D. Grünwald, S. Stallinga, and B. Rieger, *Nat. Methods* **10**, 557 (2013).
- [38] S. Sasaki, *Numerical Tables of Anomalous Scattering Factors Calculated by the Cromer and Liberman's Method* (Tsukuba, Japan, 1989).
- [39] M. Guizar-Sicairos, S. T. Thurman, and J. R. Fienup, *Opt. Lett.* **33**, 156 (2008).
- [40] J. Li, D. B. Mitzi, and V. B. Shenoy, *ACS Nano* **5**, 8613 (2011).
- [41] J. B. Li, V. Chawla, and B. M. Clemens, *Adv. Mater.* **24**, 720 (2012).
- [42] K. Sardashti, R. Haight, T. Gokmen, W. Wang, L.-Y. Chang, D. B. Mitzi, and A. C. Kummel, *Adv. Energy Mater.* **5**, 1402180 (2015).
- [43] F. Liu, C. Yan, J. Huang, K. Sun, F. Zhou, J. A. Stride, M. A. Green, and X. Hao, *Adv. Energy Mater.* **6**, 1600706 (2016).
- [44] J. Kim, S. Park, S. Ryu, J. Oh, and B. Shin, *Prog. Photovoltaics Res. Appl.* **25**, 308 (2017).
- [45] E. A. Pogue and A. A. Rockett, in *Conf. Rec. IEEE Photovolt. Spec. Conf.* (IEEE, Piscataway, NJ, 2016), pp. 471–475.

- [46] J. Just, C. M. Sutter-Fella, D. Lützenkirchen-Hecht, R. Frahm, S. Schorr, and T. Unold, *Phys. Chem. Chem. Phys.* **18**, 15988 (2016).
- [47] J. Just, D. Lützenkirchen-Hecht, O. Müller, R. Frahm, and T. Unold, *APL Mater.* **5**, 126106 (2017).
- [48] J. Deng, Y. H. Lo, M. Gallagher-Jones, S. Chen, A. Pryor, Q. Jin, Y. P. Hong, Y. S. G. Nashed, S. Vogt, J. Miao, and C. Jacobsen, *Sci. Adv.* **4**, eaau4548 (2018).
- [49] M. Stuckelberger, B. West, T. Nietzold, B. Lai, J. M. Maser, V. Rose, and M. I. Bertoni, *J. Mater. Res.* **32**, 1825 (2017).
- [50] C. Ossig, T. Nietzold, B. West, M. Bertoni, G. Falkenberg, C. G. Schroer, and M. E. Stuckelberger, *J. Vis. Exp.* **150**, e60001 (2019).
- [51] B. M. West, M. Stuckelberger, H. Guthrey, L. Chen, B. Lai, J. Maser, V. Rose, W. Shafarman, M. Al-Jassim, and M. I. Bertoni, *Nano Energy* **32**, 488 (2017).
- [52] M. E. Stuckelberger, T. Nietzold, B. M. West, B. Lai, J. M. Maser, V. Rose, and M. I. Bertoni, in *2017 IEEE 44th Photovolt. Spec. Conf.* (IEEE, Piscataway, NJ, 2017), pp. 2179–2184.
- [53] M. Holler, M. Odstrcil, M. Guizar-Sicairos, M. Lebugle, E. Müller, S. Finizio, G. Tinti, C. David, J. Zusman, W. Unglaub, O. Bunk, J. Raabe, A. F. J. Levi, and G. Aeppli, *Nat. Electron.* **2**, 464 (2019).
- [54] M. Odstrcil, M. Holler, J. Raabe, and M. Guizar-Sicairos, in *Image Sens. Technol. Mater. Devices, Syst. Appl. V*, edited by N. K. Dhar and A. K. Dutta (SPIE, Bellingham, WA, 2018), p. 28.



## 5.2 Supplemental Material

### 5.2.1 Additional figures and Tables

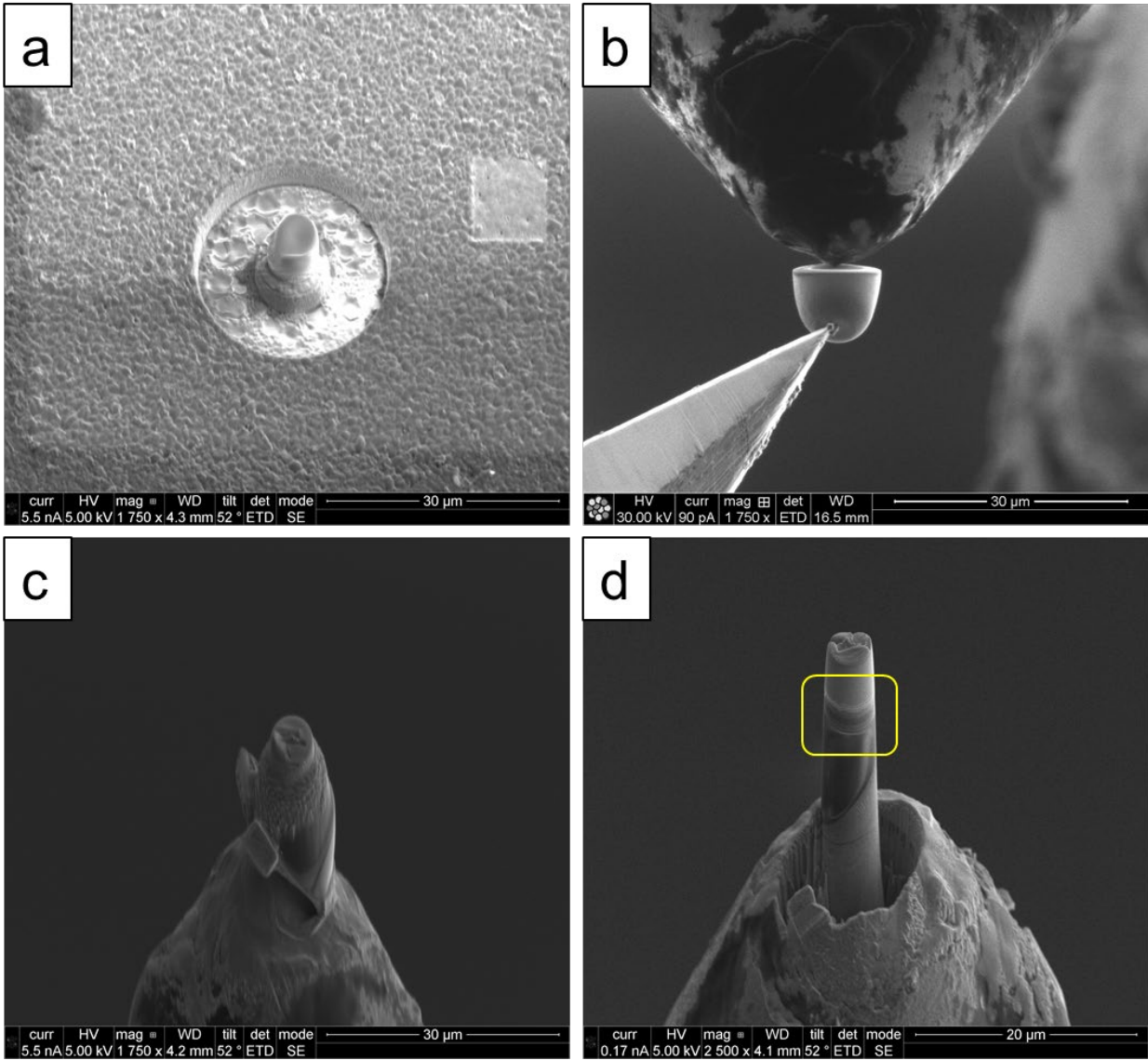


**Figure 5-2. SEM Images of sample preparation for X-ray nanotomography with FIB lift-out. a) a protective layer of Pt is deposited before milling over a round area without apparent defects; b) the sample is cut out of its side and glued on the tip of the OMNY pin; c) the paste gluing the sample to the pin is milled to isolate the prepared sample in d), where the yellow square encloses the region of interest.**



**Table 5-1. Electrical characterization of areas from which the two samples were taken.**

Area	Area [mm <sup>2</sup> ]	Contact area [mm <sup>2</sup> ]	Effective area [mm <sup>2</sup> ]	V <sub>oc</sub> [V]	J <sub>sc</sub> [mA/cm <sup>2</sup> ]	FF [%]	PCE [%]
E1	22,5	4	18,5	0,36	16.55	40	1,641
E2	22,5	2	20,5	0,22	12.3	30	0,833

V<sub>oc</sub>, open circuit voltage; J<sub>sc</sub>, short circuit current density; FF, fill factor; PCE, power conversion efficiency.

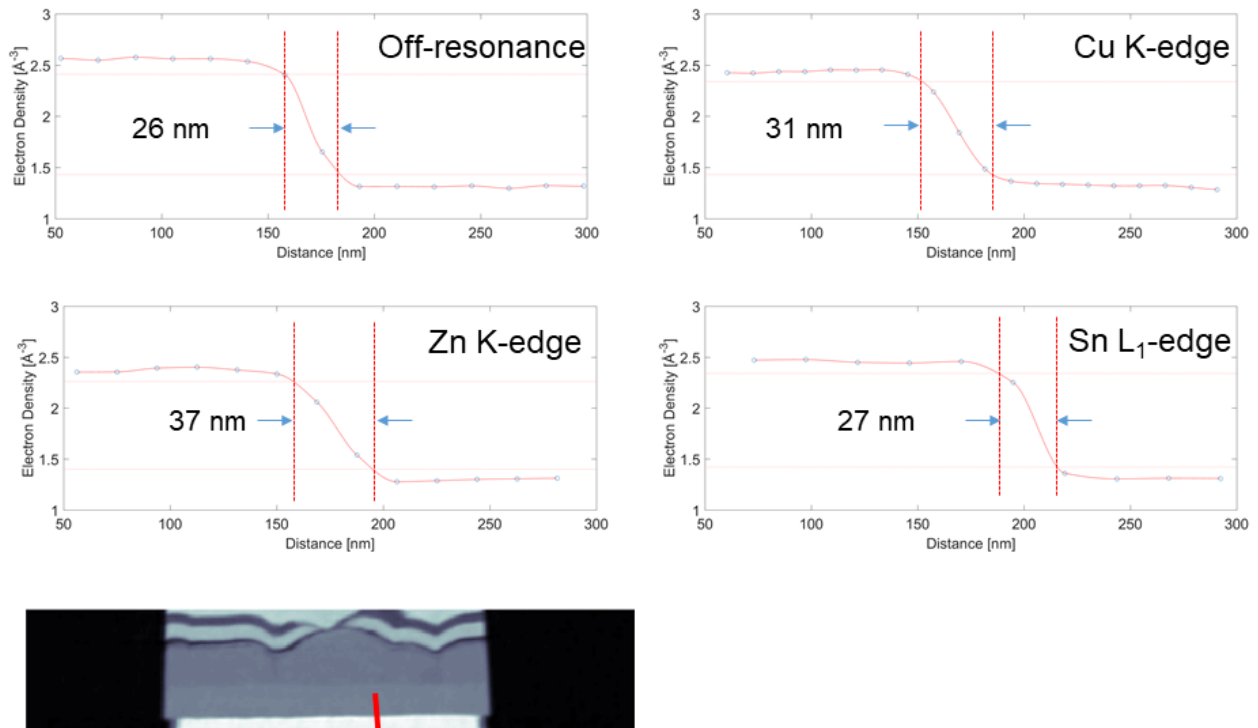


**Figure 5-3. Resolution assessment via edge response measurement. Three lines profile are measured over the red line across the Mo-MoS<sub>2</sub> interface. Such interface is chosen for the higher contrast and uniformity, which make line profiling easier.**

**Table 5-2. Electron density of compounds. Calculated from material properties according to Eq. 5.1.**

Layer	Electron Density [ $\text{\AA}^{-3}$ ]
MoS <sub>2</sub>	1.41
CZTS	1.26
CdS	1.29
ZnO	1.57
ITO	1.91
MgF <sub>2</sub>	0.91

These values of electron density are indicated with  $n_e^*$  and are computed according to the following equation:

$$n_e^* = \frac{\rho N_A N_e}{M}, \quad \mathbf{5.1}$$

where  $\rho$  is the mass density,  $N_A$  is Avogadro constant,  $N_e$  is the number of electrons per formula, and  $M$  is the molar mass.

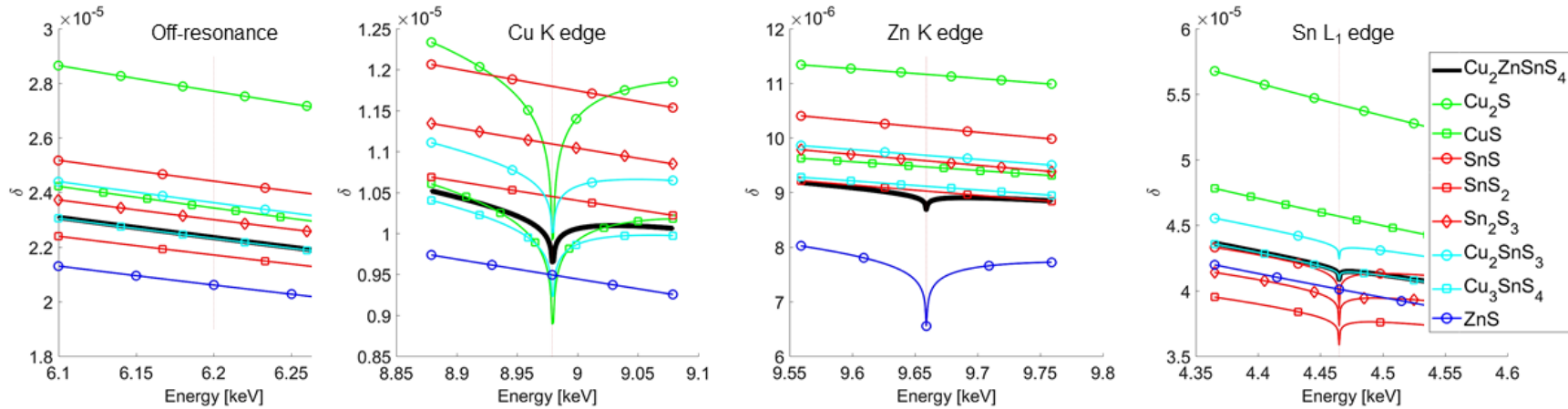


**Figure 5-4. Expected phase contrast simulations. Kesterite is represented by the thick black line, binary and ternary phases in different colors. Sulfides of the same element are represented with a different marker.**

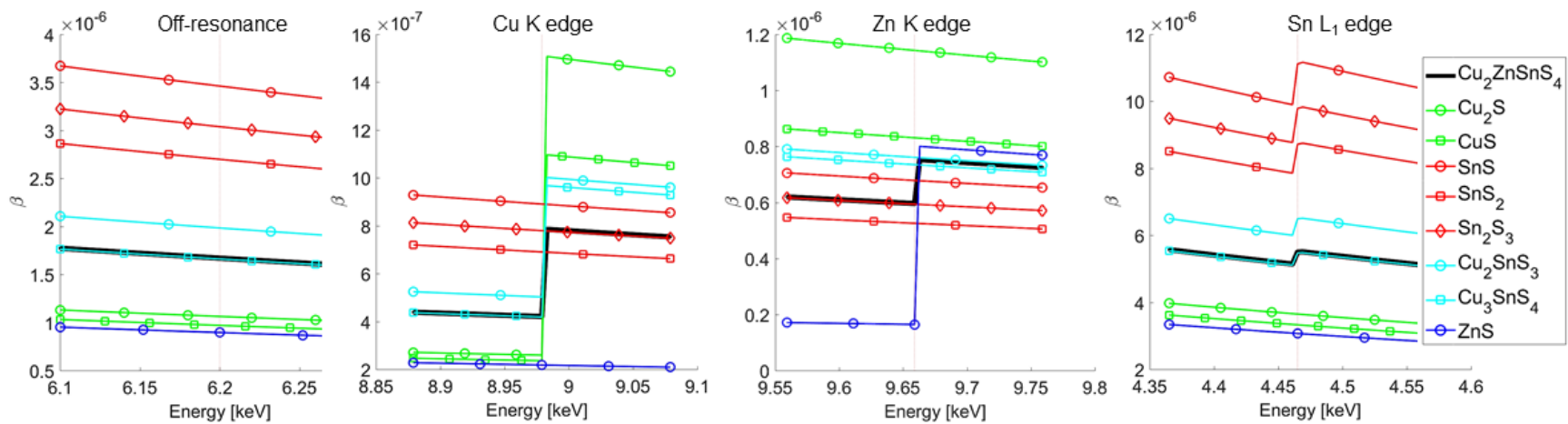


**Figure 5-5. Expected absorption contrast simulations.**

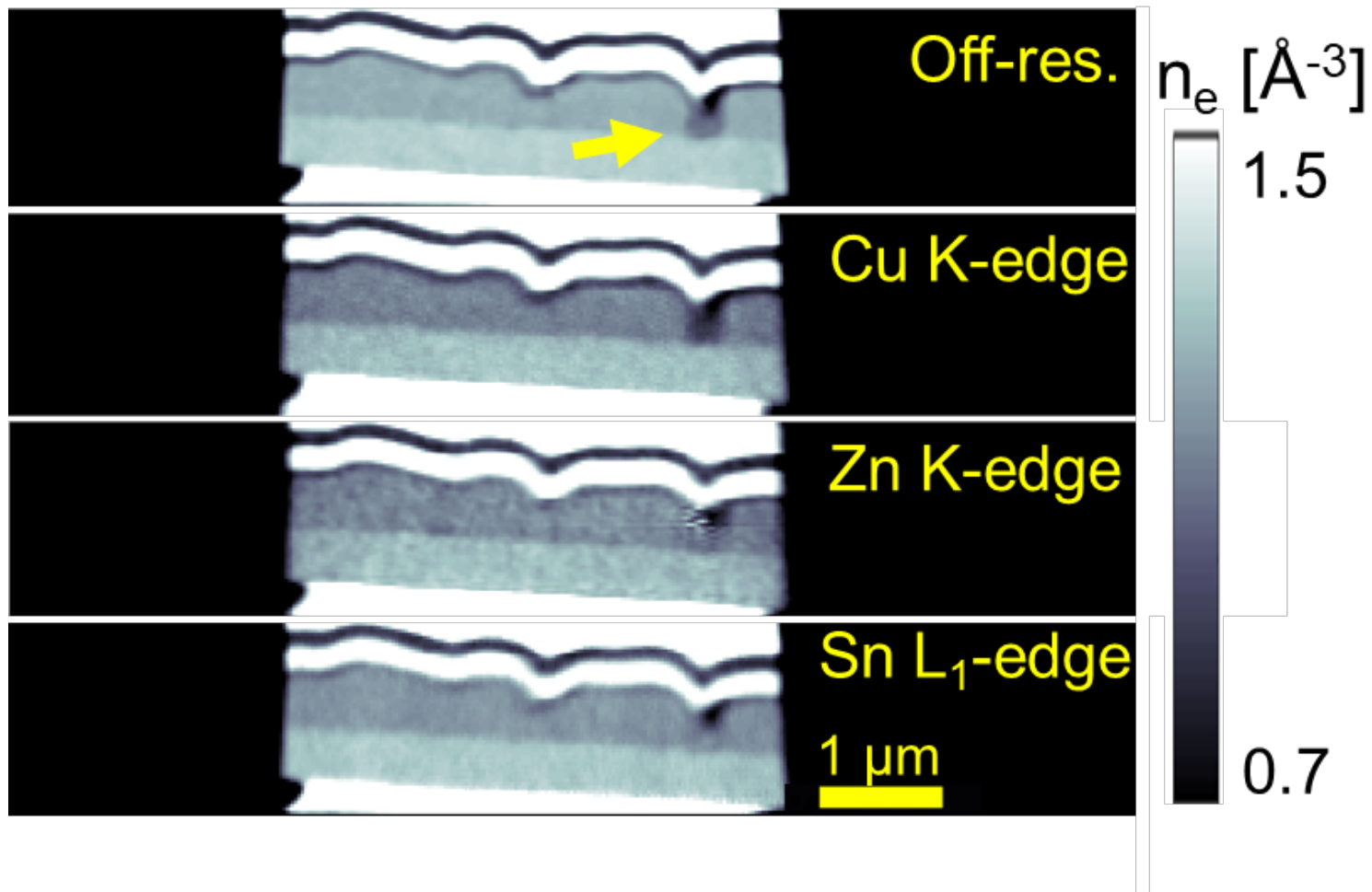
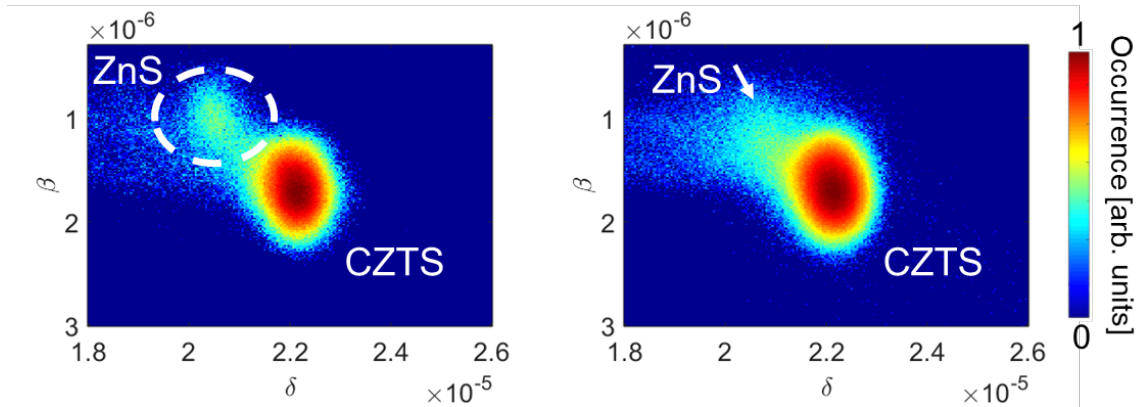


Figure 5-6. CdS filling a wider gap in the CZTS layer. A nonzero open circuit voltage was measured for the cell, which suggests there is still no electrical contact between CdS and MoS. The CdS leak is approximately 300 nm wide and shows increased contrast at Cu edge, even in the lower part. This view also shows that the Cu migration highlighted in previous figures is not misinterpretation of a slow edge-response.



**Figure 5-7. Bivariate histograms of  $\delta$  and  $\beta$  values in the active layer of E1 and E2. The centers of centroids match the expected values of Figure 5-4 and Figure 5-5, however the absorption tomogram alone does not permit to discriminate ZnS from the copper sulfides (cf. Figure 5-4).**

**Table 5-3. Apparent electron density predicted by Eq. 1 (see Methods, article) with empirical atomic scattering factors [157]. Values in grey boxes, are computed without taking into account speciation and fine structure around the edge and can easily differ from measurements.**

Phases	$n_e(\lambda_{\text{off}})$	$n_e(\lambda_{\text{Cu}})$	$n_e(\lambda_{\text{Zn}})$	$n_e(\lambda_{\text{Sn}})$
	[ $\text{\AA}^{-3}$ ]	[ $\text{\AA}^{-3}$ ]	[ $\text{\AA}^{-3}$ ]	[ $\text{\AA}^{-3}$ ]
<b>Cu<sub>2</sub>ZnSnS<sub>4</sub></b>	1.246	1.167	1.201	1.200
<b>Cu<sub>2</sub>S</b>	1.545	1.291	1.511	1.568
<b>CuS</b>	1.307	1.130	1.282	1.321
<b>SnS</b>	1.361	1.380	1.379	1.177
<b>SnS<sub>2</sub></b>	1.211	1.222	1.221	1.079
<b>Sn<sub>2</sub>S<sub>3</sub></b>	1.283	1.297	1.297	1.128
<b>Cu<sub>2</sub>SnS<sub>3</sub></b>	1.317	1.223	1.310	1.250
<b>Cu<sub>3</sub>SnS<sub>4</sub></b>	1.244	1.137	1.234	1.198
<b>ZnS</b>	1.149	1.110	0.989	1.160

### 5.2.2 Note on radiation damage

Radiation damage from synchrotron X-ray beam can result into loss of crystalline structure in inorganic semiconductor material [158] or reduction of SiO<sub>2</sub> [159], or at worst into sample shrinkage and mass loss as in biological samples [160].

In similar experimental conditions as ours, Holler et al. estimate radiation damage in ptychographic tomography by evaluating Fourier ring correlation of two projections at the same angle before and after a ca. 24 hours tomographic scan with 14.6 nm resolution [161]. They show that projections from the same angle before tomography have a sub-pixel correlation, correlation is close to 1 for all frequencies within the pixel size (14.3 nm), and always higher than the 1-bit threshold. Conversely, the threshold is crossed at 16.4 nm when correlating projections from the same angle taken before and after a tomographic scan. They attribute this loss to radiation damage and to drifts of the experimental setup. Their findings suggest that, although inevitable, radiation damage only does not seem to affect significantly features that are slightly bigger than the assessed resolution.

Nonetheless, as we collected multiple tomograms of the same samples, we examined coarse radiation damage such as shrinkage of the sample or of single layers. The absence of this kind of radiation damage cannot be taken for granted, as we did observe sample shrinkage for a cell of another material under similar experimental conditions. However, for our kesterite samples, all the layers and the overall sample size remain the same after each tomographic scan, as shown by the vertical electron density profile of Figure 2b (see article). In addition, within the single tomograms, we have another way to qualitatively assess radiation damage. As implemented at the cSAXS beamline, for tomography, ptychographic projections of the sample are acquired as 8 sub-tomograms, consecutive in time. When assembling the full tomogram, a vertical alignment of the projections by cross-correlation is performed. If the results of alignment are not sorted by angle but by time, radiation damage from the

sample structure appears as a non-constant density profile. None of our tomograms presented inconsistency among projections.

In our study, we have not analyzed fading of diffraction peaks from crystalline material, nor have we measured degradation of electrical performance due to radiation damage, which could highlight radiation damage occurring on a finer scale than our resolution. Indeed, radiation damage is a concern for active devices as changes of electrical properties are much faster than changes in chemical composition [78], and a strategy for *operando* imaging studies is to beat degradation on time when measuring [81]. The strategy is successful with fluorescence imaging and it would be of interest to compare to ptychography as the latter only uses a mostly coherent (lower) flux.





## 6. Conclusions and Outlook

In this project, we have investigated the feasibility and possibilities of synchrotron imaging with respect to state of the art 3<sup>rd</sup> generation solar cell technologies.

The challenges of synchrotron imaging for organic solar cells in particular have motivated a simulation work based on an alternative method. Given its originality within the CDI community, much of our effort was spent on demonstrating that this approach is valid and more or less reliable. We have not found clearly developed arguments for using this approach in existing literature (the importance of the method in non-X-ray context seems to be postulated), but we have illustrated our own. These works demonstrate the validity of the method in generic electromagnetic simulations, with examples and test cases which are not specifically relevant for the X-ray community. In our work we have used test cases of interest in coherent diffractive imaging, and we were able to demonstrate that, although a significant computational effort is required, the results are correct. Correctness was evaluated both with back-propagation and with phase retrieval, with a positive outcome. In its initial design, this study would include simulation of actual solar cells or representative models and on the model of a precise beamline, but it proved hard enough to convince reviewers about the method even with a toy problem, that this task was put aside and only mentioned in outlook. Future work should aim to directly compare wave-propagation and ray tracing simulation of specific samples to experimental data, with a focus on the highest spatial-frequency signal. Even state-of-the-art ultra-high resolution ptychographic tomography is not yet powerful enough to attempt an imaging experiment with good chances of success. We have pointed out the arguments and the literature in that regard. Given the theoretical limit estimated for coherent diffractive imaging, with more brilliant sources, given the present results, we believe there are good prospects to image these organic layers in a near future. The challenges for this goal have been described in this work, i.e. the low contrast between phases, the radiation-

damage, and the small domain size. We have endeavored to tackle these issues by starting an alternative simulation/modelling of the experiment in order to optimize it. Although its performance is not currently better than typical simulation tools, it allows for a comprehensive model of the sample, and of the whole beamline, and we hope it to be explored to provide insight on the best condition to perform an imaging experiment on a specific sample at a specific beamline. On the experimental side, we have proposed to use resonance as a means to enhance contrast between the phases of organic layers. With due differences, a somehow similar approach of chemical imaging through energy filtered TEM, has demonstrated convincing results on the most studied blend of P3HT-PCBM. We have reproduced similar results on a novel blend including a non-fullerene acceptor. These results confirm that also for these materials, the imaged nanorods in the active layer are roughly the same size as in P3HT-PCBM blends, i.e. around 10 nm, and suggest that a similar strategy can prove useful for an X-ray experiment.

For kesterite cells, we have demonstrated the element-specific ultra-high resolution capability of the technique. We have shown that the technique highlights secondary phases that are not easily distinguished by conventional characterization techniques and other important features, such as the grain morphology, moreover on a full functioning device. The potential of the technique has been discussed in the outlook. We have quantified that ptychographic tomography has made a remarkable progress over the years with respect to quantitiveness, and even in conditions of non-optimal flux. Whereas Diaz et al. measured a 5% relative uncertainty on a volume with 43 nm voxels, we have measured 1% on a volume with an even smaller voxel size of 25 nm. Furthermore, we have illustrated a methodology and an analysis approach for multi-energy resonant imaging, which can be applied to nanoscopy in general, to multi-phase samples from any research area.

## 6.1 Outlook

In the way they have been presented in chapters 4 (simulation) and 5 (experiments) the two main contributions are unrelated in their current state. However, McXtrace does include a component (simulation module) allowing to select a given element and retrieving, through a look-up table, the precise scattering factors as a function of energy, which should allow the simulation of resonant X-ray ptychographic tomography.

Another potential application relates to the fact that these materials are direct semiconductors, hence generate considerable photo-absorption per unit of volume. This feature is neglected in the classical contrast simulations used for our work, but might be accounted in a ray tracing simulation assigning this property to the single voxels of a sample.

Besides the possibility for GPU parallelization for McXtrace and McStas, it has been discussed with developers the possibility of opening up to open source graphic libraries such as openCV. Although this is not strictly in line with the efficiency principles according to which McXtrace was designed, and which impose relatively low-level coding, complex applications such as those of coherent diffractive imaging, might benefit from the use of high-level graphic libraries. That would also be beneficial from the GPU-parallelization perspective, as these libraries offer dedicated functions for that purpose.

On the data analysis side, there is possibly a more sophisticated analysis to be done on the RXPT that has only been hinted to in chapter 5, which can aim to determine the atomic density of the single species. On the experimental side, we note that ptychographic methods have currently the highest resolution, and if combined with laminography, they offer an advantageous flexibility between resolution and imaged area, and do not limit sample size to microns. That can possibly enable in situ and operando studies of X-ray-induced current or voltage. On the other side, classic STXM studies can potentially achieve resolution comparable with ptychographic resolution or better, given the significant focus size reduction recently achieved by multilayer Laue lenses. The reported 8 nm is arguably most advantageous for fluorescence or XBIC

experiment, which are based on an STXM setup. Another interesting combination is with 3DXRD, which can potentially allow to discriminate secondary phases and potentially the Cu/Zn disorder based on the Bragg spots. The experimental conditions are arguably quite different, but not incompatible, so that ideally in a laminographic setup, single areas of interest can be imaged after observing other diffraction peaks than those of kesterite.

The demonstrations given so far of synchrotron imaging for solar cells is obviously not an integral part of the fabrication process. The development of a fabrication process relies mostly on characterization techniques that are more easily available, such as TEM, Raman, EDS, XRD, just to name a few. The reason obviously relates to the empirical nature of the fabrication process which requires continuous tuning of specific parameters and entails fabrication of a majority of less successful samples. It is hard to see how the information provided by synchrotron techniques can be integrated in the fabrication process. However, on most beamlines tomography has experienced significant automatization, considerably reducing scan times. Plus, fourth generation synchrotrons, promise a further reduction in data acquisition time. That can in principle enable to acquire data for a batch of samples from the same process providing a more direct feedback on the fabrication process.

As pointed out, synchrotron 3D imaging has a considerable advantage compared to other characterization techniques for in situ or operando studies. It is a non-destructive technique that can probe samples of representative sizes. For organic solar cells, beside the utility cryo-stages, we have speculated that the in situ CDI technique mentioned in section 2.2.2 might be useful both to image the morphology and to track its degradation.



## 7. References

- [1] R. E. Smalley, "Future Global Energy Prosperity: The Terawatt Challenge," *MRS Bull.*, vol. 30, no. 6, pp. 412–417, Jun. 2005.
- [2] V. A. Popovich, W. Verwaal, M. Janssen, I. J. Bennett, and I. M. Richardson, "Application of X-ray computed tomography in silicon solar cells," in *2010 35th IEEE Photovoltaic Specialists Conference*, 2010, pp. 001759–001764.
- [3] G. Margaritondo, Y. Hwu, and G. Tromba, "Synchrotron light : From basics to coherence and coherence-related applications," *Ital. Phys. Soc.*, pp. 25–54, 2003.
- [4] J. Als-Nielsen and D. McMorrow, "X-rays and their interaction with matter," in *Elements of Modern X-ray Physics*, Wiley, 2011, pp. 1–28.
- [5] B. Watts, "Calculation of the Kramers-Kronig transform of X-ray spectra by a piecewise Laurent polynomial method," *Opt. Express*, vol. 22, no. 19, p. 23628, Sep. 2014.
- [6] D. Paganin, *Coherent X-Ray Optics*. Oxford University Press, 2006.
- [7] K. Giewekemeyer, *A study on new approaches in coherent x-ray microscopy of biological specimens*, vol. 5. Göttingen: Göttingen University Press, 2011.
- [8] A. Sakdinawat and D. Attwood, "Nanoscale X-ray imaging," *Nat. Photonics*, vol. 4, no. 12, pp. 840–848, Dec. 2010.
- [9] G. Fevola, E. Bergbäck Knudsen, T. Ramos, D. Carbone, and J. Wenzel Andreasen, "A Monte Carlo ray-tracing simulation of coherent X-ray diffractive imaging," *J. Synchrotron Radiat.*, vol. 27, no. 1, pp. 134–145, Jan. 2020.
- [10] W. Hoppe, "Principles of electron structure research at atomic resolution using conventional electron microscopes for the measurement of amplitudes and phases," *Acta Crystallogr. Sect. A*, vol. 26, no. 4, pp. 414–426, Jul. 1970.
- [11] J. M. Rodenburg and H. M. L. Faulkner, "A phase retrieval algorithm for shifting illumination," *Appl. Phys. Lett.*, vol. 85, no. 20, pp. 4795–4797, 2004.
- [12] H. M. L. Faulkner and J. M. Rodenburg, "Movable Aperture Lensless Transmission Microscopy : A Novel Phase Retrieval Algorithm," no. July, pp. 2–5, 2004.
- [13] P. Thibault, M. Dierolf, A. Menzel, O. Bunk, C. David, and F. Pfeiffer, "High-Resolution Scanning X-ray Diffraction Microscopy," *Science (80-. )*, vol. 321, no. 5887, pp. 379–382, Jul. 2008.
- [14] J. Rodenburg and A. Maiden, "Ptychography," in *Springer Handbook of Microscopy*, P. W. Hawkes and J. C. H. Spence, Eds. Cham: Springer International Publishing, 2019, pp. 2–2.
- [15] C. J. Jacobsen, *X-ray Microscopy*. Cambridge University Press, 2019.



- [16] Y. Jiang *et al.*, “Electron ptychography of 2D materials to deep sub-ångström resolution,” *Nature*, 2018.
- [17] J. Rodenburg, “A record-breaking microscope news-and-views,” *Nature*, vol. 559, no. 7714. Nature Publishing Group, pp. 334–335, 19-Jul-2018.
- [18] G. Zheng, R. Horstmeyer, and C. Yang, “Wide-field, high-resolution Fourier ptychographic microscopy,” *Nat. Photonics*, vol. 7, no. 9, pp. 739–745, Sep. 2013.
- [19] A. Schropp *et al.*, “Hard x-ray nanobeam characterization by coherent diffraction microscopy,” *Appl. Phys. Lett.*, vol. 96, no. 9, p. 091102, Mar. 2010.
- [20] J. Vila-Comamala *et al.*, “Characterization of high-resolution diffractive X-ray optics by ptychographic coherent diffractive imaging,” *Opt. Express*, vol. 19, no. 22, p. 21333, Oct. 2011.
- [21] C. M. Kewish *et al.*, “Reconstruction of an astigmatic hard X-ray beam and alignment of K-B mirrors from ptychographic coherent diffraction data,” *Opt. Express*, vol. 18, no. 22, p. 23420, Oct. 2010.
- [22] M. Stockmar *et al.*, “Near-field ptychography: Phase retrieval for inline holography using a structured illumination,” *Sci. Rep.*, vol. 3, pp. 1–6, 2013.
- [23] M. Stockmar *et al.*, “X-ray nanotomography using near-field ptychography,” *Opt. Express*, vol. 23, no. 10, p. 12720, 2015.
- [24] M. Stockmar *et al.*, “X-ray near-field ptychography for optically thick specimens,” *Phys. Rev. Appl.*, vol. 3, no. 1, pp. 1–6, Jan. 2015.
- [25] E. H. R. Tsai, I. Usov, A. Diaz, A. Menzel, and M. Guizar-Sicairos, “X-ray ptychography with extended depth of field,” *Opt. Express*, vol. 24, no. 25, p. 29089, 2016.
- [26] A. M. Maiden, M. J. Humphry, and J. M. Rodenburg, “Ptychographic transmission microscopy in three dimensions using a multi-slice approach,” *J. Opt. Soc. Am. A*, vol. 29, no. 8, p. 1606, Aug. 2012.
- [27] P. Li and A. Maiden, “Multi-slice ptychographic tomography,” *Sci. Rep.*, vol. 8, no. 1, p. 2049, Dec. 2018.
- [28] C. Jacobsen, “Relaxation of the Crowther criterion in multislice tomography,” *Opt. Lett.*, vol. 43, no. 19, p. 4811, Oct. 2018.
- [29] A. M. Maiden and J. M. Rodenburg, “An improved ptychographical phase retrieval algorithm for diffractive imaging,” *Ultramicroscopy*, vol. 109, no. 10, pp. 1256–1262, 2009.
- [30] P. Thibault, M. Dierolf, O. Bunk, A. Menzel, and F. Pfeiffer, “Probe retrieval in ptychographic coherent diffractive imaging,” *Ultramicroscopy*, vol. 109, no. 4, pp. 338–343, 2009.
- [31] D. R. Luke, “Relaxed averaged alternating reflections for diffraction imaging,” *Inverse Probl.*, vol. 21, no. 1, pp. 37–50, Feb. 2005.
- [32] R. Hesse, D. Russell Luke, S. Sabach, and M. K. Tam, “Proximal heterogeneous block implicit-explicit method and application to blind ptychographic diffraction imaging,” *SIAM J. Imaging Sci.*, vol. 8, no. 1, pp. 426–457, Feb. 2015.
- [33] P. Thibault and A. Menzel, “Reconstructing state mixtures from diffraction measurements,” *Nature*, vol. 494, no. 7435, pp. 68–71, 2013.

- [34] B. Enders, M. Dierolf, P. Cloetens, M. Stockmar, F. Pfeiffer, and P. Thibault, "Ptychography with broad-bandwidth radiation," *Appl. Phys. Lett.*, vol. 104, no. 17, p. 171104, Apr. 2014.
- [35] N. Burdet *et al.*, "Evaluation of partial coherence correction in X-ray ptychography," *Opt. Express*, vol. 23, no. 5, p. 5452, Mar. 2015.
- [36] O. Bunk, M. Dierolf, S. Kynde, I. Johnson, O. Marti, and F. Pfeiffer, "Influence of the overlap parameter on the convergence of the ptychographical iterative engine," *Ultramicroscopy*, vol. 108, no. 5, pp. 481–487, Apr. 2008.
- [37] T. B. Edo *et al.*, "Sampling in x-ray ptychography," *Phys. Rev. A - At. Mol. Opt. Phys.*, vol. 87, no. 5, 2013.
- [38] D. J. Batey *et al.*, "Reciprocal-space up-sampling from real-space oversampling in x-ray ptychography," *Phys. Rev. A - At. Mol. Opt. Phys.*, vol. 89, no. 4, pp. 1–5, 2014.
- [39] X. Huang, H. Yan, R. Harder, Y. Hwu, I. K. Robinson, and Y. S. Chu, "Optimization of overlap uniformness for ptychography," *Opt. Express*, vol. 22, no. 10, p. 12634, May 2014.
- [40] M. Guizar-Sicairos, M. Holler, A. Diaz, J. Vila-Comamala, O. Bunk, and A. Menzel, "Role of the illumination spatial-frequency spectrum for ptychography," *Phys. Rev. B*, vol. 86, no. 10, p. 100103, Sep. 2012.
- [41] M. Odrščil, M. Lebugle, M. Guizar-Sicairos, C. David, and M. Holler, "Towards optimized illumination for high-resolution ptychography," *Opt. Express*, vol. 27, no. 10, p. 14981, May 2019.
- [42] D. J. Batey, D. Claus, and J. M. Rodenburg, "Information multiplexing in ptychography," *Ultramicroscopy*, vol. 138, pp. 13–21, Mar. 2014.
- [43] Y. H. Lo *et al.*, "In situ coherent diffractive imaging," *Nat. Commun.*, vol. 9, no. 1, pp. 1–10, 2018.
- [44] P. M. Pelz, M. Guizar-Sicairos, P. Thibault, I. Johnson, M. Holler, and A. Menzel, "On-the-fly scans for X-ray ptychography," *Appl. Phys. Lett.*, vol. 105, no. 25, 2014.
- [45] M. Odrščil, M. Holler, M. Guizar-Sicairos, M. I. H. Oller, and G. U. Icairos, "Arbitrary-path fly-scan ptychography," *Opt. Express*, vol. 26, no. 10, pp. 12585–12593, May 2018.
- [46] J. Deng *et al.*, "The Velociprobe: An ultrafast hard X-ray nanoprobe for high-resolution ptychographic imaging," *Rev. Sci. Instrum.*, vol. 90, no. 8, p. 083701, Aug. 2019.
- [47] Z. Yuan, H. Wang, and Q. Wang, "Phase retrieval via Sparse Wirtinger Flow," *J. Comput. Appl. Math.*, vol. 355, pp. 162–173, Aug. 2019.
- [48] M. A. Iwen, A. Viswanathan, and Y. Wang, "Fast phase retrieval from local correlation measurements," *SIAM J. Imaging Sci.*, vol. 9, no. 4, pp. 1655–1688, Oct. 2016.
- [49] N. Sissouno *et al.*, "A direct solver for the phase retrieval problem in ptychographic imaging," *Math. Comput. Simul.*, Nov. 2019.
- [50] E. J. Candès, T. Strohmer, and V. Voroninski, "PhaseLift: Exact and Stable Signal Recovery from Magnitude Measurements via Convex Programming," *Commun. Pure Appl. Math.*, vol. 66, no. 8, pp. 1241–1274, Aug. 2013.

- [51] R. H. T. Rodenburg, J.M.; Bates, “The theory of super-resolution electron microscopy via Wigner-distribution deconvolution,” *Philos. Trans. R. Soc. London. Ser. A Phys. Eng. Sci.*, vol. 339, no. 1655, pp. 521–553, Jun. 1992.
- [52] H. N. Chapman, “Phase-retrieval X-ray microscopy by Wigner-distribution deconvolution,” *Ultramicroscopy*, vol. 66, no. 3–4, pp. 153–172, 1996.
- [53] H. Chang *et al.*, “Advanced denoising for X-ray ptychography,” 2019.
- [54] P. Thibault and M. Guizar-Sicairos, “Maximum-likelihood refinement for coherent diffractive imaging,” *New J. Phys.*, vol. 14, no. 6, p. 063004, Jun. 2012.
- [55] P. Godard, M. Allain, V. Chamard, and J. Rodenburg, “Noise models for low counting rate coherent diffraction imaging,” *Opt. Express*, vol. 20, no. 23, p. 25914, Nov. 2012.
- [56] M. Odstrčil, A. Menzel, and M. Guizar-Sicairos, “Iterative least-squares solver for generalized maximum-likelihood ptychography,” *Opt. Express*, vol. 26, no. 3, p. 3108, Feb. 2018.
- [57] J. Als-Nielsen and D. McMorrow, “Resonant scattering,” in *Elements of Modern X-ray Physics*, Hoboken, NJ, USA: Wiley, 2011, pp. 275–303.
- [58] C. Song *et al.*, “Nanoscale imaging of buried structures with elemental specificity using resonant X-ray diffraction microscopy,” *Phys. Rev. Lett.*, vol. 100, no. 2, pp. 18–21, 2008.
- [59] D. A. Shapiro *et al.*, “Chemical composition mapping with nanometre resolution by soft X-ray microscopy,” *Nat. Photonics*, vol. 8, no. 10, pp. 765–769, Oct. 2014.
- [60] M. Beckers *et al.*, “Chemical contrast in soft X-ray ptychography,” *Phys. Rev. Lett.*, vol. 107, no. 20, pp. 1–4, 2011.
- [61] R. Hoppe *et al.*, “High-resolution chemical imaging of gold nanoparticles using hard x-ray ptychography,” *Appl. Phys. Lett.*, vol. 102, no. 20, p. 203104, May 2013.
- [62] J. Reinhardt *et al.*, “Hard X-ray Resonant Ptychography for Chemical Imaging at the Sensitivity Limit,” *Microsc. Microanal.*, vol. 24, no. S2, pp. 28–29, Aug. 2018.
- [63] M. Hirose, K. Shimomura, N. Burdet, and Y. Takahashi, “Use of Kramers–Kronig relation in phase retrieval calculation in X-ray spectro-ptychography,” *Opt. Express*, vol. 25, no. 8, p. 8593, Apr. 2017.
- [64] C. Donnelly *et al.*, “High-resolution hard x-ray magnetic imaging with dichroic ptychography,” *Phys. Rev. B*, vol. 94, no. 6, pp. 1–9, 2016.
- [65] C. Donnelly *et al.*, “Three-dimensional magnetization structures revealed with X-ray vector nanotomography,” *Nature*, vol. 547, no. 7663, pp. 328–331, 2017.
- [66] C. Donnelly *et al.*, “Element-Specific X-Ray Phase Tomography of 3D Structures at the Nanoscale,” *Phys. Rev. Lett.*, vol. 114, no. 11, p. 115501, Mar. 2015.
- [67] J. Wu *et al.*, “High-Resolution Imaging of Polymer Electrolyte Membrane Fuel Cell Cathode Layers by Soft X-ray Spectro-Ptychography,” *J. Phys. Chem. C*, vol. 122, no. 22, pp. 11709–11719, Jun. 2018.
- [68] M. Hirose *et al.*, “Visualization of Heterogeneous Oxygen Storage

- Behavior in Platinum-Supported Cerium-Zirconium Oxide Three-Way Catalyst Particles by Hard X-ray Spectro-Ptychography,” *Angew. Chemie*, vol. 130, no. 6, pp. 1490–1495, Feb. 2018.
- [69] J. Wu *et al.*, “Four-Dimensional Imaging of ZnO-Coated Alumina Aerogels by Scanning Transmission X-ray Microscopy and Ptychographic Tomography,” *J. Phys. Chem. C*, vol. 122, no. 44, pp. 25374–25385, Nov. 2018.
- [70] A. C. Kak and M. Slaney, *Principles of Computerized Tomographic Imaging*. Society for Industrial and Applied Mathematics, 2001.
- [71] R. A. Crowther, D. J. DeRosier, and A. Klug, “The Reconstruction of a Three-Dimensional Structure from Projections and its Application to Electron Microscopy,” *Proc. R. Soc. A Math. Phys. Eng. Sci.*, vol. 317, no. 1530, pp. 319–340, 1970.
- [72] H. N. Chapman *et al.*, “High-resolution ab initio three-dimensional x-ray diffraction microscopy,” *J. Opt. Soc. Am. A*, vol. 23, no. 5, p. 1179, May 2006.
- [73] D. Gürsoy, “Direct coupling of tomography and ptychography,” *Opt. Lett.*, vol. 42, no. 16, p. 3169, Aug. 2017.
- [74] T. Ramos, B. E. Grønager, M. S. Andersen, and J. W. Andreasen, “Direct three-dimensional tomographic reconstruction and phase retrieval of far-field coherent diffraction patterns,” *Phys. Rev. A*, vol. 99, no. 2, p. 023801, Feb. 2019.
- [75] M. Kahnt *et al.*, “Coupled ptychography and tomography algorithm improves reconstruction of experimental data,” *Optica*, vol. 6, no. 10, p. 1282, Oct. 2019.
- [76] S. Aslan, V. Nikitin, D. J. Ching, T. Bicer, S. Leyffer, and D. Gürsoy, “Joint ptycho-tomography reconstruction through alternating direction method of multipliers,” *Opt. Express*, vol. 27, no. 6, p. 9128, Mar. 2019.
- [77] J. Baró, J. Sempau, J. M. Fernández-Varea, and F. Salvat, “PENELOPE: An algorithm for Monte Carlo simulation of the penetration and energy loss of electrons and positrons in matter,” *Nucl. Inst. Methods Phys. Res. B*, vol. 100, no. 1, pp. 31–46, May 1995.
- [78] M. Stuckelberger *et al.*, “Engineering solar cells based on correlative X-ray microscopy,” *J. Mater. Res.*, vol. 32, no. 10, pp. 1825–1854, May 2017.
- [79] M. I. Bertoni *et al.*, “Grain engineering: How nanoscale inhomogeneities can control charge collection in solar cells,” *Nano Energy*, vol. 32, no. November 2016, pp. 488–493, Feb. 2017.
- [80] M. Stuckelberger *et al.*, “Charge Collection in Hybrid Perovskite Solar Cells: Relation to the Nanoscale Elemental Distribution,” *IEEE J. Photovoltaics*, vol. 7, no. 2, pp. 590–597, Mar. 2017.
- [81] C. Ossig *et al.*, “X-ray Beam Induced Current Measurements for Multi-Modal X-ray Microscopy of Solar Cells,” *J. Vis. Exp.*, vol. 150, no. 150, p. e60001, Aug. 2019.
- [82] M. V. Grigoriev, R. R. Fakhrtdinov, D. V. Irzhak, D. V. Roshchupkin, and E. B. Yakimov, “XBIC using a laboratory X-ray source,” *Bull. Russ. Acad. Sci. Phys.*, vol. 77, no. 1, pp. 26–28, 2013.

- [83] M. V. Grigoriev, D. V. Roshchupkin, R. R. Fakhrtidinov, and E. B. Yakimov, "Studying stacking faults in SiC by the XBIC method using a laboratory X-ray source," *J. Surf. Investig. X-ray, Synchrotron Neutron Tech.*, vol. 8, no. 1, pp. 155–157, 2014.
- [84] M. E. Stuckelberger *et al.*, "X-Ray Beam Induced Voltage: A Novel Technique for Electrical Nanocharacterization of Solar Cells," in *2017 IEEE 44th Photovoltaic Specialist Conference (PVSC)*, 2017, no. January, pp. 2179–2184.
- [85] L. Helfen *et al.*, "Synchrotron-radiation computed laminography for high-resolution three-dimensional imaging of flat devices," *Phys. status solidi*, vol. 204, no. 8, pp. 2760–2765, Aug. 2007.
- [86] L. Helfen *et al.*, "On the implementation of computed laminography using synchrotron radiation," *Rev. Sci. Instrum.*, vol. 82, no. 6, Jun. 2011.
- [87] F. Xu, L. Helfen, T. Baumbach, and H. Suhonen, "Comparison of image quality in computed laminography and tomography," *Opt. Express*, vol. 20, no. 2, p. 794, Jan. 2012.
- [88] S. L. Fisher *et al.*, "Laminography in the lab: imaging planar objects using a conventional x-ray CT scanner," *Meas. Sci. Technol.*, vol. 30, no. 3, p. 035401, Mar. 2019.
- [89] L. Helfen, F. Xu, H. Suhonen, P. Cloetens, and T. Baumbach, "Laminographic imaging using synchrotron radiation – challenges and opportunities," *J. Phys. Conf. Ser.*, vol. 425, no. 19, p. 192025, Mar. 2013.
- [90] M. Holler *et al.*, "Three-dimensional imaging of integrated circuits with macro- to nanoscale zoom," *Nat. Electron.*, vol. 2, no. 10, pp. 464–470, Oct. 2019.
- [91] P. Kirkpatrick and A. V. Baez, "Formation of Optical Images by X-Rays," *J. Opt. Soc. Am.*, vol. 38, no. 9, p. 766, Sep. 1948.
- [92] J. Stangl, C. Mocuta, V. Chamard, and D. Carbone, "X-Ray Focusing Elements Characterization," in *Nanobeam X-Ray Scattering*, Weinheim, Germany: Wiley-VCH Verlag GmbH & Co. KGaA, 2013, pp. 39–87.
- [93] R. Conley *et al.*, "Multilayer Laue Lens: A Brief History and Current Status," *Synchrotron Radiat. News*, vol. 29, no. 4, pp. 16–20, Jul. 2016.
- [94] S. Bajt *et al.*, "X-ray focusing with efficient high-NA multilayer Laue lenses," *Light Sci. Appl.*, vol. 7, no. 3, pp. 17162–17162, Mar. 2018.
- [95] K. T. Murray *et al.*, "Multilayer Laue lenses at high X-ray energies: performance and applications," *Opt. Express*, vol. 27, no. 5, p. 7120, Mar. 2019.
- [96] A. Kubec *et al.*, "Point focusing with flat and wedged crossed multilayer Laue lenses," *J. Synchrotron Radiat.*, vol. 24, no. 2, pp. 413–421, Mar. 2017.
- [97] J. Demmerle, E. Wegel, L. Schermelleh, and I. M. Dobbie, "Assessing resolution in super-resolution imaging," *Methods*, vol. 88, pp. 3–10, 2015.
- [98] A. Diaz, P. Trtik, M. Guizar-Sicairos, A. Menzel, P. Thibault, and O. Bunk, "Quantitative x-ray phase nanotomography," *Phys. Rev. B*, vol. 85, no. 2, p. 020104, Jan. 2012.
- [99] N. Espinosa, M. Hösel, D. Angmo, and F. C. Krebs, "Solar cells with one-day energy payback for the factories of the future," *Energy Environ. Sci.*,

- vol. 5, no. 1, pp. 5117–5132, Jan. 2012.
- [100] A. C. Mayer, S. R. Scully, B. E. Hardin, M. W. Rowell, and M. D. McGehee, “Polymer-based solar cells,” *Mater. Today*, vol. 10, no. 11, pp. 28–33, 2007.
- [101] R. Søndergaard, M. Hösel, D. Angmo, T. T. Larsen-Olsen, and F. C. Krebs, “Roll-to-roll fabrication of polymer solar cells,” *Materials Today*, vol. 15, no. 1–2. Elsevier, pp. 36–49, 01-Jan-2012.
- [102] Y. Lin *et al.*, “17% Efficient Organic Solar Cells Based on Liquid Exfoliated WS<sub>2</sub> as a Replacement for PEDOT:PSS,” *Adv. Mater.*, vol. 31, no. 46, p. 1902965, Nov. 2019.
- [103] P. W. M. Blom, V. D. Mihailesti, L. J. A. Koster, and D. E. Markov, “Device Physics of Polymer:Fullerene Bulk Heterojunction Solar Cells,” *Adv. Mater.*, vol. 19, no. 12, pp. 1551–1566, Jun. 2007.
- [104] G. Yu and A. J. Heeger, “Charge separation and photovoltaic conversion in polymer composites with internal donor/acceptor heterojunctions,” *J. Appl. Phys.*, vol. 78, no. 7, pp. 4510–4515, Oct. 1995.
- [105] G. Yu, J. Gao, J. C. Hummelen, F. Wudl, and A. J. Heeger, “Polymer Photovoltaic Cells: Enhanced Efficiencies via a Network of Internal Donor-Acceptor Heterojunctions,” *Science (80-. )*, vol. 270, no. 5243, pp. 1789–1791, Dec. 1995.
- [106] M. C. Scharber and N. S. Sariciftci, “Efficiency of bulk-heterojunction organic solar cells,” *Prog. Polym. Sci.*, vol. 38, no. 12, pp. 1929–1940, Dec. 2013.
- [107] H. Hoppe, N.S. Sariciftci, “Morphology of polymer/fullerene bulk heterojunction solar cells,” *J. Mater. Chem.*, vol. 16, pp. 45–61, 2006.
- [108] M. C. Scharber and N. S. Sariciftci, “Efficiency of bulk-heterojunction organic solar cells,” *Prog. Polym. Sci.*, vol. 38, no. 12, pp. 1929–1940, Dec. 2013.
- [109] X. Yang and J. Loos, “Toward High-Performance Polymer Solar Cells: The Importance of Morphology Control,” *Macromolecules*, vol. 40, no. 5, pp. 1353–1362, Mar. 2007.
- [110] S. Van Bavel, S. Veenstra, and J. Loos, “On the importance of morphology control in polymer solar cells,” *Macromol. Rapid Commun.*, vol. 31, no. 21, pp. 1835–1845, 2010.
- [111] F. Zhao, C. Wang, and X. Zhan, “Morphology Control in Organic Solar Cells,” *Adv. Energy Mater.*, vol. 8, no. 28, p. 1703147, Oct. 2018.
- [112] H. F. Dam *et al.*, “Enabling Flexible Polymer Tandem Solar Cells by 3D Ptychographic Imaging,” *Adv. Energy Mater.*, vol. 5, no. 1, p. 1400736, Jan. 2015.
- [113] E. B. L. Pedersen *et al.*, “Improving organic tandem solar cells based on water-processed nanoparticles by quantitative 3D nanoimaging,” *Nanoscale*, vol. 7, no. 32, pp. 13765–13774, 2015.
- [114] M. R. Howells *et al.*, “An assessment of the resolution limitation due to radiation-damage in X-ray diffraction microscopy,” *J. Electron Spectros. Relat. Phenomena*, vol. 170, no. 1–3, pp. 4–12, 2009.
- [115] A. Rose, “A Unified Approach to the Performance of Photographic Film, Television Pickup Tubes, and the Human Eye,” *J. Soc. Motion Pict. Eng.*,

- vol. 47, no. 4, pp. 273–294, Oct. 1946.
- [116] M. Odstrčil, “Coherent diffractive imaging using table-top sources,” University of Southampton, University Library, 2017.
- [117] A. S. Gertsen, M. F. Castro, R. R. Søndergaard, and J. W. Andreasen, “Scalable fabrication of organic solar cells based on non-fullerene acceptors,” *Flex. Print. Electron.*, vol. 5, no. 1, p. 014004, Jan. 2020.
- [118] Y. Huang, E. J. Kramer, A. J. Heeger, and G. C. Bazan, “Bulk Heterojunction Solar Cells: Morphology and Performance Relationships,” 2014.
- [119] Y. Moritomo *et al.*, “Fullerene mixing effect on carrier formation in bulk-hetero organic solar cell,” *Sci. Rep.*, vol. 5, no. 1, p. 9483, Aug. 2015.
- [120] S. V. Kesava *et al.*, “Domain Compositions and Fullerene Aggregation Govern Charge Photogeneration in Polymer/Fullerene Solar Cells,” *Adv. Energy Mater.*, vol. 4, no. 11, p. 1400116, Aug. 2014.
- [121] N. Van den Brande *et al.*, “Probing the bulk heterojunction morphology in thermally annealed active layers for polymer solar cells,” *Org. Electron.*, vol. 41, pp. 319–326, Feb. 2017.
- [122] N. Patil *et al.*, “X-Ray Nanoscopy of a Bulk Heterojunction,” *PLoS One*, vol. 11, no. 7, p. e0158345, Jul. 2016.
- [123] K. Giewekemeyer *et al.*, “Quantitative biological imaging by ptychographic x-ray diffraction microscopy,” *Proc. Natl. Acad. Sci.*, vol. 107, no. 2, pp. 529–534, 2010.
- [124] H. Ade, X. Zhang, S. Cameron, C. Costello, J. Kirz, and S. Williams, “Chemical contrast in x-ray microscopy and spatially resolved XANES spectroscopy of organic specimens,” *Science (80-. )*, vol. 258, no. 5084, pp. 972–975, Nov. 1992.
- [125] V. Savikhin, D. A. Shapiro, X. Gu, S. D. Oosterhout, and M. F. Toney, “Ptychography of Organic Thin Films at Soft X-ray Energies,” *Chem. Mater.*, vol. 31, no. 13, pp. 4913–4918, Jul. 2019.
- [126] M. Holler *et al.*, “OMNY - A tOMography Nano crYo stage,” *Rev. Sci. Instrum.*, vol. 89, no. 4, Apr. 2018.
- [127] S. van Bavel, E. Sourty, G. de With, and J. Loos, “3D Nanoscale Organization Of Bulk Heterojunction Polymer Solar Cells,” vol. 27, no. 1, pp. 85–92, 2009.
- [128] A. A. Herzing, L. J. Richter, and I. M. Anderson, “3D nanoscale characterization of thin-film organic photovoltaic device structures via spectroscopic contrast in the TEM,” *J. Phys. Chem. C*, vol. 114, no. 41, pp. 17501–17508, Oct. 2010.
- [129] D. R. Kozub, K. Vakhshouri, L. M. Orme, C. Wang, A. Hexemer, and E. D. Gomez, “Polymer Crystallization of Partially Miscible Polythiophene/Fullerene Mixtures Controls Morphology,” *Macromolecules*, vol. 44, no. 14, pp. 5722–5726, Jul. 2011.
- [130] B. Kuei, B. Kabius, J. L. Gray, and E. D. Gomez, “Strategies for elemental mapping from energy-filtered TEM of polymeric materials,” *MRS Commun.*, vol. 8, no. 03, pp. 1321–1327, Sep. 2018.
- [131] M. Corazza, S. B. Simonsen, H. Gnaegi, K. T. S. Thydén, F. C. Krebs, and S. A. Gevorgyan, “Comparison of ultramicrotomy and focused-ion-



- beam for the preparation of TEM and STEM cross section of organic solar cells," *Appl. Surf. Sci.*, vol. 389, pp. 462–468, Dec. 2016.
- [132] R. C. Masters *et al.*, "Sub-nanometre resolution imaging of polymer–fullerene photovoltaic blends using energy-filtered scanning electron microscopy," *Nat. Commun.*, vol. 6, no. 1, p. 6928, Nov. 2015.
- [133] C. Ophus, "Four-Dimensional Scanning Transmission Electron Microscopy (4D-STEM): From Scanning Nanodiffraction to Ptychography and Beyond," *Microsc. Microanal.*, vol. 25, no. 3, pp. 563–582, Jun. 2019.
- [134] Y. Jiang *et al.*, "Electron ptychography of 2D materials to deep sub-ångström resolution," *Nature*, vol. 559, no. 7714, pp. 343–349, Jul. 2018.
- [135] O. Panova *et al.*, "Diffraction imaging of nanocrystalline structures in organic semiconductor molecular thin films," *Nat. Mater.*, p. 1, Jun. 2019.
- [136] J. Hou, O. Inganäs, R. H. Friend, and F. Gao, "Organic solar cells based on non-fullerene acceptors," *Nat. Mater.*, vol. 17, no. 2, pp. 119–128, 2018.
- [137] D. Baran *et al.*, "Reduced voltage losses yield 10% efficient fullerene free organic solar cells with >1 V open circuit voltages," *Energy Environ. Sci.*, vol. 9, no. 12, pp. 3783–3793, 2016.
- [138] L. F. Drummy, R. J. Davis, D. L. Moore, M. Durstock, R. A. Vaia, and J. W. P. Hsu, "Molecular-Scale and Nanoscale Morphology of P3HT:PCBM Bulk Heterojunctions: Energy-Filtered TEM and Low-Dose HREM †," *Chem. Mater.*, vol. 23, no. 3, pp. 907–912, Feb. 2011.
- [139] B. V. Andersson, A. Herland, and S. Masich, "Imaging of the 3D Nanostructure of a Polymer Solar Cell by Electron Tomography," *Nano Lett.*, vol. 9, no. 2, pp. 853–855, Feb. 2009.
- [140] J. Ramanujam *et al.*, "Flexible CIGS, CdTe and a-Si:H based thin film solar cells: A review," *Progress in Materials Science*, vol. 110. Elsevier Ltd, p. 100619, 01-May-2019.
- [141] K. J. Yang *et al.*, "Flexible Cu<sub>2</sub>ZnSn(S,Se)<sub>4</sub> solar cells with over 10% efficiency and methods of enlarging the cell area," *Nat. Commun.*, vol. 10, no. 1, pp. 1–10, Dec. 2019.
- [142] Z. Yu, M. Leilaoui, and Z. Holman, "Selecting tandem partners for silicon solar cells," *Nat. Energy*, vol. 1, no. 11, p. 16137, Nov. 2016.
- [143] T. Ratz *et al.*, "Physical routes for the synthesis of kesterite," *J. Phys. Energy*, vol. 1, no. 4, p. 042003, Sep. 2019.
- [144] J. J. Scragg, T. Kubart, J. T. Wätjen, T. Ericson, M. K. Linnarsson, and C. Platzer-Björkman, "Effects of back contact instability on Cu<sub>2</sub>ZnSnS<sub>4</sub> devices and processes," *Chem. Mater.*, vol. 25, no. 15, pp. 3162–3171, Aug. 2013.
- [145] S. Siebentritt and S. Schorr, "Kesterites—a challenging material for solar cells," *Prog. Photovoltaics Res. Appl.*, vol. 20, no. 5, pp. 512–519, Aug. 2012.
- [146] K. Ito, *Copper Zinc Tin Sulfide-Based Thin-Film Solar Cells*. Chichester, UK: John Wiley & Sons Ltd, 2014.
- [147] S. Bourdais *et al.*, "Is the Cu/Zn Disorder the Main Culprit for the Voltage Deficit in Kesterite Solar Cells?," *Adv. Energy Mater.*, vol. 6, no. 12, pp. 1–21, Jun. 2016.

- [148] J. J. S. Scragg *et al.*, “Cu-Zn disorder and band gap fluctuations in Cu<sub>2</sub>ZnSn(S,Se)<sub>4</sub>: Theoretical and experimental investigations,” *Phys. Status Solidi Basic Res.*, vol. 253, no. 2, pp. 247–254, 2016.
- [149] J. Kim, S. Park, S. Ryu, J. Oh, and B. Shin, “Improving the open-circuit voltage of Cu<sub>2</sub>ZnSnSe<sub>4</sub> thin film solar cells via interface passivation,” *Prog. Photovoltaics Res. Appl.*, vol. 25, no. 4, pp. 308–317, Apr. 2017.
- [150] C. Yan *et al.*, “Cu<sub>2</sub>ZnSnS<sub>4</sub> solar cells with over 10% power conversion efficiency enabled by heterojunction heat treatment,” *Nat. Energy*, vol. 3, no. 9, pp. 764–772, Sep. 2018.
- [151] X. Cui *et al.*, “Enhanced Heterojunction Interface Quality To Achieve 9.3% Efficient Cd-Free Cu<sub>2</sub>ZnSnS<sub>4</sub> Solar Cells Using Atomic Layer Deposition ZnSnO Buffer Layer,” *Chem. Mater.*, vol. 30, no. 21, pp. 7860–7871, Nov. 2018.
- [152] D. M. Berg *et al.*, “Discrimination and detection limits of secondary phases in Cu<sub>2</sub>ZnSnS<sub>4</sub> using X-ray diffraction and Raman spectroscopy,” *Thin Solid Films*, vol. 569, pp. 113–123, Oct. 2014.
- [153] V. A. Solé, E. Papillon, M. Cotte, P. Walter, and J. Susini, “A multiplatform code for the analysis of energy-dispersive X-ray fluorescence spectra,” *Spectrochim. Acta - Part B At. Spectrosc.*, vol. 62, no. 1, pp. 63–68, 2007.
- [154] R. P. J. Nieuwenhuizen *et al.*, “Measuring image resolution in optical nanoscopy,” *Nat. Methods*, vol. 10, no. 6, pp. 557–562, 2013.
- [155] M. Van Heel and M. Schatz, “Fourier shell correlation threshold criteria,” *J. Struct. Biol.*, vol. 151, no. 3, pp. 250–262, 2005.
- [156] X. Huang *et al.*, “Signal-to-noise and radiation exposure considerations in conventional and diffraction x-ray microscopy,” *Opt. Express*, vol. 17, no. 16, p. 13541, Aug. 2009.
- [157] S. Sasaki, “Numerical Tables of Anomalous Scattering Factors Calculated by the Cromer and Liberman’s Method,” Tsukuba, 1989.
- [158] S. M. Polvino, C. E. Murray, Ö. Kalenci, I. C. Noyan, B. Lai, and Z. Cai, “Synchrotron microbeam x-ray radiation damage in semiconductor layers,” *Appl. Phys. Lett.*, vol. 92, no. 22, p. 224105, Jun. 2008.
- [159] H. Akazawa, “Formation of Silicon Nanocrystals and Interface Islands in Synchrotron-Radiation-Irradiated SiO<sub>2</sub> Films on Si(100),” *Int. J. Mod. Phys. B*, vol. 15, no. 28n30, pp. 3749–3752, Dec. 2001.
- [160] S. Williams *et al.*, “Measurements of wet metaphase chromosomes in the scanning transmission X-ray microscope,” *J. Microsc.*, vol. 170, no. 2, pp. 155–165, May 1993.
- [161] M. Holler *et al.*, “High-resolution non-destructive three-dimensional imaging of integrated circuits,” *Nature*, vol. 543, no. 7645, pp. 402–406, Mar. 2017.